12-2017

Electromechanical Dynamics of High Photovoltaic Power Grids

Shutang You
University of Tennessee, syou3@utk.edu

To the Graduate Council:

I am submitting herewith a dissertation written by Shutang You entitled "Electromechanical Dynamics of High Photovoltaic Power Grids." I have examined the final electronic copy of this dissertation for form and content and recommend that it be accepted in partial fulfillment of the requirements for the degree of Doctor of Philosophy, with a major in Electrical Engineering.

Yilu Liu, Major Professor

We have read this dissertation and recommend its acceptance:

Joshua S. Fu, Fangxing Li, Kai Sun

Accepted for the Council:
Carolyn R. Hodges

Vice Provost and Dean of the Graduate School

(Original signatures are on file with official student records.)

Electromechanical Dynamics of High Photovoltaic Power Grids

A Dissertation Presented for the
Doctor of Philosophy
Degree
The University of Tennessee, Knoxville

Shutang You
December 2017

ACKNOWLEDGEMENTS

First and foremost, I would like to express my sincere thanks to my advisor Professor Yilu Liu. I am deeply grateful for her encouragement and support throughout my PhD study. I cannot be luckier to have her be my advisor. The impact of her great personality and academic excellence on me is one of the few very best gifts I can have throughout my whole life.

Special thanks to Professor Fangxing (Fran) Li, Professor Kai Sun, and Professor Joshua S. Fu, for serving as my dissertation committee. I greatly appreciate their insightful suggestions throughout the research and dissertation preparation. It is impossible to complete this work without their tremendous help.

Thanks to the faculties of the CURENT center and the EECS department at UTK for providing encouraging environments and all great possibilities, especially Professor Fei (Fred) Wang, Professor Kevin Tomsovic, Professor Leon Tolbert, and Dr. Chien-fei Chen.

I would like to thank Dr. Stanton Hadley from Oak Ridge National Laboratory for his guidance on my research. I would also like to thank Dr. Tassos Golnas, Dr. Rebecca Hott, and Dr. Guohui Yuan, from the U.S. Department of Energy Solar Energy Technology Office for their support and advices on this dissertation study.

With a special mention to all colleagues in the Power IT Lab. Working with them has been the unforgettable experience in my life. I am especially thankful for the help from Dr. Yong Liu (Frank), Dr. Lin Zhu, Dr. Zhiyong Yuan (Alan), Dr. Gefei Kou (Derek), Dr. Jiecheng Zhao, Dr. Wenxuan Yao, Dr. Jiahui Guo (Jason), Dr. Hesen Liu, Dr. Micah J. Till, Dr. Dao Zhou, Dr. Jidong Chai (Jack), Dr. Zhuohong Pan, Dr. Yi Cui, Dr. Wenpeng Yu (Wayne), Dr. Yao Zhang, Dr. Jiaojiao Dong, Dr.

Fuhua Li, Dr. Yi Zhao, Dr. He Yin, Ellen Ling Wu, Mike Yu Su, Shirley Xuemeng Zhang, Sundaresh Lakshmi, Weikang Wang, Cujie Zeng, Abigail Till, Melanie Gonzalez, Zhihao Jiang, Summer Fabus, and many other colleagues.

I would like to give my thank to my family, especially my parents Chungeng You and Huaping Fang for their love and support.

ABSTRACT

This dissertation study focuses on the impact of high PV penetration on power grid electromechanical dynamics. Several major aspects of power grid electromechanical dynamics are studied under high PV penetration, including frequency response and control, inter-area oscillations, transient rotor angle stability and electromechanical wave propagation.

To obtain dynamic models that can reasonably represent future power systems, Chapter One studies the co-optimization of generation and transmission with large-scale wind and solar. The stochastic nature of renewables is considered in the formulation of mixed-integer programming model. Chapter Two presents the development procedures of high PV model and investigates the impact of high PV penetration on frequency responses. Chapter Three studies the impact of PV penetration on inter-area oscillations of the U.S. Eastern Interconnection system. Chapter Four presents the impacts of high PV on other electromechanical dynamic issues, including transient rotor angle stability and electromechanical wave propagation. Chapter Five investigates the frequency response enhancement by conventional resources. Chapter Six explores system frequency response improvement through real power control of wind and PV. For improving situation awareness and frequency control, Chapter Seven studies disturbance location determination based on electromechanical wave propagation. In addition, a new method is developed to generate the electromechanical wave propagation speed map, which is useful to detect system inertia distribution change. Chapter Eight provides a review on power grid data architectures for monitoring and controlling power grids. Challenges and essential elements of data architecture are analyzed to identify various requirements for operating high-renewable power grids and a conceptual data architecture is proposed. Conclusions of this dissertation study are given in Chapter Nine.

TABLE OF CONTENTS

LIST OF TABLES

LIST OF FIGURES

CHAPTER ONE
CO-OPTIMIZING GENERATION AND TRANSMISSION EXPANSION WITH RENEWABLES

1.1. Introduction

Bulk power system expansion problems can be divided into three categories: generation expansion [1, 2], transmission expansion [2-4], and generation-transmission co-expansion [5]. Power system operation is subjected to influences from stochastic factors, such as forced outages, load, and fuel cost variations. With the increase of renewable penetration rates, the stochastic features of wind and solar are becoming the major uncertain factors of power systems [6-10]. As studies predict that US could have around 27% of its electricity coming from renewables by 2030 [11], their fluctuations need to be considered not only in the operation stage, but also in the planning stage.

1.1.1. Literature review

Much research focused on expansion planning for generation and transmission. Several methods exist to categorize these studies. For example, studies can be categorized by single-stage [12-14] or multiple-stage formulations of the problem [15-19], which can provide the timing of expansion [20]. Research can also be classified by its solving algorithm: conventional mathematical programming or meta-heuristic optimization methods. While meta-heuristic algorithms possess the capability to deal with non-linear and non-convex optimization problems [21-25], they have the defect of converging to local-optima. Conventional mathematical programming, such as mixed-integer programming, are more computational efficient but their applicability is more restricted by the model characteristics. Some recent research seeks to solve a series of mixed-integer

linear programming problems iteratively to obtain the optimal generation expansion plan [1, 26].

Existing studies can also be classified by their problem formulation structures: some research addresses generation or transmission expansion only; while other studies optimize both the generation and the transmission expansion plan. Research that considers both generation and transmission expansion further falls into two sub-categories. One category is the multi-level or hierarchical models that apply iterative or decomposition methods to obtain the expansion result. For example, Ref. [2, 27, 28] formulated the generation transmission expansion plan as tri-level problems that consist of a pool-based market, generation expansion and transmission expansion. The other category is formulating the two expansion problems in one problem (co-optimization). For example, Ref. [13] proposed a mixed integer nonlinear programming formulation for generation and transmission planning considering the lost load cost, and then the problem was linearized to a mixed integer linear programming problem. In [29-31], the expansion planning is directly formulated as mixed integer programming problems with reliability constraints enforced iteratively. As extensions of the previous work based on the MIP formulation, Ref. [32] applied a modified genetic algorithm to solve the MIP problem and adopted a virtual database to accelerate detailed reliability assessment. Ref. [33] proposed a co-optimizing model with multiple objectives related to renewable energy development.

As renewables grow in power grids, the influence of their uncertainties on generation and transmission planning has drawn much attention. Various methods have been applied to consider wind, solar, and load uncertainties. These methods include the fuzzy decision approach [34], the chance-constrained model [35], and the benders decomposition [12, 36, 37]. Apart from modelling

uncertainty of wind and solar in one spot, [38] further considered the uncertainties of wind speed correlation in integrating wind to a power grid, and the optimal integration plan was obtained using fuzzy techniques. To provide multiple plan candidates, Ref. [39] applied probabilistic power flow to consider the uncertainty of wind power and a genetic algorithm to obtain Pareto optimal solutions of a multi-objective transmission expansion problem.

Recent progresses on robust optimization techniques can consider uncertain parameters in expansion optimization [38, 40, 41]. Two categories of robust optimization models have been successfully applied in power system expansion: probabilistic robust optimization models (e.g. stochastic optimization models) [38, 41] and non-probabilistic robust optimization models [40]. Probabilistic robust optimization models can consider detailed parameter distribution such as wind, solar, and load variation. The most commonly-used techniques for solving a stochastic optimization problem is formulating its deterministic equivalent through scenario construction. Besides considering all possible combinations of uncertainties [42, 43], some techniques to select representative scenarios have been applied, such as Taguchi's Orthogonal Array Testing [44]. As the other category of robust optimization, non-probabilistic robust optimization models are more adaptive to the representation of uncertainties. Therefore, they are applicable when parameter probabilistic distribution is not available. Such uncertainties include policy changes and market participant behaviors. Non-probabilistic optimization models usually adopt the Wald's maximum model to minimize of the maximum adjustment cost and regret [40, 45]. The deficiencies of some robust optimization models include the computation complexity when applied to large-scale systems (for probabilistic robust optimization models) and the lack of ability to quantify the overall expected cost (for non-probabilistic robust optimization models). Besides, scenario construction to balance model

accuracy and complexity is still an active research topic for both categories of methods [46].

1.1.2. Aim and contributions

It has been widely accepted that co-optimization generation and transmission expansion can obtain better results and more investment savings [47]. With this combined planning information, policy makers can formulate market rules, incentives and penalties to make sure regional planning authorities and stakeholders are expanding and operating the power grid in a way close to maximizing social welfare. Moreover, variations of renewables in different regions have significantly increased interface flow and energy exchange between regions, requiring combined generation-transmission expansion optimization.

A major obstacle for implementing existing methods to actual systems is the computation complexity of the Level II problems, which requires multiple year's operation or market simulation. The computation burden further grows exponentially with renewables, fuel price and load uncertainties in the temporal and spatial dimension. Additionally, few studies have investigated co-optimizing generation and transmission expansion considering renewables in large-scale multi-region power grids [48]. This chapter presents a mixed-integer programming (MIP) formulation that can co-optimize generation and transmission expansion considering renewable outputs and load variations on a multi-region basis [49]. For simplicity, wind power is discussed in details in this chapter. Solar generation and combinations of wind and solar can be considered directly using the proposed approach. Contributions of this study include:

- This chapter proposes an uncertainty-incorporated MIP formulation to co-optimize generation and transmission expansion. Under this framework,

the timing and capacity of generation and transmission expansion can be obtained through solving a single optimization problem.

- A scenario generation method is proposed to incorporate the demand and wind/solar diversity across regions in a large-scale power grid. Incorporating these diversities into the co-optimization model facilitates more accurate modelling of inter-regional energy exchange and interface expansion.
- Actual system data of the US Eastern Interconnection (EI) system with a 15-year planning horizon are used to verify the proposed method's capability for implementing in actual large-scale power grids. In addition, the obtained result can aid system planners and policy makers to maximize the social welfare of the EI system.

The structure of this chapter is organized as follows. Section 1.2 presents the formulation of the generation and transmission co-optimization model. Section 1.3 introduces the scenario generation method. Section 1.4 describes the dataset, study cases, and results based on the US EI system. Section 1.5 gives the conclusion.

1.2. Co-optimizing generation-transmission expansion

The generation and transmission expansion model aims to maximize the social welfare or minimize the total cost, which is comprised of the capacity expansion cost, the operation cost, and the emission cost over the planning horizon. The capacity expansion cost includes both the generation and the transmission expansion cost. The operation cost consists of the fixed operation cost and maintenance cost, the varying operation and maintenance cost, the fuel cost of generators, the value of the lost load, and the wheeling cost of transmission

lines. Based on a generic MIP model [50], the objective function of the generation and transmission expansion co-optimization problem can be expressed as:

$$
\begin{aligned}
f = & \sum_{y=1}^{N_Y}\sum_{r=1}^{N_R}\sum_{g=1}^{N_{r,G}} DF_y \cdot \left(C_{Gbuilt,y,r,g} \cdot x_{Gbuilt,y,r,g}\right) \\
& + \sum_{y=1}^{N_Y}\sum_{r=1}^{N_R}\sum_{g=1}^{N_{r,G}} DF_y \cdot \left[C_{FOM,r,g} \cdot P_{\max,r,g}\left(x^0_{r,g} + \sum_{y' \le y} x_{Gbuilt,y',r,g}\right)\right] \\
& + \sum_{y=1}^{N_Y}\sum_{r=1}^{N_R} DF_y \cdot T \sum_{s=1}^{N_{y,S}} pr_{y,s} \cdot \sum_{g=1}^{N_{r,G}} R_{H,r,g} \cdot C_{fuel,y,r,g} \cdot P_{y,r,g,s}\left(x^0_{r,g} + \sum_{y' \le y} x_{Gbuilt,y',r,g}\right) \\
& + \sum_{y=1}^{N_Y}\sum_{r=1}^{N_R} DF_y \cdot T \sum_{s=1}^{N_{y,S}} pr_{y,s} \cdot \sum_{g=1}^{N_{r,G}} C_{VOM,r,g} \cdot P_{y,r,g,s}\left(x^0_{r,g} + \sum_{y' \le y} x_{Gbuilt,y',r,g}\right) \\
& + \sum_{y=1}^{N_Y}\sum_{r=1}^{N_R} DF_y \cdot T \sum_{s=1}^{N_{y,S}} pr_{y,s} \cdot C_{VOLL,r} \cdot P_{USE,y,r,s} \\
& + \sum_{y=1}^{N_Y}\sum_{l=1}^{N_L} DF_y \cdot \left(C_{Xbuilt,y,l} \cdot x_{Xbuilt,y,l}\right) \\
& + \sum_{y=1}^{N_Y}\sum_{l=1}^{N_L} DF_y \cdot T \sum_{s=1}^{N_{y,S}} pr_{y,s} \cdot C_{Wheeling,l} \cdot I_{y,l,s} \cdot \left(x^0_{r,l} + \sum_{y' \le y} x_{Xbuilt,y',l}\right) \\
& + \sum_{y=1}^{N_Y}\sum_{r=1}^{N_R}\sum_{g=1}^{N_{r,G}} DF_y \cdot \left[C_{emm,y,r,g} \cdot e_{r,g} \cdot T \sum_{s=1}^{N_{y,S}} pr_{y,s} \cdot P_{y,r,g,s}\left(x^0_{r,g} + \sum_{y' \le y} x_{Gbuilt,y',r,g}\right)\right]
\end{aligned}
\tag{1.1}
$$

where DF_y is the discount factor in year *y*. Before the end of the planning horizon, its value is:

$$
DF_y = \frac{1}{(1+d)^y} \qquad y = 1,2,\ldots,\ N_Y - 1 \tag{1.2}
$$

It is important that the expansion planning formulation does not inappropriately consider the end of the planning horizon to be the ‘end of time’. Without considering the ‘end-year effects’, the expansion plan would select to build generators with low build costs in the last several years, even if their marginal generation costs are high, so that the average cost in the horizon would be low. To reflect the ‘end-year effects’, the last year of the horizon is repeated an infinite number of times [50]. Therefore, the discount factor in the end year considering the ‘end-year effects’ is

$$DF_{N_Y} = \frac{1}{(1+d)^{N_Y}} + \frac{1}{(1+d)^{N_Y+1}} \cdot \frac{1}{\left(1 - \frac{1}{1+d}\right)} \tag{1.3}$$

In (1.1), $\sum_{y=1}^{N_Y} \sum_{r=1}^{N_R} \sum_{g=1}^{N_{r,G}} DF_y \cdot \left(C_{Gbuilt,r,g} \cdot x_{Gbuilt,y,r,g}\right)$ is the generation built cost in all regions;

$\sum_{y=1}^{N_Y} \sum_{r=1}^{N_R} \sum_{g=1}^{N_{r,G}} DF_y \cdot \left[C_{FOM,r,g} \cdot P_{\max,r,g} \left(x_{r,g}^0 + \sum_{y' \le y} x_{Gbuilt,y',r,g} \right) \right]$ is the fixed operation and maintenance cost in all regions (in $/kW/year, forming part of the unit annual fixed cost charge); $\sum_{y=1}^{N_Y} \sum_{r=1}^{N_R} DF_y \cdot T \sum_{s=1}^{N_{y,S}} pr_{y,s} \cdot \sum_{g=1}^{N_{r,G}} R_{H,r,g} \cdot C_{fuel,y,r,g} \cdot P_{y,r,g,s} \left(x_{r,g}^0 + \sum_{y' \le y} x_{Gbuilt,y',r,g} \right)$ denotes the fuel cost. $\sum_{y=1}^{N_Y} \sum_{r=1}^{N_R} DF_y \cdot T \sum_{s=1}^{N_{y,S}} pr_{y,s} \cdot \sum_{g=1}^{N_{r,G}} C_{VOM,r,g} \cdot P_{y,r,g,s} \left(x_{r,g}^0 + \sum_{y' \le y} x_{Gbuilt,y',r,g} \right)$ denotes the varying operation and maintenance cost (in $/kW/year, representing an incremental cost of generation used to recover regular equipment replacement and servicing costs that are a direct function of generation, e.g. wear and tear); $\sum_{y=1}^{N_Y} \sum_{r=1}^{N_R} DF_y \cdot T \sum_{s=1}^{N_{y,S}} pr_{y,s} \cdot C_{VOLL,r} \cdot P_{USE,y,r,s}$ denotes the value of lost load;

$\sum_{y=1}^{N_Y} \sum_{l=1}^{N_L} DF_y \cdot \left(C_{Xbuilt,y,l} \cdot x_{Xbuilt,y,l}\right)$ is the transmission expansion cost of all interfaces;

$\sum_{y=1}^{N_Y} \sum_{l=1}^{N_L} DF_y \cdot T \sum_{s=1}^{N_{y,S}} pr_{y,s} \cdot C_{Wheeling,l} \cdot I_{y,l,s} \cdot \left(x_{r,l}^0 + \sum_{y' \le y} x_{Xbuilt,y',l} \right)$ is the wheeling cost of transmission lines; $\sum_{y=1}^{N_Y} \sum_{r=1}^{N_R} \sum_{g=1}^{N_{r,G}} DF_y \cdot \left[C_{emm,y,r,g} \cdot e_{r,g} \cdot T \sum_{s=1}^{N_{y,S}} pr_{y,s} \cdot P_{y,r,g,s} \left(x_{r,g}^0 + \sum_{y' \le y} x_{Gbuilt,y',r,g} \right) \right]$ is the emission cost.

The objective function (1.1) is the net present value of the sum of all of the system's cost items over the planning horizon considering the 'end-year effects'. A practical expansion plan should also satisfy various planning and operation constraints. Constraints considered in this expansion planning problem include:

- Power balance constraint

In each region, the sum of generation output, unserved demand, and interface interchange should equal to the demand for all regions within the planning horizon.

$$\sum_{g=1}^{N_{r,G}} P_{y,r,g,s} + P_{USE,y,r,s} + \sum_{l \in \Omega_r} I_{y,l,s} = L_{y,r,s} \qquad \forall y, \forall r \qquad (1.4)$$

where $\sum_{g=1}^{N_{r,G}} P_{y,r,g,s}$ denotes generation of all generators in region *r* under the scenario *s*; $\sum_{l \in \Omega_r} I_{y,l,s}$ denotes the power interchange through all the interfaces of region *r*.

- Maximum expansion constraint for generation

Due to resource limitation (such as maximum exploitable resources for hydro and nuclear power plants), the number of generator expansion in each region should be within its upper limit.

$$\sum_{y \le N_Y} x_{Gbuilt,y,r,g} \le X_{MaxGbuilt,r,g} \qquad \forall g, \forall r \qquad (1.5)$$

- Maximum expansion constraint for transmission

Due to the right-of-way limitation, the number of expanded interfaces should be within its upper limit.

$$\sum_{y \le N_Y} x_{Xbuilt,y,l} \le X_{MaxXbuilt,l} \qquad \forall l \qquad (1.6)$$

- Integer constraint

The number of built generators and interfaces should be integers.

$$x_{Gbuilt,y,r,g} \in N \; ; \; x_{Xbuilt,y,l} \in N \qquad (1.7)$$

- Expansion speed constraint

Due to the construction resource limitation, the annual expansion speed of generators and transmission lines should be within their upper limits.

$$x_{Gbuilt,y,r,g} \le \bar{x}_{Gbuilt,y,r,g}; \; x_{Xbuilt,y,l} \le \bar{x}_{Xbuilt,y,l} \qquad \forall y, \forall g, \forall r, \forall l \qquad (1.8)$$

- Capacity discount considering the forced and maintenance outages

In each region, the available capacity is usually less than the installed capacity due to forced and maintenance outages. The capacity discount is determined by the maintenance outage rate, the maintenance factor, and the forced outage rate. Since maintenance tasks are usually scheduled in off-peak periods, the maintenance factor $MF_{r,s}$ is related to the load level in scenario *s*.

$$\overline{P}_{\max,\,r,g,s} \le \left(1 - F_{MOR,r,g} \cdot MF_{r,s} + F_{FOR,r,g}\right) \cdot P_{\max,\,r,g} \cdot \left(x^0_{r,g} + \sum_{y' \le y} x_{Gbuilt,y',r,g} \right) \qquad \forall g, \forall r \qquad (1.9)$$

- Regional reserve capacity constraint

The reserve capacity of each region should be larger than a pre-determined level for regulation and contingency requirements. The reserve capacity level is set to be able to cover the energy imbalance caused by any single generator or interface failure associated with this region.

$$\overline{P}_{\max,\,r,g,s} \left(x^0_{r,g} + \sum_{y' \le y} x_{Gbuilt,y',r,g} \right) \ge L_{y,r,s} - p \sum_{l \in \Omega_r} I_{y,l,s} + Rs_{y,r} \qquad \forall y, \forall r \qquad (1.10)$$

- Interface capacity constraint

To facilitate interregional analysis based on information provided by regional planning authorities [51], resources inside a region are considered to be connected to a notional node. Nodes that are not associated with a region is considered as regions by themselves. The interface power flows between regions are modeled by the transportation model [52, 53]. Interface flows should satisfy their limits.

$$-P_{l,\max} \left(x^0_{r,l} + \sum_{y' \le y} x_{Xbuilt,y',l} \right) \le I_{y,l,s} \le P_{l,\max} \left(x^0_{r,l} + \sum_{y' \le y} x_{Xbuilt,y',l} \right) \qquad \forall y, \forall l \qquad (1.11)$$

- Regional renewable portfolio constraint

In those regions with renewable portfolio constraints, the percentage of renewables in the total installed generation capacity should be higher than a pre-determined value.

$$\sum_{g=1}^{N_{r,G}} P_{\max\,r,g} \left(x^0_{r,g\,(renew)} + \sum_{i \le t} x_{Gbuilt,y,r,g\,(renew)} \right) \ge RPS_{y,r} \cdot \sum_{g=1}^{N_{r,G}} P_{\max\,r,g} \left(x^0_{r,g} + \sum_{y' \le y} x_{Gbuilt,y',r,g} \right) \quad \forall y, \forall r \qquad (1.12)$$

- Renewable resource constraint

The output of renewable generation is restricted by the available resource, such as wind speed and solar irradiance. Here, wind resource constraint is formulated as an example.

$$P_{y,r,g,s\,(wind)} \le CF_{y,r,s}\overline{P}_{\max,r,g\,(wind)} \qquad \forall y, \forall r, \forall g \qquad (1.13)$$

Objective function (1.1) and constraints (1.4) - (1.13) comprise a mixed-integer programming problem that minimizes the cost of the expansion plan while satisfying multiple operational and environmental constraints.

Except for the fixed operation and maintenance cost, all the operation-related cost items in the objective function are related to the load and wind levels. The obtained expansion plan is the optimal considering all the stochastic factors, such as load and wind. Section 1.3 will show the methodology of integrating these stochastic factors into the generation and transmission expansion co-optimization problem.

1.3. Scenario creation for multi-region systems

In long-term planning, hourly load data are usually aggregated and represented by blocks (load scenarios) for computation complexity consideration. Typical load aggregation methods include the load duration curve method and the load curve fitting method. The resulting load representation will have a limited number of scenarios in each year that represent different levels of demand and corresponding time duration.

For multi-region expansion planning, load scenarios should be synchronized (the load data in one scenario have the same chronological time stamps for all

regions) to preserve the load diversity across regions. Load scenario synchronization is accomplished through the steps shown in Table 1.1.

Table 1.1. Load scenario synchronization for multi-region power grids

Step	Description
1)	Obtain the load duration curves $\{L'\}_{N_Q}$ of the system based on the future demand data obtained by load forecasting. The total number of the curves is N_Q and each curve has probability pr'_q.
2)	The target scenario load scenarios $\{L_{y,s}\}_{N_{y,s}}$ and probabilities $pr_{y,s}$ are simultaneously optimized using the least square fitting approach, i.e. minimizing $\sum_{s=1}^{N_{y,s}} pr_{y,s}\left(\sum_{q=1}^{N_Q} pr'_q\left(L_{y,s}-L'\right)^2\right)$. (In particular, the maximum demand periods of all load duration curves are preserved to form a scenario.) Recording the chronology-to-scenario mapping function Θ_L.
3)	Use Θ_L to re-arrange the load data of each region.
4)	Calculate the expected value of load data for each scenario and region. The scenario probabilities are inherited from Step 2).

Similar to load, the wind power variation in each region should also be considered in expansion planning, especially if wind generation is a significant fraction of the total generation. In addition, since large power systems usually have wide geographic areas, wind resources could vary greatly in different regions at the same time point. Therefore, it is needed to develop a sub-scenario creation method that can most effectively capture the information of multi-regional chronological wind output. The expansion model can then include multiple scenarios of wind power output in each region, as well as the correlation information of wind power output across regions in each demand level.

To meet this requirement, a generic scenario creation method for multiple stochastic variables in expansion planning is shown in Figure 1.1. Description of some steps is as follows.

- Step 1. Prepare the time series load, wind, or solar data over the planning horizon based on forecast data or scaling historical records.
- Step 2. Use the least square fitting method to form N_{S_L} load scenarios, namely $s_{L1}, s_{L2}, \ldots, s_{LN_{SL}}$, in each year. That is $N_{S_L} \times N_Y$ scenarios in total over the planning horizon. Probability of each scenario is denoted by $pr_{y,s}$.
- Step 3. Select the next stochastic factor v_k (v_k could be wind, solar, or cost uncertainty depending on the influences on expansion. In the following steps, wind is described for convenience).
- Step 4. Create the system-scale time series of the wind capacity factor. In many large-scale power grids, wind farms (both existing and candidate) are centralized in certain regions with rich wind resource, the time-series wind capacity factors in these regions are better indicators of the wind output of the whole system compared with those of the regions that have much less wind power. Thus, the weighted time series value of the wind capacity factors is used to form a system-scale chronological attribute— the multi-region system wind capacity factor $CF_{system,t}$.

$$CF_{system,t} = \sum_{r=1}^{N_R} WindCap_r^* \cdot CF_{r,t} \tag{1.14}$$

where $WindCap_r^*$ denotes the rough target wind generation capacity in the region r, which can be obtained through estimation or iteratively updating from the previous planning result. $CF_{r,t}$ is the time-series wind capacity factor in region r. N_R is the number of regions.

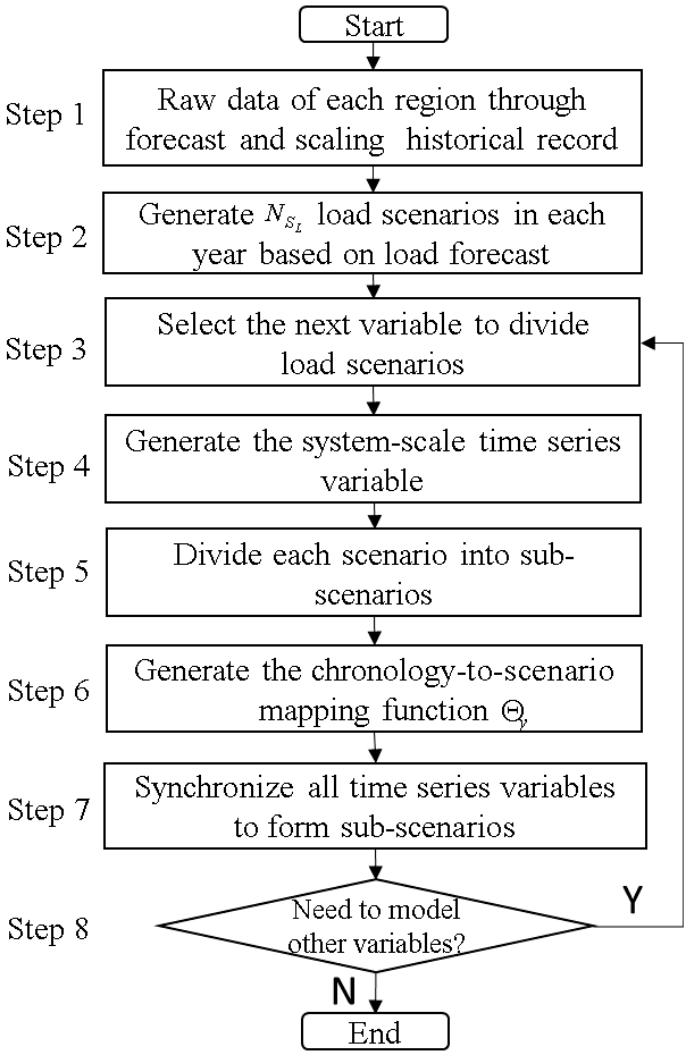

Figure 1.1. The sub-scenario creation procedure

- *Step 5.* Divide each load scenario s_{Ll} into N_{S_W} sub-scenarios of different wind scenarios, namely $s_{Ll,W1}, s_{Ll,W2}, \ldots, s_{Ll,WN_{SW}}$. Each sub-scenario represents a certain range of those wind capacity factors happening during the corresponding period of the load scenario. For instance, the lowest $1/N_{S_W}$ percent system-scale wind capacity factor chronological data ($CF_{system,t}$) in the load scenario s_{Ll} is aggregated in sub-scenario $s_{Ll,W1}$, and the highest $1/N_{S_W}$ percent data is aggregated in $s_{Ll,WN_{SW}}$. The probability of each sub-scenario is $pr_{y,s}/N_{S_W}$. (An alternative and more computation-intensive method to obtain the sub-scenarios and probabilities using the least square approach as described before.)
- Step 6. Generate the chronology-to-scenario mapping function Θ_y. In forming each sub-scenario, the correspondence between the original chronological data $CF_{system,t}$ and each sub-scenario $s_{Ll,Ww}$ is recorded as the chronology-to-scenario mapping function denoted by Θ. Note that Θ differs from year to year and it is denoted by Θ_y for year y.
- Step 7. According to the chronology-to-scenario mapping function Θ_y, synchronize all the chronological data (load, wind, and solar) of all regions to form $\left(N_{S_L} \times N_{S_W}\right) \times N_Y = N_S \times N_Y$ scenarios.
- Step 8. Check if there are other stochastic factors (such as solar in high solar systems) that need to form sub-scenarios in expansion planning. If so, return to Step 3. Otherwise, we end the scenario generation process.

This scenario forming method can model multiple coupled stochastic variables (e.g. solar generation) for long-term expansion planning through creating scenarios that have various probabilities in a computationally effective way.

Moreover, the formed scenarios can be directly put into the mixed-integer programming model, and then solved through commercial mathematical programming solvers to obtain the optimal generation-transmission co-expansion plan. It should be noted that Step 7 synchronizes all the stochastic factors, so those factors that have not been selected to further divide scenarios still have different values in different scenarios. The difference is that their scenarios are passively formed (or synchronized) since their information is not specifically used to form sub-scenarios due to that the computation complexity restricts the number of scenarios in the optimization problem.

1.4. Implementation on the US EI system

1.4.1 Dataset and case description

The proposed model and the scenario generation method is applied to the United States Eastern Interconnection (EI) multi-regional dataset created by the EIPC and Charles River Associates [51] and translated to PLEXOS format by Energy Exemplar [50]. This dataset partitions the EI system into 25 regions and the interfaces between adjacent regions as shown in Figure 1.2 [54]. The planning horizon is from 2015 to 2030. Wind and solar resource data are from historical record and the impacts of yearly climate change on solar irradiance and wind speed are not considered in this study. Five developed cases with different scenario formation methods and number of scenarios are shown in Table 1.2. The EI multi-regional dataset and the generation and transmission expansion problem are modeled in PLEXOS [50] and the problem is solved by the MIP solver —Xpress-MIP 26.01.04. The optimization is performed on a server with two Intel Xeon E5-2470.0 V2 CPUs (2.40 GHz, 40 cores) and 128 GB memory.

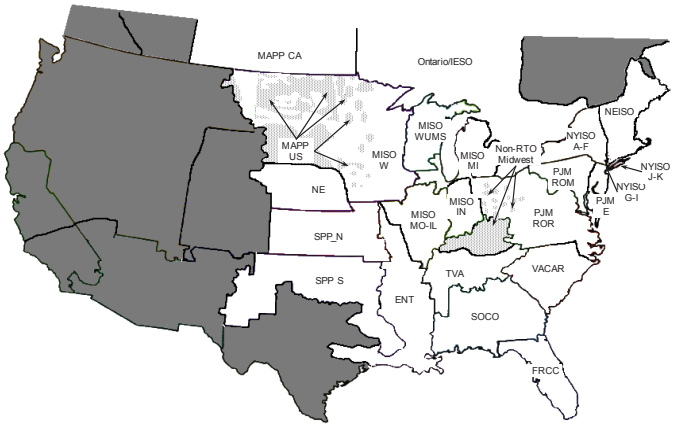

Figure 1.2. Regions of the U.S. EI system (EI includes all east regions) [55]

Table 1.2. Description on the developed cases

Case Name	Number of sub-scenarios	Case Description
20 Scenarios (20-Scn)	$N_{S_W} = 1$	• The base case has 20 load scenarios in each year • Wind is the average value in each load scenario
40 Scenarios Non-Synchronized (40-Scn-NonSync)	$N_{S_W} = 2$	• Splitting each scenario in two equal number of hours • Average of high wind in a half and average of low wind in the other half (*wind data are not synchronized*).
40 Scenarios Synchronized (40-Scn-Sync)	$N_{S_W} = 2$	• Determining hours of high and low wind capacity factors based on the weighted average system-scale data in each of the 20 load scenarios • Synchronizing wind, solar, and load to the average of the region's values in those hours
80 Scenarios Synchronized (80-Scn-Sync)	$N_{S_W} = 4$	• Breaking each load scenario into four quartiles based on the weighted average system-scale data in each of the 20 load scenarios • Synchronizing all regions' wind, solar, load, and fuel prices to those hours
160 Scenarios Synchronized (160-Scn-Sync)	$N_{S_W} = 8$	• Breaking each load scenario into eight quartiles based on the weighted average system-scale data in each of the 20 load scenarios • Synchronizing all regions' wind, solar, load, and fuel prices to those hours

1.4.2. Comparison and analysis on the expansion results

Applying the co-optimization model, the expansion results of the five cases are summarized in Table 1.3. It can be noted that the planning results of Case 40-Scn-Sync is between that of Case 20-Scn and Case 40-Scn-NonSync. Since Case 20-Scn only includes one wind output scenario (i.e. the average wind output) in each load scenario, it overestimates the capacity of wind power and underbuilds transmission capacity. Compared with 40-Scn-Sync, the 40-Scn-NonSync Case underestimates the capacity value of wind power since it assumes all regions' wind power is at the high or low half simultaneously, which also leads to more transmission expansion. The 80-Scn-Sync and 160-Scn-Sync Cases add less wind than 40-Scn-Sync but more transmission. This is because the two cases modeled higher wind peak generation scenarios, which need more transmission capacity to export. In the meantime, modelling lower wind scenarios reduces wind power's capacity value, thereby reducing wind power expansion in the planning result.

The transmission expansion over the planning horizon of the five cases is shown in Figure 1.3. The number of expanded interfaces of Case 20-Scn is smaller than that of Case 160-Scn-Sync. It indicates that using more detailed wind scenarios will make the transmission expansion more dispersed in space. Particularly, compared with 20-Scn, both 40-Scn-Sync, 80-Scn-Sync, and 160-Scn-Sync have smaller transmission expansion on the interface MISO_IN to PJM_ROR.

Table 1.3. The expansion result summary of the five cases

Expansion results	20-Scn	40-Scn-NonSync	40-Scn-Sync	80-Scn-Sync	160-Scn-Sync
Wind Candidates Built Capacity[a] (GW)	262	218	223	221	218
All Gen Built Capacity (GW)	407	373	381	380	378
Wind Capacity in 2030 (GW)	304	260	265	263	260
Wind Generation in 2030 (TWh)	917	768	783	776	766
All Gen Build Cost (NPV) (billion $)	649	595	603	601	598
Trans Build Cost (NPV) (billion $)	20.2	26.1	22.1	22.5	25.0
Emission in 2030 (million ton)	305	365	358	362	368
Fuel Offtake 2030 (million GBTU)	17.1	18.2	18.1	18.1	18.2

[a] Excluding wind power that has already been decided to build.

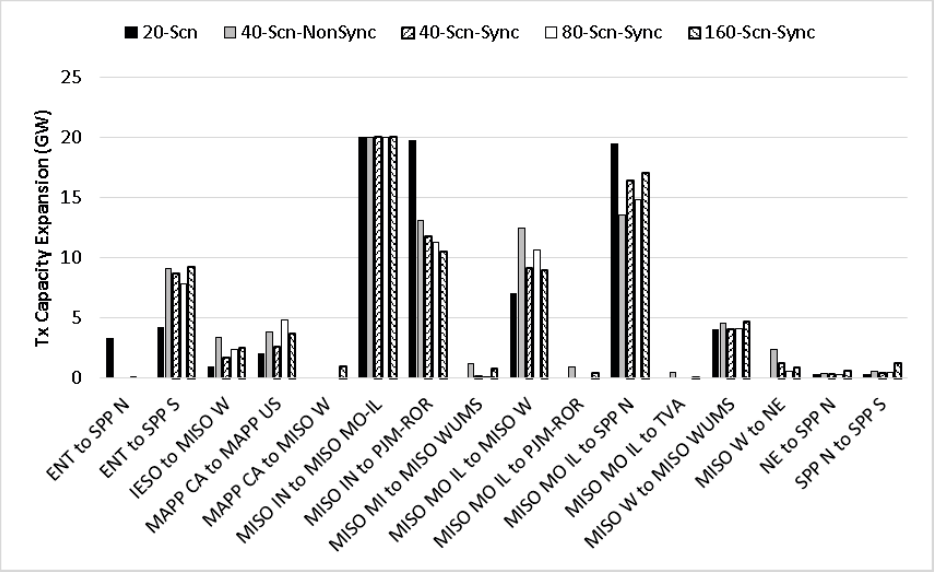

Figure 1.3. Transmission expansion over the planning horizon in the five cases (Refer to Figure 1.2 for the labels)

Table 1.4 shows the expansion of natural gas and wind generation capacity in PJM_ROR and SPP_N. Figure 1.4 shows the energy flow in 2030 for the Case 20-Scn and Case160-Scn-Sync. Combining Table 1.4 and Figure 1.4, it can be seen that in the 20-Scn Case, a large proportion of import energy to PJM_ROR comes from wind in SPP_N. When detailed wind scenarios are incorporated (such as in Case 160-Scn-Sync), PJM_ROR relies more on its local natural gas plants.

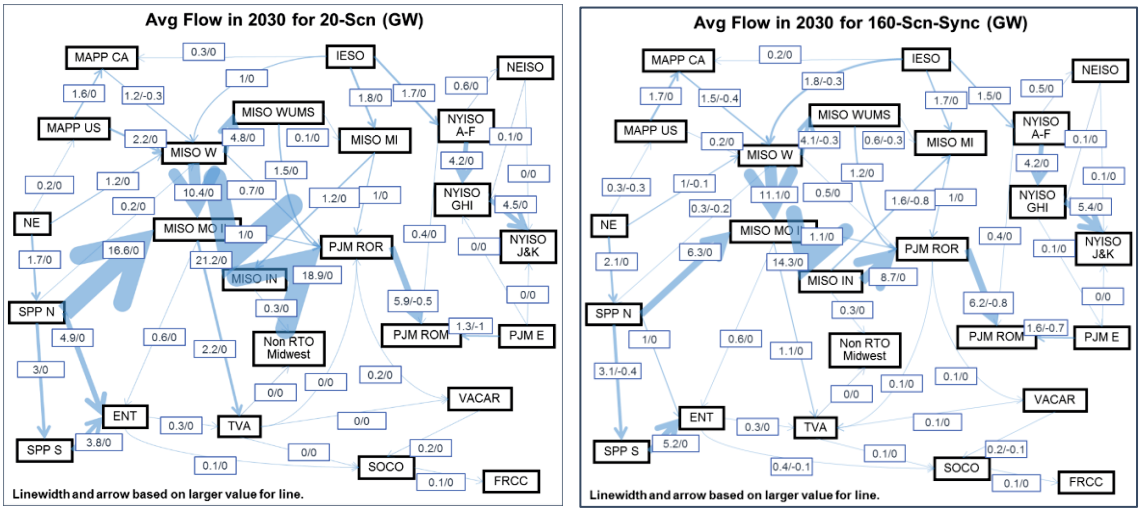

(a) Case 20-Scn (b) Case 160-Scn-Sync

Figure 1.4. Annual energy flow of Case 20-Scn and 160-Scn-Sync (Linewidth is proportional to interface annual energy flow)

In addition, it can be noted from Figure 1.4 that the annual energy flow of almost all interfaces in 160-Scn-Sync increase except for those on the major wind power delivery corridor: SPP_N – MISO_MO_IL – MISO_IN – PJM_ROR. This indicates that detailed wind scenarios will increase the energy exchange frequency and amount between adjacent regions, while decreasing the economy of enforcing

transmission networks to transmit a large amount of wind power through a long distance.

Table 1.4. Expansion of gas and wind generation in Region PJM_ROR and SPP_N

Expansion Results	**20-Scn**	**40-Scn_NonSync**	**40-Scn-Sync**	**80-Scn-Sync**	**160-Scn-Sync**
PJM_ROR Gas Combined Cycle Built (GW)	6	12	15.5	16	17.5
SPP_N Wind Built[a] (GW)	76.8	37.4	41.0	37.4	37.4
PJM_ROR Net Interchange	153 TWh Import	82 TWh Import	78 TWh Import	69 TWh Import	61 TWh Import

[a] Excluding wind power that has already been decided to build.

For comparison, Figure 1.5 shows the annual energy flow of the not-co-optimized case (which optimizes transmission and generation expansion sequentially [56]). The not-co-optimized solution chooses to expand the interface between MISO_W and PJM_ROR. In fact, expansion of this interface requires high investment, making the whole expansion plan uneconomic. On the contrary, the co-optimized case can leverage multiple regions with good wind resources (e.g. MISO_W and SPP_N) and transfer this energy through an optimal path to regions with high load and low wind (e.g. PJM).

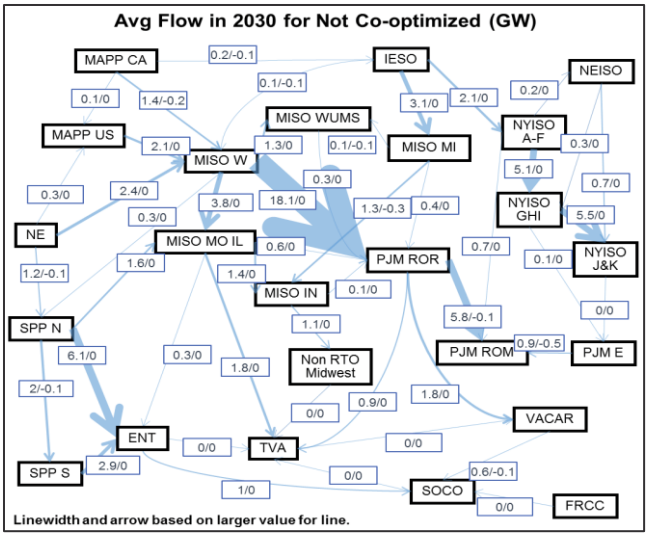

Figure 1.5. Annual energy flow of the not-co-optimized case (Linewidth is proportional to interface annual energy flow)

1.4.3. Long-term (LT) and short-term (ST) simulation results comparison

To quantify the accuracy improvement through the proposed scenario generation method, the long-term expansion result is compared with the short-term simulation result for each case. The long-term simulation applies economic dispatch based on the scenarios generated in the expansion planning model, while short-term simulation uses unit commitment and economic dispatch based on the chronological hourly data. The LT-and ST comparison result is shown in Table 1.5. It can be noted that there are always gaps between the short-term and long-term results. This is because long-term expansion uses the aggregated scenarios that omit some information in the hourly data. It can be noted that for most cases, generation cost errors of synchronized cases are smaller compared with those of the non-synchronized case, and a larger number of scenarios will further reduce the generation cost error. For the emission cost, the LT-ST gap is the smallest for the Case 40-Scn-NonSync. The reason is that Case 40-Scn-NonSync assumes that the high wind scenarios come simultaneously for all

regions, which tends to overestimate the emission cost because it does not appropriately consider the inter-generational balance of renewable output. Meanwhile, Case 40-Scn-NonSync tends to underestimate the emission cost because it does not adequately model wind variation: only distinguishing the higher 50% and lower 50% wind production in each region. Combining the two factors may cancel out the errors and result in a smaller LT-ST gap on emission costs compared with synchronized cases. Nevertheless, it is noted that the emission cost error is much smaller than the significant improvement in generation cost modeling, which is the major contributor of the expansion result improvement.

Table 1.5. LT and ST simulation results in 2030

Results	**LT/ST**	**20-Scn**	**40-Scn-NonSync**	**40-Scn-Sync**	**80-Scn-Sync**	**160-Scn-Sync**
Generation cost (NPV billion $)	LT	47.9	55.0	54.4	54.9	55.2
	ST	60.3	61.9	60.0	59.7	59.5
	LT-ST Gap	20.6%	11.1%	9.3%	8.0%	7.2%
Emission cost (NPV billion $)	LT	42.8	51.0	50.0	50.5	51.3
	ST	50.9	52.6	52.5	53.1	53.2
	LT-ST Gap	15.9%	3.0%	4.7%	4.9%	3.6%
Computation time		1h 6min	1h 14min	1h 28min	4h 28min	12h 30min

It shows that Case 160-Scn-Sync has the smallest difference between long-term and short-term simulations, indicating that the operation simulation in Case 160-Scn-Sync is closest to short-term realistic operation. Therefore, based on more

accurate modelling of the system operation, the expansion co-optimization result obtained in Case 160-Scn-Sync is more reasonable (but at the expense of execution time.)

1.5. Conclusion

In this chapter, generation and transmission expansion is co-optimized using the proposed MIP model, which can be solved robustly using MIP solvers to obtain the global optimal solution. A scenario creation method is proposed to represent wind/solar and load diversities of different regions effectively, thus modelling the interchange of energy between regions more accurately. This scenario creation method can efficiently incorporate uncertainties and operation details into the MIP model for obtaining better expansion plan. The co-optimization model and the scenario creation method are verified through comparing the long-term and short-term simulation results of the US EI system. Additional findings in implementing the proposed framework to the case study are:

(1) Compared with separated optimization, the co-optimized model is able to better leverage renewable resources and find a cost-effective path to transmit energy to regions with high load and low renewables. The MIP formulation features a systematic consideration of generation and transmission expansion resources.

(2) Incorporating the diversity of renewable resources through using more scenarios will decrease the renewable expansion capacity and make transmission expansion more dispersed in space. In addition, detailed renewable scenarios will reveal that it may be less economic to expand transmission networks to transmit a large amount of renewable energy through a long distance in the EI system.

CHAPTER TWO
HIGH PV POWER GRID MODEL DEVELOPMENT AND IMPACT OF PV ON FREQUENCY RESPONSE

2.1. Introduction

Power system frequency response refers to the frequency transient profile after a disturbance. In a few seconds following the disturbance, the rate of change of frequency will be primarily determined by system inertia for a given imbalance amount. Larger system inertia will result to smaller ROCOF, and vice versa [57]. In contrast, governors determine prime movers' response to the frequency deviation and thus influence the settling frequency. As frequency response is critical to system stability and security, underperformance of system frequency response will trip off or damage system components, causing load shedding, or even losing stability [58, 59].

As discussed in Chapter One, PV and wind power plants are expected to have substantial growth worldwide [60, 61]. These renewable power plants have very low or even zero inertia and therefore unable to provide the frequency support as synchronous generators. In addition, most PV plants are operating at the maximum power tracking mode, which doesn't reserve any real power for frequency regulation. Therefore, the primary frequency response will be inadequate and special attention is need to strengthen the primary frequency control reserve to ensure acceptable frequency regulation capabilities. Additionally, the location of the primary frequency may need to be relocated to prevent transmission bottlenecks. Also, the slow ramping of the renewable resources will increase the demand on secondary frequency control capability [62]. These factors contribute to the poor frequency regulation capability of the system after disturbances under high PV penetration.

Researchers have started to investigate the impact of increasing PV on power system transient stability including frequency response. Ref. [63] studied the steady state and angle stability of a system during a bus fault disturbance under different PV penetration rates. Ref. [64] presented a comparative study on the angle stability under the penetration of three different types of PV, namely, distributed PV, utility-scale PV with and without voltage control. Ref. [65] reviewed the system frequency response after a generator loss with the increasing wind and PV. This review attested that existing primary control support schemes may not provide adequate frequency support for some networks under increased wind/PV generation. Ref. [66] studied the South Australia system's frequency response under high PV and wind. It confirmed that low inertia can become a serious issue under high renewable penetration. Ireland's operation experience with 50% wind power also verified the significant challenge to deal with severely reduced system inertia [65]. Clearly, to achieve high renewable penetration, frequency deviations due to the loss of system inertial and primary response must be accurately quantified and effectively mitigated.

The United States has enormous potential to obtain its energy from the sun [67]. As the capacity of solar photovoltaic (PV) grows, one major challenges to grid stability will be the decreasing system inertia and deteriorating frequency response [68]. Preliminary studies on both EI and WECC systems already demonstrated that the overall frequency response of both systems will deteriorate significantly with increasing renewable generation [61]. This study investigated the U.S. EI system frequency response with high PV penetration. The sitting of PV power plants is based on economic analysis on the Eastern Interconnection system, and the maximum penetration of PV and wind reaches 80%. To the best of our knowledge, this study is the first effort to investigate the

frequency response of an actual large-scale system under such a high renewable penetration rate. This chapter studied the changes of system frequency response characteristics, such as frequency nadir, ROCOF, and settling frequency, with the increasing penetration of PV. Changes in the regional frequency drop under high PV penetration were also investigated. In addition, this chapter analyzed the impact of different voltage/Var control modes of PV plants on system frequency response. The quantitative analysis helps system operators and planners to understand the system frequency response capability under high PV penetration and lay out proper mitigating actions [69].

The reminder of this chapter is organized as follows. Section 2.2 introduces the model, PV distribution projection, and high model development in the EI system. Section 2.3 analyzes the impact PV penetration on frequency response at both the system level and regional level, as well as the impact of voltage/var control mode. Section 2.4 concludes the chapter.

2.2 High PV power grid model development

2.2.1. Base model overview

With a peak power of ~610 GW in 2015, the EI system is the biggest power grid in the North America and the second largest power grid in the world. With a rich solar territory that covers two thirds of the United States mainland, EI has great potential to reach high PV penetration.

In this study, the detailed EI multiregional modeling working group (MMWG) 2030 model with ~70k buses will be used for study. This model is developed and used by the EI regional reliability councils and their member utilities to evaluate operating conditions and plan future infrastructures for the EI system [70]. This power flow model depicts a scenario in which wind generation provides 15%

instantaneous power and some transmission network upgrades are built to facilitate wind power transfer, primarily from west to east within the EI. Earlier efforts also include the development of corresponding dynamic models, including synchronous generators, excitation systems, and turbine governors. Some statistic values on this model are shown in Table 2.1. More detailed information on this dynamic modeling effort can be found in [71]. Compared with reduced or generic models, the detailed model can significantly enhance the completeness of this study.

Table 2.1. Basic Information of the EI Model

EI model Statistics	**Value**
Total Bus Number	68309
Generator Number	8337
Branch Number	58784
Operating Generation Capacity	600 GW
Load	540 GW

2.2.2. Base model validation using synchrophasor frequency measurement

Wide area measurement systems (WAMS) have been deployed to provide accurate measurements of EI frequency performances [72, 73]. Using measurements from WAMS, it has been noticed that the EI primary frequency response (defined as the sum of the change in demand, plus the change in generation, divided by the change in frequency, expressed in MW per 0.1 Hz) had been decreasing by 32% over 15 years before 2009 (1994-2009), and then it slowly increases since 2012 [74]. This is mainly due to stricter primary frequency requirements and better implementation of governor settings in the industry [75, 76]. It is also found that the original EI model tend to exhibit frequency responses that are more optimistic than actual performances measured by WAMS [77].

Therefore, before studying frequency response under high renewable penetration conditions, the EI model was validated using WAMS frequency measurement to further enhance the model credibility.

In the model validation process, the governor dead-band model was inserted to the original models in our previous work [78, 79] and the governor droop and generator inertia parameters were adjusted coordinately to more realistic values in order to make the simulated and measured frequency responses following the same disturbance match each other in terms of ROCOF, nadir, settling time, and settling frequency. Multiple disturbances have been used to verify the accuracy of the model validation results [78, 79]. Since model validation is not the focus of this chapter, only one example is given in this subsection for each system, as shown in Figure 2.1.

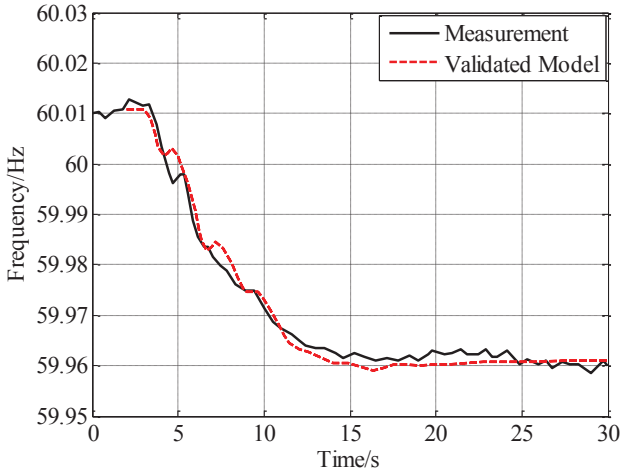

Figure 2.1. Frequency response model validation in EI

As shown in Figure 2.1, the simulated frequency response of EI shows a good match with actual measurements, laying firm foundations for studying frequency responses under high renewable penetration. In addition, to facilitate the study of

oscillation damping control function of renewable power plants, inter-area oscillations of the models were compared with the measurement during model validation. The comparison shows the model can represent the major features of the inter-area oscillation.

2.2.3. Scenario development

To finalize the total PV penetration of the to-be-developed high PV simulation scenario, a survey was conducted to gather inputs from electric utilities from the EI system, national labs and research institutes. Based on the survey results, the renewable generation mix of the to-be-developed high PV simulation scenarios are defined to be 5%, 25%, 45%, and 65% PV penetration levels plus 15% wind at the interconnection level and 100% PV at the regional level (as shown in Table 2.2).

Table 2.2. Generation mix of high PV simulation scenarios in the EI

Scenario	Instantaneous Penetration Level			
	PV	Wind	PV+Wind Total	Synchronous Generation
Interconnection Level Scenario 1	5%	15%	20%	80%
Interconnection Level Scenario 2	25%	15%	40%	60%
Interconnection Level Scenario 3	45%	15%	60%	40%
Interconnection Level Scenario 4	65%	15%	80%	20%
Regional Level Scenario	100%	0%	100%	0%

This subsection aims to determine future PV distribution for the wide range of PV penetration levels defined in Table 2.2. The studies documented in [80, 81] investigated the frequency response of EI under a high wind scenario. In these studies, wind power plants displaced synchronous generators uniformly across the EI system except SERC/FRCC. Based on the literature review results, there is no readily available data that can provide interconnection-scale PV location information for the projected high PV scenarios.

In this study, the PV distribution for EI high PV penetration scenarios was obtained by optimization, which minimized the system total cost consisting of PV expansion, system operation and maintenance and emission. The optimization horizon featured an interconnection-level PV growth primarily driven by high carbon-emission prices. The optimization was conducted based on the PLEXOS tool and the dataset described in Chapter One.

The PLEXOS modelling tool[1] and the commercial mix-integer programming (MIP) solver Xpress-XP were applied to optimize the PV distribution in the projected high PV scenarios. Additional parameters in PV expansion optimization included solar radiation, PV prices, land prices, as well as associated renewable portfolio standards. In this study, the input data sources of the PLEXOS model are shown in Table 2.3. The PLEXOS optimization result included the generation mix and projected PV capacity distribution for each penetration level. Then instantaneous PV output was assumed to be 80% of its capacity in order to mimic the high PV

[1] Plexos has the capability to optimize independent generation, transmission expansion, or co-optimize them to formulate the most economic expansion/retirement plan considering reliability requirements, environmental, and policy factors. The MIP modelling and solving core provides robust modelling capabilities to incorporate multiple factors that impact the future generation or transmission growth, such as economic and technical features of existing generation/transmission facilities and candidates, long-term load forecast results, reserve margin requirements, quality of renewable resources.

output time periods during the daytime in spring/fall weekends. In the high PV penetration scenarios developed in this chapter, PV will provide a significant proportion of system reactive power so the inverter capacities of some PV plants could be larger than their MW rating. In this study, PV inverters are assumed to have enough capacity to provide reactive power during frequency disturbance events.

Table 2.3. PLEXOS model input data sources

PLEXOS model input	Data sources
• Existing generation and transmission infrastructure • Load forecast • Solar radiation • Fuel price forecast • Carbon emission price forecast	• The Eastern Interconnection Planning Collaborative (EIPC) database [51]
• PV price forecast	• North American PV Outlook [82]
• PV sitting land price	• Land Value 2015 Summary [83]

The distribution of wind power was obtained from Ref.[7] and is presented in Figure 2.2. It shows that substantial proportions of wind are in Nebraska, MISO and SPP, as well as in NYISO and NEISO regions. These regions are often projected as the major locations of future wind farms in many other studies due to rich wind resources [84].

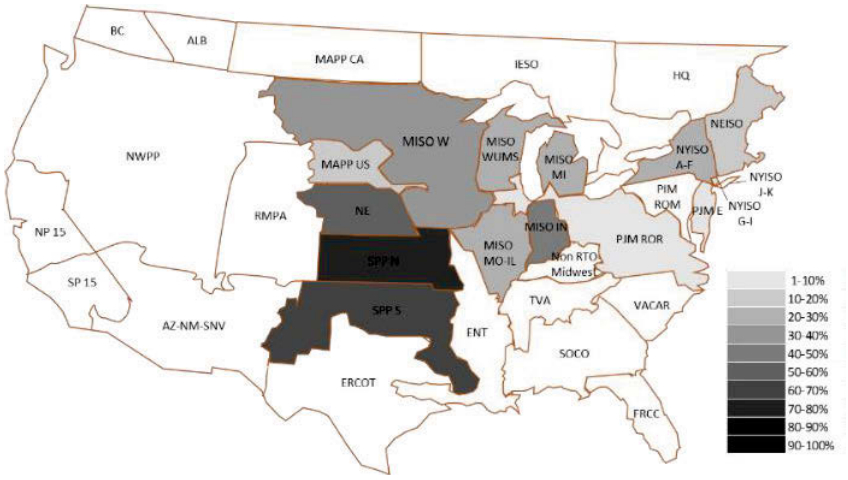

Figure 2.2. 15% wind power distribution in EI

Based on PV expansion optimization results, the PV geographical distribution for all penetration levels are obtained and the PV distribution for difference penetration scenarios is shown in Figure 2.3 to Figure 2.6. In the 80% renewable case, PJM_ROR has the largest PV output while the PJM_ROM has the highest PV penetration level. In contrast, SPP_N and SPP_S are dominated by wind (more than 70%). Furthermore, the regions in southern EI and those close to load centers tend to have more PV distribution. That is because the southern regions have higher solar radiation, which leads to higher PV capacity factors and thus more economic benefits by reducing carbon emission and fuel costs, while regions close to load centers have higher local marginal prices, meaning more economic surplus for the same level of PV output. Figure 2.7 to Figure 2.10 shows detailed PV distributions for the four renewable penetration levels. Considering wind power, the renewable geographical distribution in EI is shown in Figure 2.11 to Figure 2.14.

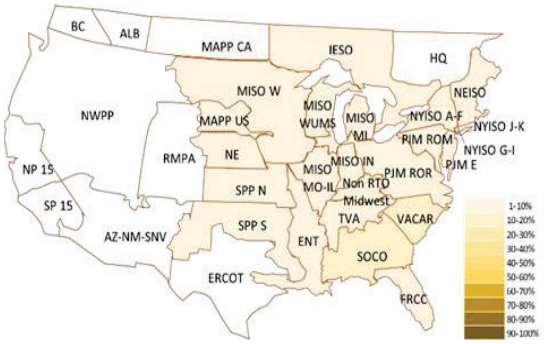

Figure 2.3. PV regional distribution in 20% renewable (5% PV+15%WT)

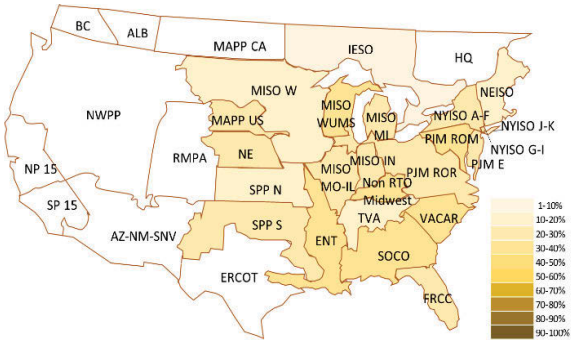

Figure 2.4. PV regional distribution in 40% renewable (25% PV+15%WT)

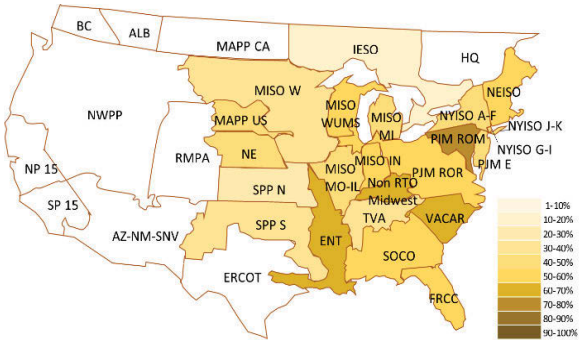

Figure 2.5. PV regional distribution in 60% renewable (45% PV+15%WT)

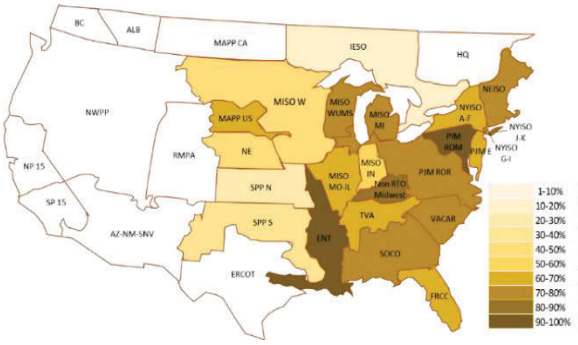

Figure 2.6. PV regional distribution in 80% renewable (65% PV+15%WT)

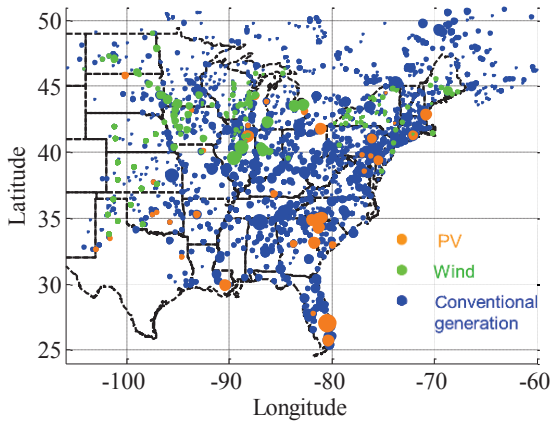

Figure 2.7. PV distribution in different scenarios (5%PV + 15%WT)

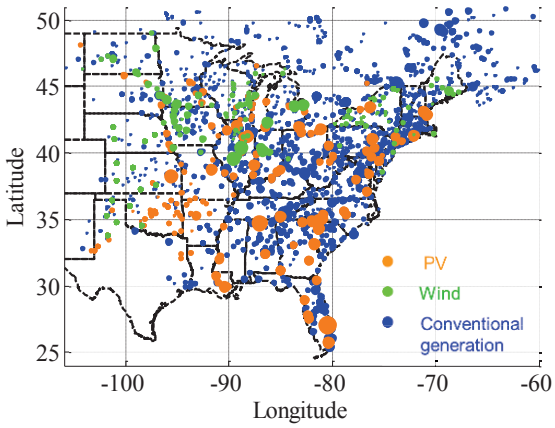

Figure 2.8. PV distribution in different scenarios (25% PV + 15%WT)

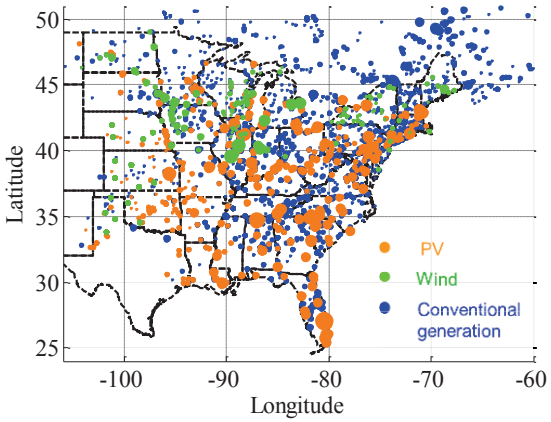

Figure 2.9. PV distribution in different scenarios (45%PV+15%WT)

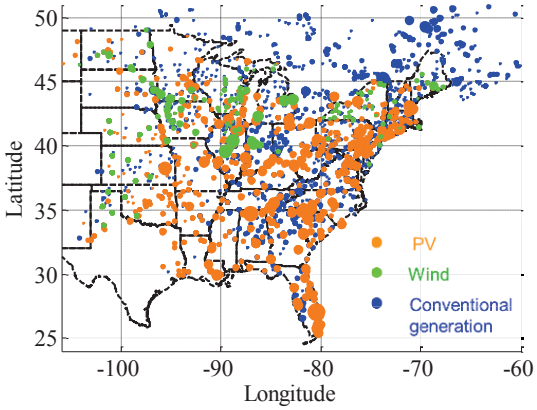

Figure 2.10. PV distribution in different scenarios (65%PV + 15%WT)

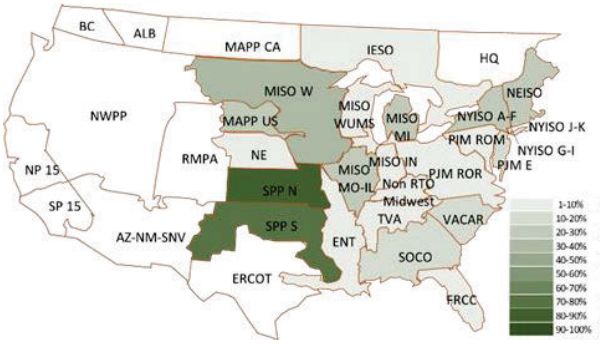

Figure 2.11. 20% renewable geographical distribution in EI

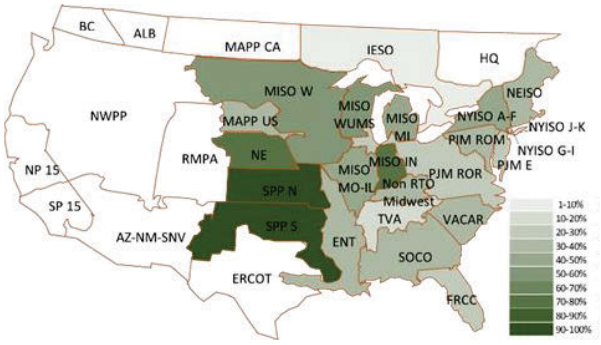

Figure 2.12. 40% renewable geographical distribution in EI

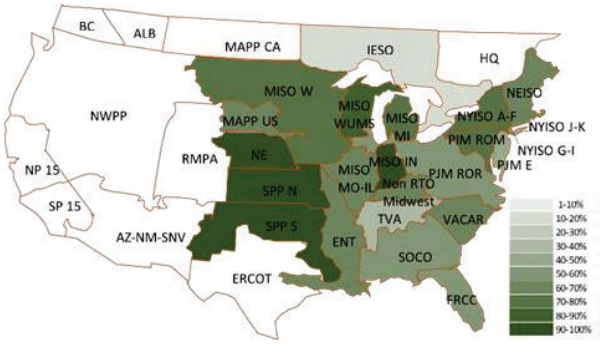

Figure 2.13. 60% renewable geographical distribution in EI

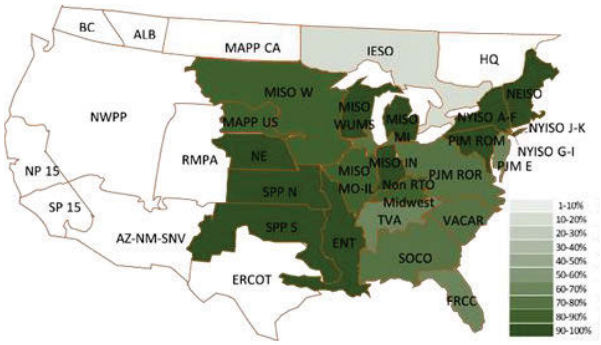

Figure 2.14. 80% renewable geographical distribution in EI

2.2.4. High PV power grid dynamic model development

Following the PV distribution optimization, the second step is to incorporate the PV dynamic model into each scenario. Incorporation of the PV dynamic model into system models includes four procedures as shown in Figure 2.15.

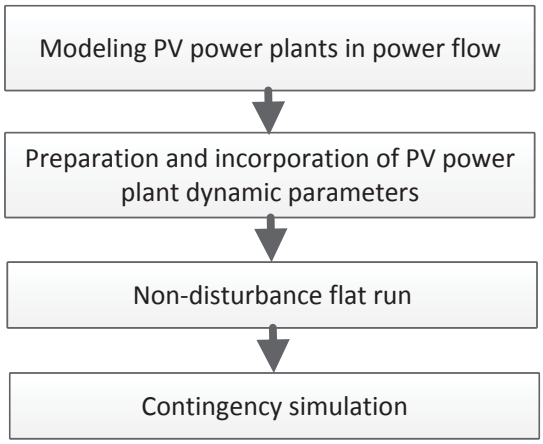

Figure 2.15. Flowchart of developing high PV dynamic models

1) Modeling PV power plant in power flow

The first step is modeling PV power plants in power flow. In this step, the distribution of PV is kept consistent with the PV siting optimization result. In general, PV have similar steady state settings with synchronous generators in terms of power flow modeling in commercial software (such as PSS/e and PSLF), expect for some minor modifications on the power flow parameters to incorporate dynamic models. For example, special attentions need to be paid to three parameters: the MVA rating, X_{src} (generator internal reactance) and R_{src} (generator internal resistance). Typically, X_{src} and R_{src} are set to 99999.0 and 0.0, respectively, to model power electronics interfaced generators in commercial software. The instantaneous capacity factors of PV plants in a system varies with time and among plants in different locations. For simulating a typical circumstance, a uniform capacity factor can be assumed for the study scenario.

The MVA rating is then derived based on the real power output in the power flow and the capacity factor.

2) Preparation and incorporation of PV power plant parameters

Figure 2.16 shows the connectivity diagram of the PV dynamic model. The details of the converter and controllers of a PV power plant can be found in [85]. Actual PV power plants parameters are ideal for building existing system models. Since these are future scenarios, generic dynamic parameters of PV power plants are adopted for the models [85], as shown in Table 2.4 and Table 2.5. In commercial software, such as PSS/e and PSLF, the PV dynamic model can be incorporated into the validated dynamic model through a user-defined model. Proper control modes, such as voltage control and power factor control, should be selected or defined according to simulation purposes before running dynamic simulation test. Typical parameters of the PV inverter and electric controller models are listed in the tables of the Appendix. Table 2.6 shows the two typical control strategies for PV power plants in North America [86]. As the normal configuration, the Volt/Var control with SolarControl (Strategy 1) is selected as the base strategy.

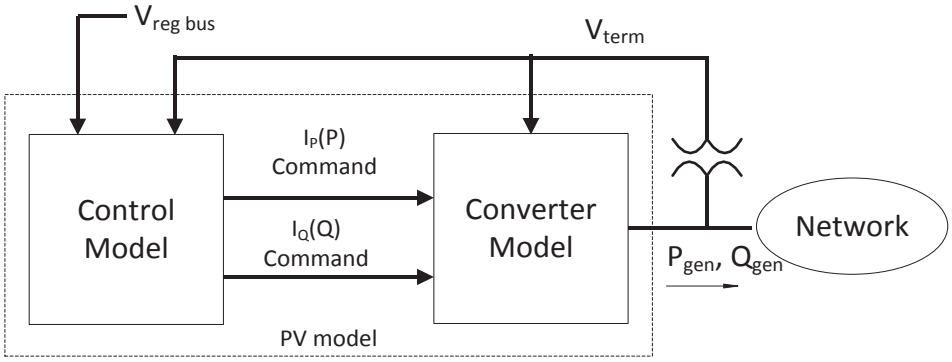

Figure 2.16. PV dynamic model connectivity [85]

Table 2.4. PV converter model ‘GEPVG’ generic parameters

Parameter	**Value**
Xeq-equivalent reactance for current injection	99999
VHVRCR2- HVRCR voltage 2	1.2
CURHVRCR2- Max. reactive current at VHVRCR2	2.0
RIp_LVPL-Rate of active current change	5.0
T_LVPL-Voltage sensor for LVPL	0.02
LVPL voltage 1	0
LVPL power 1	0
LVPL voltage 2	0.5
LVPL power 2	0.167
LVPL voltage 3	0.9
LVPL power 3	0.98
XLVPL	0

Table 2.5. PV electrical controller ‘GEPVE’ generic parameters

Parameter	**Value**
Tfv - V-regulator filter	0.15
Kpv - V-regulator proportional gain	18.0
Kiv - V-regulator integrator gain	5.0
Rc - line drop compensation resistance	0
Xc - line drop compensation reactance	0
QMX - V-regulator max limit	1.0
QMN - V-regulator min limit	-1.0
IPMAX - Max active current limit	1.12
TRV - V-sensor	0.02
KQi - MVAR/Volt gain	0.1
VMINCL	0.88
VMAXCL	1.15
KVi - Volt/MVAR gain	120
XIQmin - min. limit for Eq'cmd	0.55
XIQmax - max. limit for Eq'cmd	1.55
Tv - Lag time constant in WindVar controller	0.05
Tp - Pelec filter in fast PF controller	0.05
Fn - A portion of on-line PV converters	1.0
ImaxTD - Converter current limit	1.12
Iphl - Hard active current limit	1.12
Iqhl - Hard reactive current limit	1.12
TIpqd - Reactive droop time constant	5.0
Kqd - Reactive droop gain	0.0
Xqd - Reactive droop synthesizing Impedance	0.0
Vermx - Reactive power control maximum error signal	0.01
Vermn - Reactive power control minimum error signal	-0.01
Vfrz - Reactive power control freeze voltage	0.7
PFAFLG: (=1 if PF fast control enabled)	0
VARFLG: (=1 if Qord is provided by SolarVar)	1
PQFLAG: (=1 for P priority, =0 for Q priority)	1

Table 2.6. PV plants control strategies [85]

PV control strategies	Description
Strategy 1: Volt/Var control with SolarControl[2]	Current configuration of North American PV plants
Strategy 2: Volt/Var control without SolarControl	SolarControl turned off and a slow reset of reactive power

3) Non-disturbance flat run and contingency simulation

To ensure the developed dynamic models are ready for dynamic studies, dynamic simulation testing on these models is required. In this study, both the twenty seconds' non-disturbance scenario and typical N-1 contingency scenarios are tested to validate the numerical stability of the developed dynamic cases. If examining the rotor speed deviation, a successful flat run will show very small ripples due to very small numerical errors. A converged contingency run will obtain an expected change in system overall frequency in addition to some common phenomenon, such as electromechanical wave propagation, local and inter-area oscillations.

2.3. Impact of high PV on frequency response

This section studies the impact of PV on the EI frequency response using the PV penetration scenarios. The wind model adopts the GEWT Type 3 model and the PV model applies the GEPV model. The simulation is performed in PSS/e.

The frequency responses of the EI system after a generation trip of 1,128 MW is given in Figure 2.17 and the corresponding frequency response metrics including ROCOF, nadir, settling time and settling frequency are shown in Table 2.7.

[2] The SolarControl function monitors a specified bus voltage and compares it to a reference voltage.

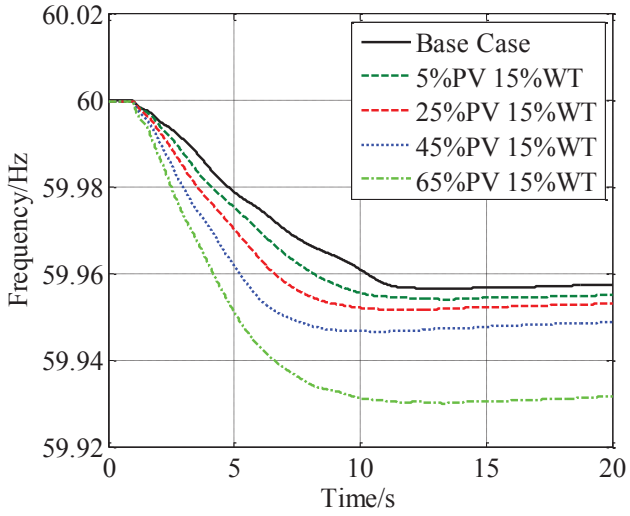

Figure 2.17. EI frequency response change due to renewable integration (1.128 GW generation loss)

Table 2.7. EI frequency response metrics change due to renewable generation

Frequency response metrics	Base case	20%	40%	60%	80%
ROCOF (mHz/s)	5.0	6.8	8.8	9.7	12.2
Nadir (Hz)	59.956	59.954	59.952	59.947	59.930
Settling time (s)	14	13	11	9	12
Setting frequency (Hz)	59.957	59.955	59.954	59.949	59.932

From Figure 2.17, it is obvious that the EI system does not have obvious frequency recovery under various PV penetration, which is similar to the current frequency response in EI [87]. As shown in Table 2.7, though the EI 20% case does show a larger ROCOF (6.8 mHz/s compared with 5.0 mHz/s), the nadir and setting frequency of EI 20% case is only slightly influenced. This demonstrates that 20% renewable power integration will not change the EI system frequency response dramatically. For the EI 40% and 60% cases, ROCOF keeps getting larger and frequency nadir/settling frequency gets lower. Particularly, the ROCOF of the 60% case is almost twice of that of the base case. Unlike the dramatically increased ROCOF, a 9 mHz (from 59.956Hz to 59.947Hz) nadir change is not dramatic. When the renewable penetration rate reaches 60% to 80%, the system frequency response performance dramatically decreases. Since the under-frequency load shedding (UFLS) threshold for typical utilities EI is around 59.5 Hz, this result tends to indicate that, despite a much steeper frequency decline rate, 80% renewable is unlikely to trigger many UFLS in the EI system, which means 80% instantaneous renewable penetration may be tolerable for the EI system frequency response. This is mainly due to the extensive size of the EI system. However, considering the EI frequency response has been steadily declining during the past two decades [76], the impact of renewable integration should be closely watched and appropriately mitigated.

Examining regional frequency response, it is found that when a disturbance happens in a region where its coupling to the main system is relatively loose, it is possible to observe a dramatic decrease of regional frequency under high PV penetration. Figure 2.18 shows an example that a generation trip event happens in Florida for the base case and the 80% renewable case. The regional instantaneous frequency will cross the FRCC UFLS threshold, activating load shedding in FRCC.

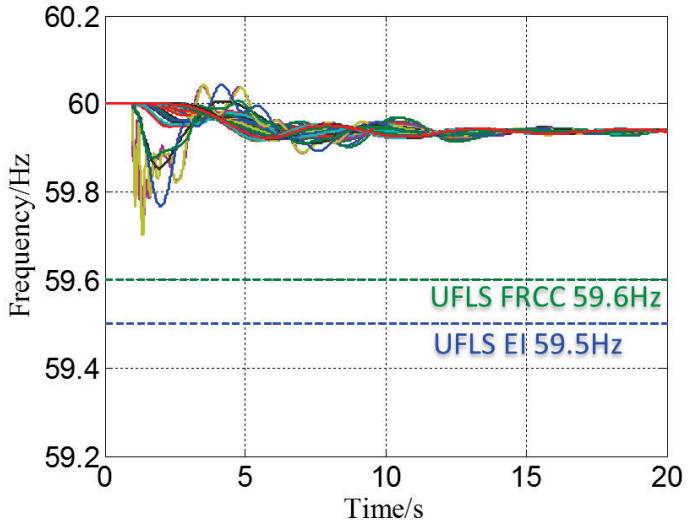

(a) Base case

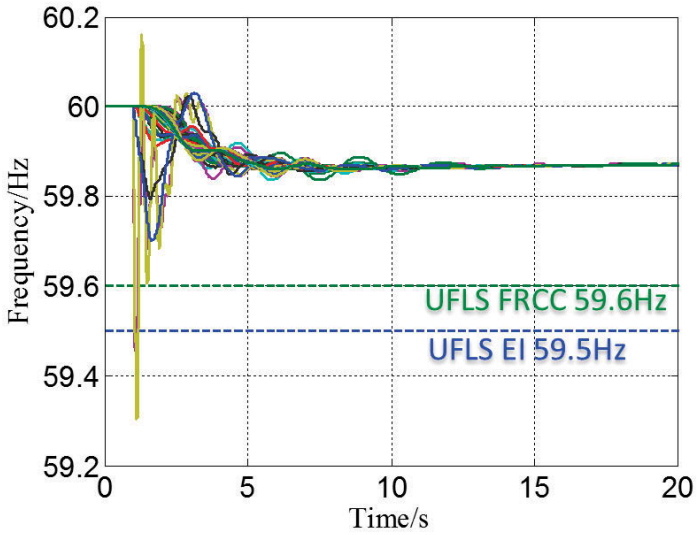

(b) 80% renewable case

Figure 2.18. PV penetration's effects on local frequency and UFLS

The voltage/Var control mode of PV plant also has impact on the system frequency response. Figure 2.19 shows a comparison of the frequency responses of voltage control and the power factor control (equivalent to constant reactive power control as real power output keeps constant in this case). It shows that the power factor control of PV plants has smaller ROCOF, higher nadir and settling frequency. The reason is that the power factor control mode allows a slight drop of bus voltage, which leads to decrease of active power in load. Figure 2.20 shows a comparison of voltage of a bus under different voltage/var control modes. It indicates that the voltage decrease in power factor control is very small (0.1%), which usually would not influence system security. A check on the bus with the maximum decrease of voltage, which is the POI bus of the tripped generator, shows a 0.015 p.u. difference between voltage control (0.965 p.u.) and power factor control (0.95 p.u.). This result indicates the potential capability of fast voltage/var control of PV power plants in improving system frequency stability.

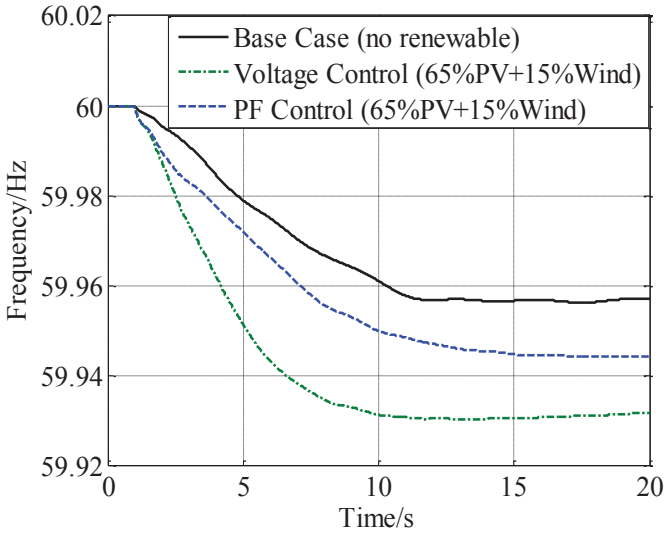

Figure 2.19. PV plants control mode's impact on system frequency response.

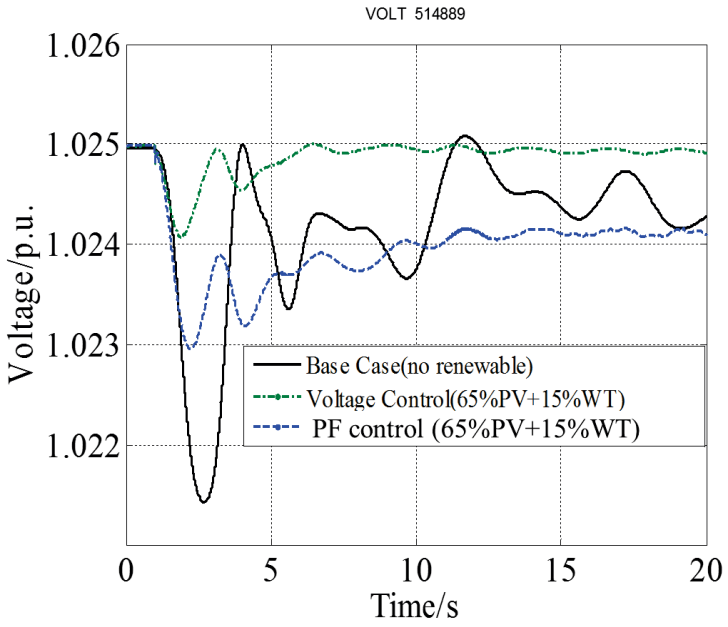

Figure 2.20. Voltage profile of Bus 514889 using different PV control mode.

2.4. Conclusion

This chapter used the measurement-validated EI system model to study the frequency response under up to 65% PV penetration (total renewables up to 80%). The result shows that the system frequency response performance decreases non-linearly when the increase of PV penetration. EI system frequency response will decrease dramatically when the renewable penetration increases to 60% to 80%. In addition, regional frequency could drop much sharper and activate UFLS. Under high PV penetration. By controlling the voltage and thus real power consumption, the voltage/var control modes of PV power plants have some potential to improve EI frequency response capability under high PV penetration.

CHAPTER THREE
IMPACT OF HIGH PV PENETRATION ON INTER-AREA OSCILLATIONS

3.1. Introduction

Solar photovoltaic (PV) generation grows quickly in the U.S. and worldwide, joining wind power as a major renewable energy technology. While many aspects of wind power's impact on system power grid stability has been investigated, including rotor angle stability [88-90], voltage stability [91], frequency response [61, 69, 92], and inter-area oscillations [88, 93-99], the impact of PV generation on power system dynamics has not been given enough attention.

Among all these aspects, inter-area oscillations need special attention from system operators. Poorly damped inter-area oscillations can reduce transmission line capacity, damage system generation and transmission facilities, influence power quality, and lead to cascading failures or blackouts. The impact of PV generation on power system oscillations may be attributed to various aspects. However, the findings of existing literature are not consistent. For example, the New-England and New York test system was used to investigate the PV's impact on its established inter-area oscillation mode; it was found that PV could detrimentally affect the inter-area oscillation mode as PV integration results in larger angular separation among synchronous generators [100]. Furthermore, using small signal analysis and transient simulation, the study in [101] indicated that the increase of utility-scale and residential rooftop PV may decrease damping of inter-area oscillation modes due to reduced system inertia. However, other studies have found it is also possible that PV integration could improve small-signal stability. For example, the study in [102] concluded that PV could

increase oscillation damping because PV adds damping to critical modes, and the scattered integration pattern is more beneficial than the concentrated pattern. Other studies that have similar findings include [103] and [104]. Additionally, other literature observed both beneficial and detrimental influence of PV on oscillations. Ref. [105] studied the impact of increased PV on system small signal stability based on a single-machine infinite-bus system. It was found that PV could either have positive or negative impact on oscillation damping. Similar findings can be found in [96] and [106]. The operation limit of PV also plays a significant role on the contribution of PV's damping torque. Ref. [64] studied the impact of distributed PV and large PV farms on system stability and found that damping does not vary significantly with the increase of either PV type.

Obviously, the impact of PV on power system inter-area oscillations is not yet well understood. Since there are so many factors that may play a role in this phenomenon, the impact of PV on inter-area oscillations may need to be studied on a case-by-case basis at this stage. Therefore, the United States Eastern Interconnection (EI) is used as a case study in this chapter to investigate the impact of PV generation on a large interconnected power grid. Specifically, by incrementally displacing synchronous generators with PV in the EI dynamic model, how the dynamics of PV affect inter-area oscillation frequency and damping ratio will be illustrated. The following sections present the procedures and details in model development, time-domain dynamic simulation, and analytical analysis [107].

3.2. Current oscillation analysis in the EI using FNET/GridEye measurements

Since the EI covers a wide area, inter-area oscillation is an important issue for system operators and planners [108, 109]. Our previous study shows that the

inter-area oscillation modes are observable by FNET/GridEye, which is a wide-area measurement system deployed at the distribution level [110, 111]. Before analyzing the impact of PV on oscillations of the U.S. EI, this section analyzes the characteristics of inter-area oscillations in the EI based on FNET/GridEye wide-area measurements during 2013 to 2015 using the Matrix-Pencil method [112, 113]. Figure 3.1 shows the frequency distribution of the dominant oscillation modes, while Figure 3.2 shows the distribution of the damping ratio of the same. The frequency of the dominant oscillation of the EI is around 0.2 Hz and the center of the damping ratio is close to 10%. Additionally, both distributions show patterns with long tails, similar to the Beta distribution. The slight shifting of oscillation frequency and damping can be explained by seasonal and daily load variations.

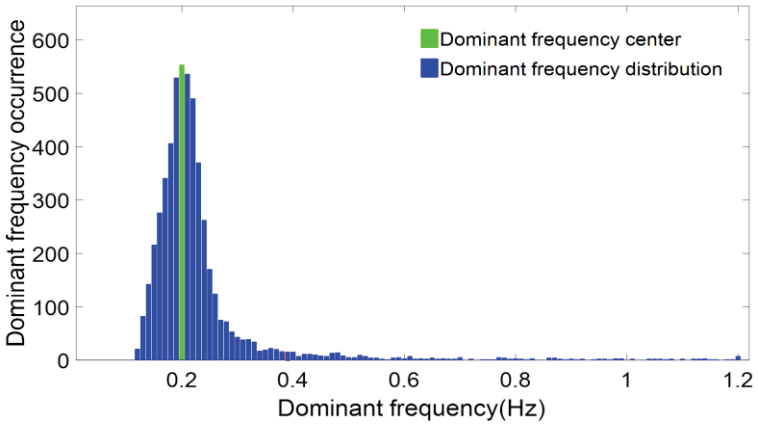

Figure 3.1. Dominant frequency distribution of inter-area oscillations [114]

Table 3.1 shows the oscillation frequency and damping ratio of different years. The oscillation characteristics are relatively stable in past years. The frequency center changed slightly from 2014 to 2015 (0.21 Hz to 0.20 Hz). This can be explained by the increase of renewable generation in the EI. Since 0.2 Hz is the

dominant oscillation mode in the EI, this mode will be the study focus in the rest of this chapter.

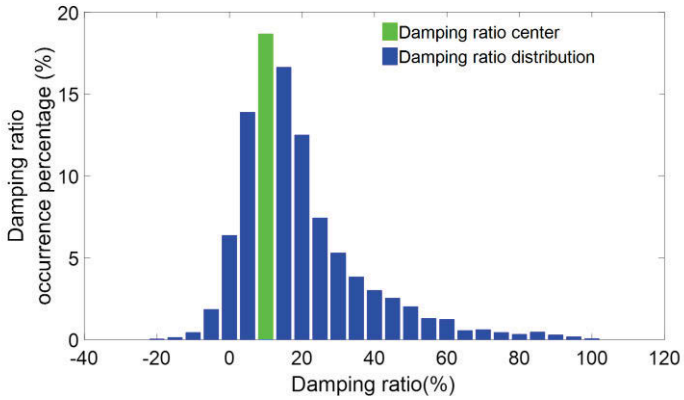

Figure 3.2. Damping ratio distribution of inter-area oscillations [114]

Table 3.1. Oscillation frequency and damping ratio

Year	**2013**	**2014**	**2015**
Dominant frequency center (Hz)	0.21	0.21	0.20
Damping ratio center of the dominant frequency (%)	10	10	10

3.3. Impact of high PV on EI oscillation modes

The EI is a geographically dispersed power grid. To capture its inter-area oscillation modes, multiple observation locations across the EI are necessary to mitigate the impact of local oscillations and obtain more reliable results from inter-area oscillation analysis. The observation locations in this study are shown in Figure 3.3 To analyze the oscillations observed at each observation point, the Matrix Pencil method is applied to the bus frequency at each location [115]. The oscillation analysis results from all observation locations are combined to form a

more complete picture of oscillation trends. These procedures are conducted under four scenarios, specifically 5%, 25%, 45%, and 65% PV penetration.

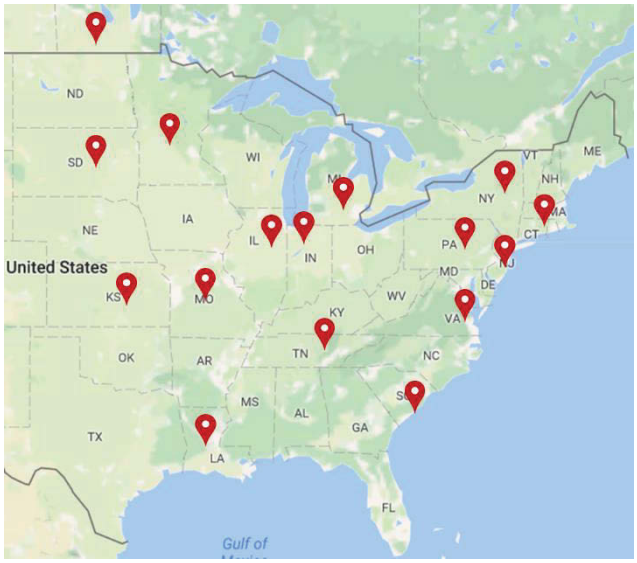

Figure 3.3 Observation locations in the U.S. EI

3.3.1. Impact on frequency and damping ratios

system and the frequency response is recorded at multiple locations. This disturbance is a three-phase fault on a 500 kV bus located in the central EI lasting for two cycles. Using Matrix Pencil analysis to analyze the oscillation modes at multiple locations, the frequency and damping ratios of the 0.2 Hz inter-area oscillation mode at each observation location are calculated. The change of oscillation frequency and damping ratios with PV penetration are shown in Figure 3.4 and Figure 3.5, respectively. It can be noted that as PV penetration increases from 5% to 65%, the oscillation frequency increases almost linearly from 0.20 Hz to 0.28 Hz, and the damping ratio decreases from around 9% to 6%. The distribution of the damping ratio

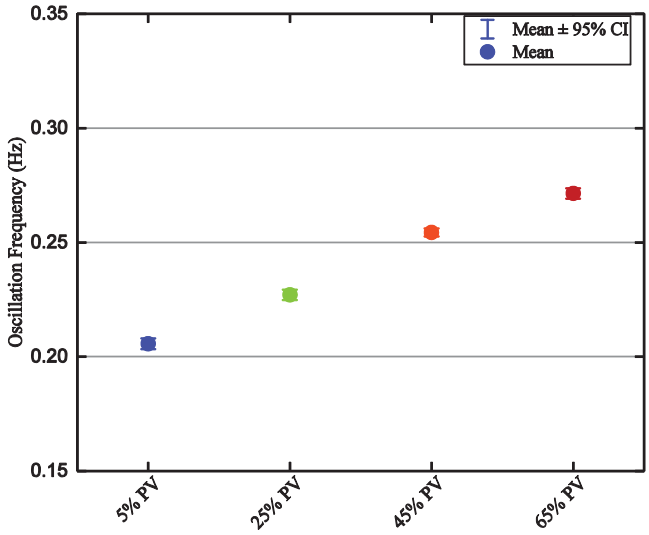

Figure 3.4 Oscillation frequency change as PV penetration increases

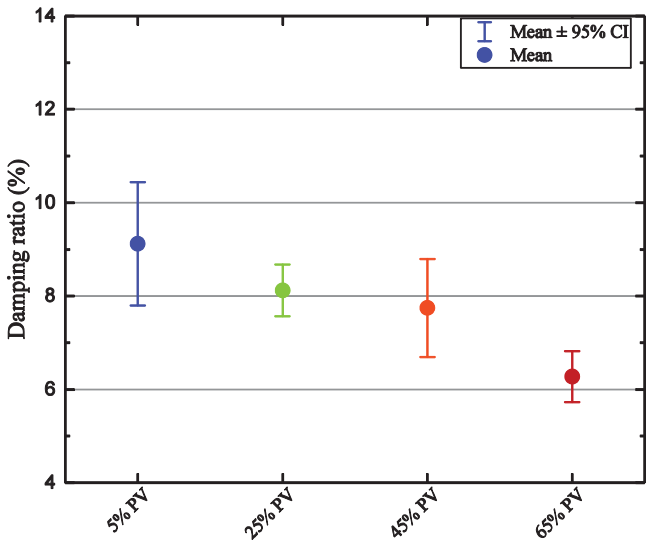

Figure 3.5 Oscillation damping ratio change as PV penetration increases

Figure 3.6 and Figure 3.7 shows the frequency profiles of two different locations: Connecticut (CT) and Tennessee (TN), respectively. It can be seen from Figure 3.6 that the oscillation frequency increases, but the amplitude and damping decreases as PV penetration increases. In TN (Figure 3.7), while the change of this inter-area oscillation mode is similar to that of Connecticut, there is an obvious local oscillation as well due to the proximity of the disturbance location. The frequency of this local oscillation is around 15 Hz for the 65% PV penetration scenario. It can be noted that this oscillation frequency increases with PV penetration, indicating that this oscillation mode change is related to the reduction of system inertia.

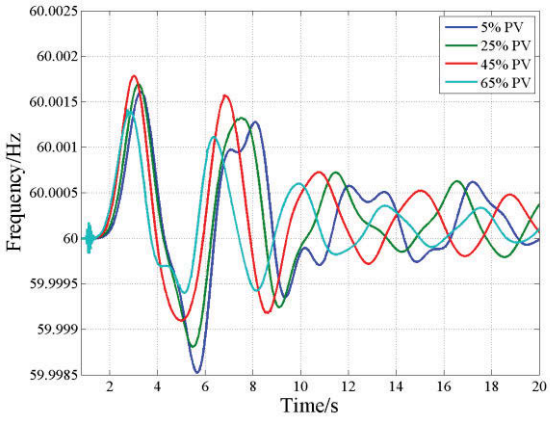

Figure 3.6 Oscillation frequency change as PV penetration increases (CT)

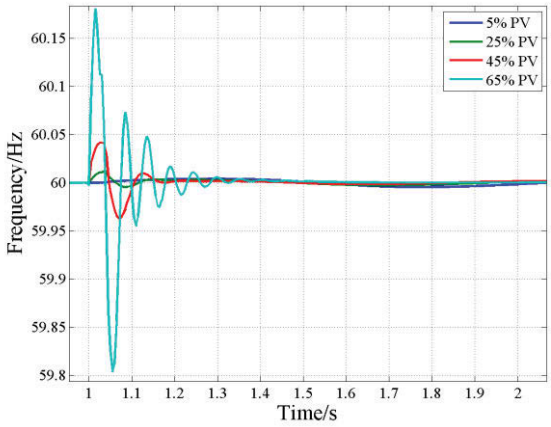

Figure 3.7 Local oscillation changes as PV penetration increases (TN)

3.3.2. Impact on mode shape

The mode shape describes the angular information of an oscillation mode and can be used to design additional damping controls. Figure 3.8 shows the oscillation mode under different PV penetration levels. The 0.2 Hz inter-area oscillation mode has two main coherent groups: Northeastern EI (NY, PA, CT, and NJ, etc.) and Western EI (MB, MN, and KS, etc). As PV penetration increases, the angular difference between buses within each group decreases, indicating the increase of coherence between generators within each group due to the decrease of conventional generation.

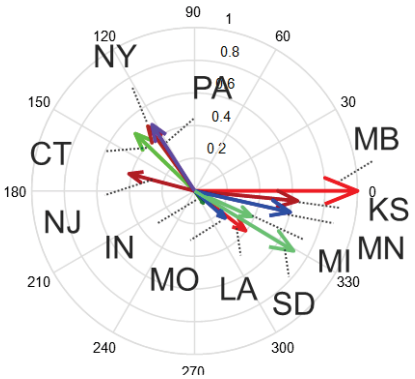

(a) 5% PV

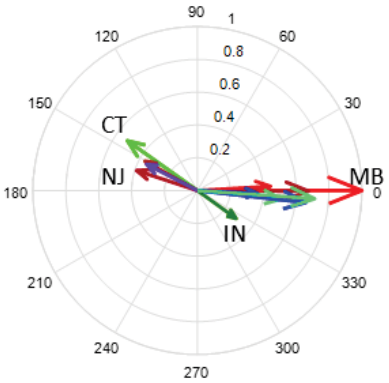

(b) 25% PV

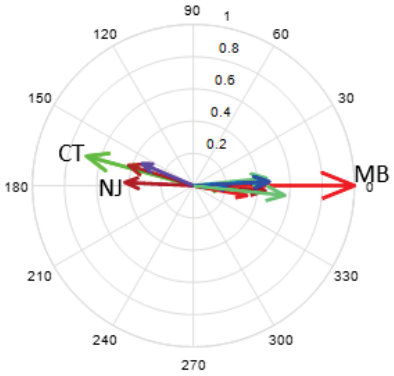

(c) 45% PV

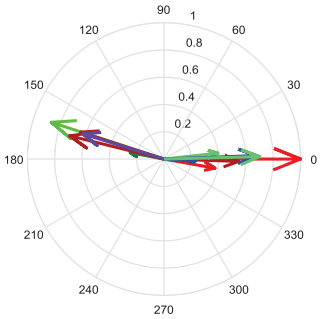

(d) 65% PV

Figure 3.8 Mode shape change with PV penetration

3.3.3. Impact of PV plant control strategies on inter-area oscillations

The control strategies of PV power plants impact inter-area oscillation modes. For a comparison with Control Strategy 1 (Volt/Var control with SolarControl), Control Strategy 2 (Volt/Var control without SolarControl) is applied to all PV plants. Figure 3.9 contrasts the frequency profile of a bus in CT under both control strategies in the 65% penetration scenario. It can be seen that the system oscillation frequencies under the two control strategies are close, but Control Strategy 2 has a smaller oscillation amplitude and damping ratio, due to the slower reset of reactive power from PV plants after the disturbance.

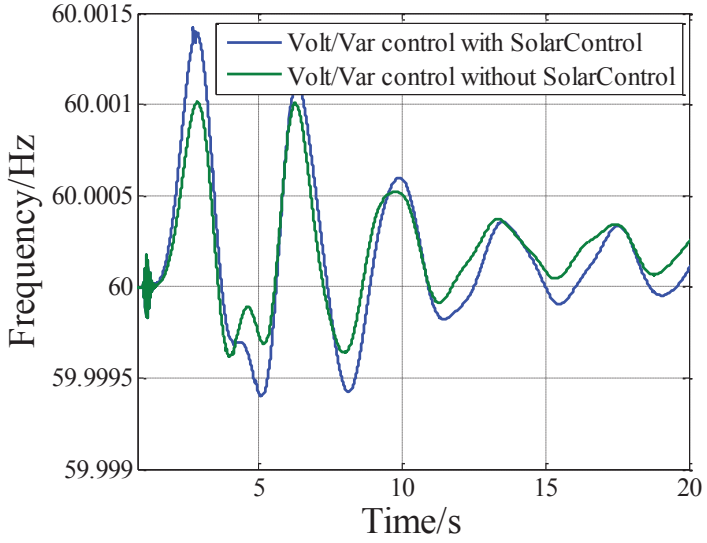

Figure 3.9 Oscillation frequency in CT under different PV power plant control strategies (65% PV)

Figure 3.10 shows the oscillation mode shape under Control Strategy 2. The oscillation mode shape also includes two separate groups, similar to Control Strategy 1 (Figure 3.8 (d)). but with some differences in phase angles, especially at grid edges such as New Jersey and Manitoba, Canada. This oscillation mode

shape difference is due to the discrepancy in reactive power output under the two PV control strategies.

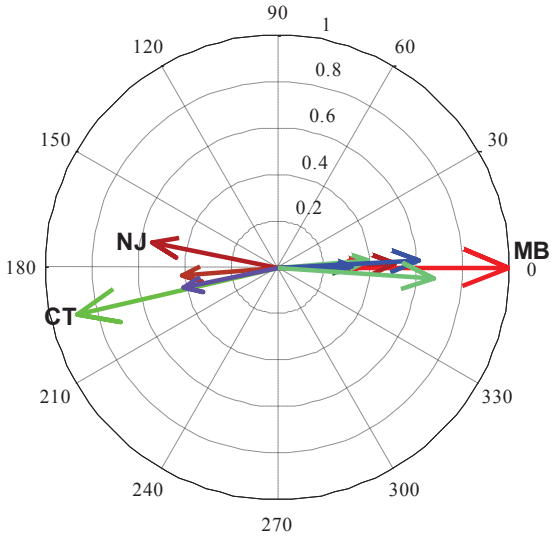

Figure 3.10 Oscillation mode shape at 65% PV (Control Strategy 2)

3.3.4. Introduction of new inter-area oscillation modes under certain PV plant control settings

Certain control parameters can introduce new oscillation modes. The initial reactive power regulator gain value is increased from 0.1 to 0.5 in Control Strategy 1. Applying the same disturbance as before, the frequency profiles at a 138 kV bus in Illinois (IL) for the 65% PV scenario under the two different settings are shown in Figure 3.11 and Figure 3.12. A 1.2 Hz inter-area oscillation mode can be easily seen after the disturbance for the case with a higher reactive power gain. Figure 3.13 shows the mode shape of the 1.2 Hz oscillation mode. It can be noted that large oscillation locations include MI, IL, and VA.

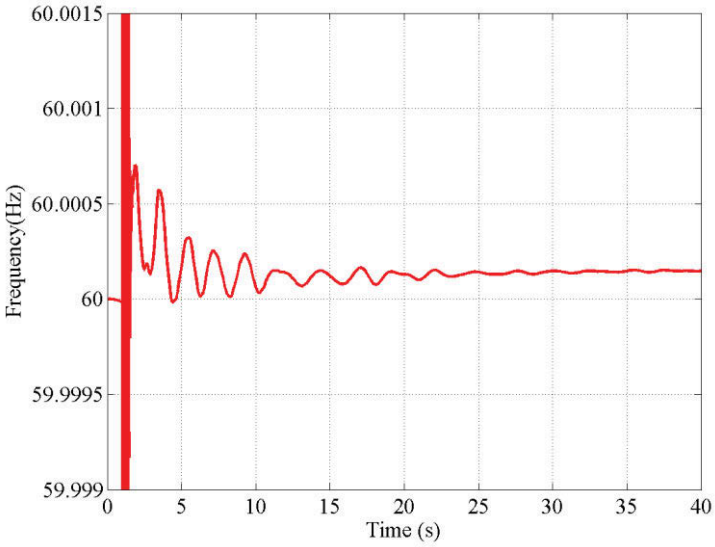

Figure 3.11 Frequency profile in IL under Control Strategy 1 (Volt/Var control with SolarControl) (65% PV)

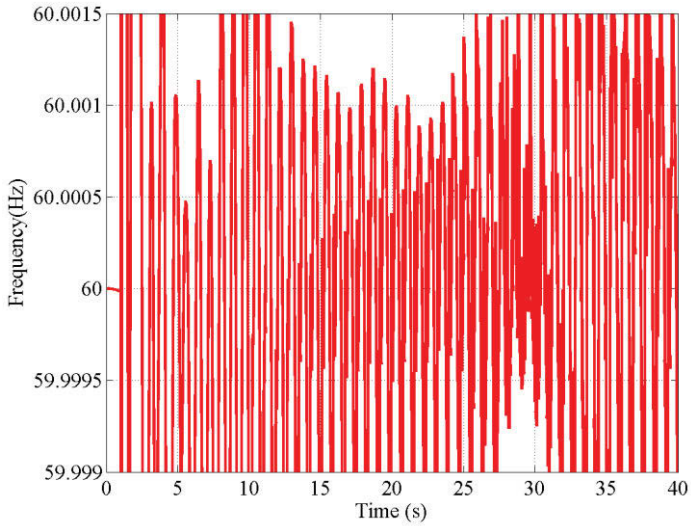

Figure 3.12 Frequency profile in IL under Control Strategy 1 with fast power factor control (65% PV)

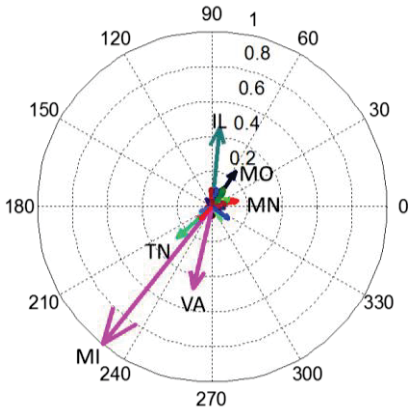

Figure 3.13 Mode shape of the 1.2 Hz Inter-area mode (65% PV)

Figure 3.14 and Figure 3.15 show the changes in frequency and damping ratios of this new oscillation mode for multiple PV penetration levels. Unlike the 0.2 Hz mode, the frequency and damping ratios of the 1.2 Hz mode barely change with PV penetration. This insensitivity is seen because the PV controllers, which are not influenced by time constants related to system inertia, cause this oscillation mode.

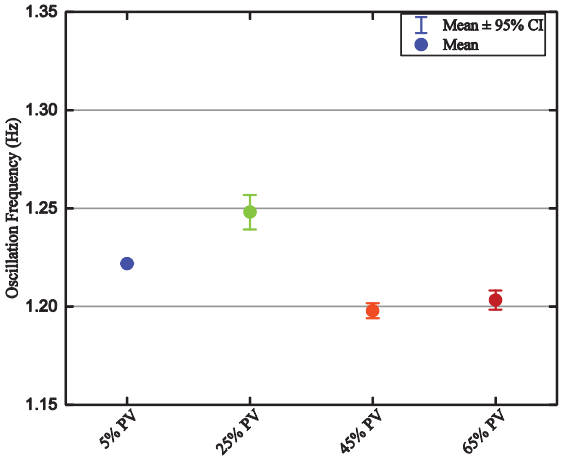

Figure 3.14 Oscillation frequency change with PV penetration (1.2 Hz mode)

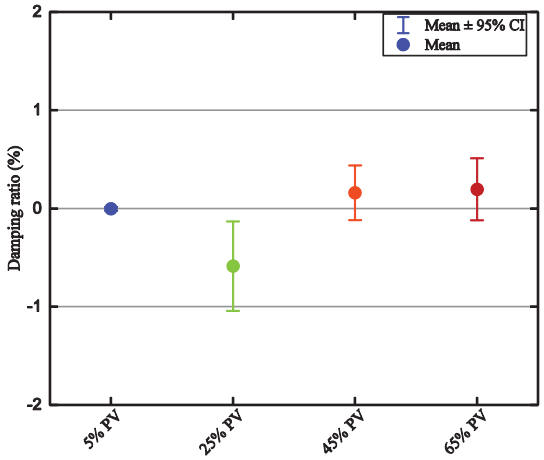

Figure 3.15 Damping ratio change with PV penetration (1.2 Hz mode)

3.4. Conclusions

Based on detailed dynamic system models, this chapter studied the impact of high PV penetration on the inter-area oscillation modes of the U.S. EI. The analytical procedures include dynamic model development, PV plant siting, time-domain transient simulation, and Matrix Pencil analysis. Changes in oscillation frequencies, damping, and mode shapes, as well as the introduction of new oscillation modes, are studied by varying PV penetration levels, control strategies and parameters. It is found that oscillation damping decreases as PV penetration increases in the system, indicating that additional operation and planning consideration may be required to increase oscillation damping as PV penetration increases in the future. Variations in PV control strategies and parameters are found to impact mode shape and can create new oscillation modes.

CHAPTER FOUR
IMPACT OF HIGH PV ON TRANSIENT ROTOR ANGLE STABILITY AND ELECTROMECHANICAL WAVE PROPAGATION

4.1. Introduction

As PV generation provides no inertia to the system, the electromechanical dynamics of the system is expected to be influenced in all dimensions. This chapter discusses other two important issues related to power grid electromechanical dynamics: transient rotor angle stability and electromechanical wave propagation. Transient rotor angle stability focuses on the dynamics of rotor angles and their capability of keeping synchronization. Transient rotor-angle stability is one important dimension of transient stability and it is directly related to the system security [116, 117]. Electromechanical wave propagation is the propagation of angle deviation from the disturbance location to the entire synchronized system. Electromechanical wave may influence various protections and it is important for wide-area protection and control. This chapter will first focus on the impact of PV on transient rotor angle stability using the out-of-step stability case between Florida and the rest of the EI. Then tis chapter will investigate the change of electromechanical wave propagation under high PV penetration in the U.S. EI system.

4.2. Impact of high PV penetration on transient stability — case study of FRCC out-of-step stability

4.2.1. Background

According to the technical review committee (TRC), Florida Reliability Coordinating Council (FRCC) may be separated from main EI after a large generation loss in Florida if the two 500kV tie-lines connecting FRCC and main

EI are already heavily-loaded before the generation loss, causing an out-of-step (OOS) instability issue. The generation loss magnitude is about 3 GW, which may occur during a grid disturbance or the natural disaster, such as thunderstorms and hurricanes. The two 500 kV tie-lines (Duval-Hatch and Duval-Thalmann) are shown in Figure 4.1. This OOS issue occurs because much more power will flow from main EI to FRCC after a Florida generation loss and these two lines will be overloaded and tripped by the line protections. Since this OOS issue will make FRCC lose synchronization and support from main EI, TRC suggested to examine the impact of high PV penetration on this issue.

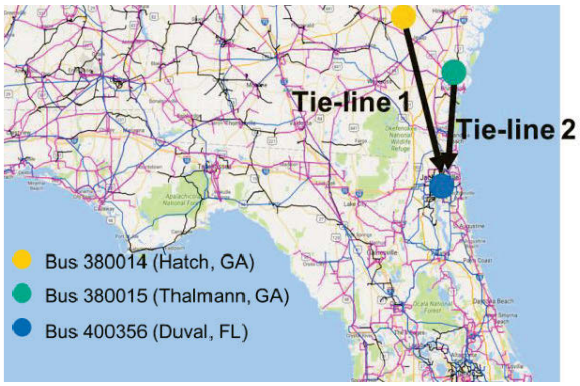

Figure 4.1. Two 500kV tie lines between FRCC and main EI

4.2.2. Approach

To replicate the heavily-loaded tie-lines, the original tie-line power flows were increased according to the TRC's suggestions, as shown in Table 4.1. Then contingencies with different generation loss amounts were simulated in FRCC to examine whether this OOS issue occurred. As two example, Figure 4.2 and Figure 4.3 show the DUVAL-HATCH 500kV tie-line voltage phase angle difference after the loss of 2.0 GW and 3.5 GW generation in FL, respectively. The loss of 2.0 GW generation in FL did not result to out of step between FL and EI, while the 3.5 GW generation loss in FL caused out-of-step instability.

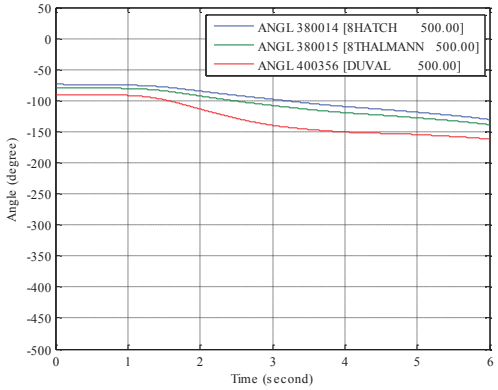

Figure 4.2. DUVAL-HATCH 500kV tie-line voltage phase angle difference after the loss of 2.0 GW generation in FL

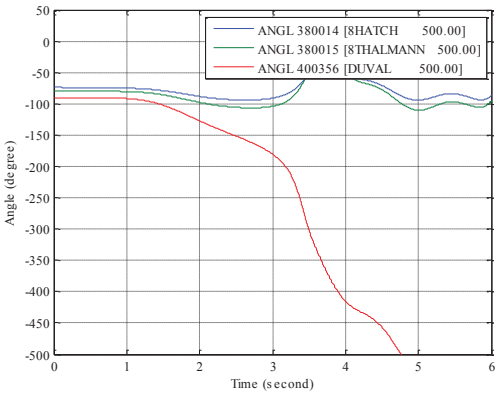

Figure 4.3. DUVAL-HATCH 500kV tie-line voltage phase angle difference after the loss of 3.5 GW generation in FL

Table 4.1. Increased tie-line flows

Tie line	Tie-line Flow when heavily-loaded
Line 1 (Duval-Hatch 500kV)	1,150MW
Line 2 (Duval-Thalmann 500 kV)	1,250MW

4.2.3. Results and discussion

Results of various generation loss amounts and PV penetration rates are shown in Table 4.2, OOS occurred after a 2.1 GW generation loss in 40%, 60%, and 80% renewable scenarios but not in the base case and 20% scenario while OOS occurred after a 2.0 GW generation loss only in 80% renewable scenario. These results indicate that, with the increasing PV penetration level, FRCC becomes more vulnerable to the OOS instability issue. This can be explained by that FRCC will gradually lose its own frequency regulation capability due to the reduction of synchronous units and rely more on the power imports from the two tie-lines. Countermeasures to mitigate this OOS issue may include engaging PV plants in FRCC frequency control and strengthening the tie-lines between FRCC and main EI.

Table 4.2. FRCC OOS test results with increased tie-line flows

Contigency Magnitude	Base Case	20% Renewable (8.4% PV within FRCC)	40% Renewable (29.4% PV within FRCC)	60% Renewable (52.4% PV within FRCC)	80% Renewable (69.7% PV within FRCC)
3.5 GW	OOS	OOS	OOS	OOS	OOS
2.5 GW	OOS	OOS	OOS	OOS	OOS
2.1 GW	No OOS	No OOS	OOS	OOS	OOS
2.0 GW	No OOS	No OOS	No OOS	No OOS	OOS
1.8 GW	No OOS	No OOS	No OOS	No OOS	No OOS

It is noted that this case study is conducted under a specific unit commitment and economic dispatch scenario of the system. Different renewable penetration, the variation of PV, wind power, and loads will influence the system dynamics by varying unit commitment, dispatch, and even topologies. Therefore, the study

results of this OOS issue are more meaningful from a qualitative perspective than a quantitative perspective.

4.3. Impact of high PV penetration on electromechanical wave propagation speed

4.3.1. Introduction

Synchronous generator rotor angles deviate after a disturbance in power systems. The propagation of angle deviation from the disturbance location to the entire synchronized system is referred to as an electromechanical wave. This kind of electromechanical wave has been clearly observed since the deployment of the wide-area synchrophasor measurement technology [118]. Its propagation speed was found to be much smaller than the speed of light, and therefore it was categorized as an intrinsically different wave compared with electromagnetic waves. Electromechanical wave may influence various protections, such as over-current, impedance, and out-of-step relays, as well as under-frequency load-shedding [119]. Meanwhile, the electromechanical wave propagation phenomenon had also been found to be useful in event location [120] and inertia estimation [121].

Currently, there are two categories of methods in general to study electromechanical wave propagation in power systems: simulation-based methods and measurement-based methods. Simulation methods are based on detailed power system dynamic models. Since the system configuration is constantly changing because of unit commitment etc.[122], the simulation method usually uses a typical snapshot of power flow and associated dynamic models as the study case. Comparatively, the measurement-based method is able to calculate electromechanical wave propagation speed using wide-area synchrophasor measurement data during transients.

In the literature, electromechanical wave was mainly studied through simulation-based methods. The continuum model was first proposed in [123] to model uniformly distributed machine inertia and transmission impedance. Based on the continuum model, Ref. [124] derived standard second-order wave equations to describe electromechanical waves. By aggregating local system parameters into cells, Ref. [125] relaxed constraints that the virtual grid is homogenous and isotropic in the continuum model. Ref. [126] further relaxed the assumptions, such as lossless lines and generators. In addition, the Gaussian function was applied to smooth the nodal parameters. Ref. [127] studied the propagation of electromechanical waves based on a reduced model of the U.S. Eastern Interconnection (EI) system. It was found that wave propagation speeds are higher if it propagates along the power transfer direction compared with that of the opposite direction. Some studies developed controllers to mitigate the electromechanical wave based on the wave equation derived from the continuum model [128].

The wide-area synchronized measurements of wave propagation can serve as a foundation for theoretical modeling, validation, and applications development. For example, wave propagation has been observed and studied using data from FNET/GridEye [129, 130], a wide-area measurement deployed at the distributed level. Ref. [131] proposed a method to calculate regional speeds. This study confirmed that the propagation speed has high correlations with the distribution of system inertia and network impedance. A series of applications including disturbance location have been developed based on electromechanical waves propagation recorded in FNET/GridEye measurements [121, 131, 132].

It was predicted by the ideal continuum model that the changes of power system parameters, such as line impedance and inertia, would influence electromechanical wave propagation speed [119]. As power systems are accommodating more and more power-electronics-interfaced renewable generations and energy storage facilities [133, 134], system inertia will significantly decrease [58, 135]. However, there has been few literatures that studied the potential change of wave propagation speed due to the increasing renewable generation.

This study investigates the electromechanical wave propagation in current EI system using wide-area measurements and detailed dynamic model simulations were used to provide information on wave propagation in the future system. The rest of section is organized as follows: Section 4.3.2 studies the impact of high PV penetration on electromechanical wave propagation based on detailed dynamic models of the EI. Section 4.3.3 presents study on the electromechanical wave propagation speed, inertia, and PV penetration using a simple ring system. Section 4.3.4 gives the summary.

4.3.2. Study approach and results

Using a continuum model [126], an example demonstrating that electromechanical wave propagation varies with renewable penetration in a mesh grid is shown in Figure 4.4. The left mesh grid consists of only synchronous generation units while the right grid has 80% PV generation. A significant difference can be noticed after the same load-shedding contingency happened in the centroid of the grid.

To investigate the impact of high PV penetration on electromechanical wave propagation, the EI MMWG 2030 model [135, 136] is adopted as the study case

in this section. The distribution of PV in the high PV EI model was determined by achieving the least cost of system investment and operation.

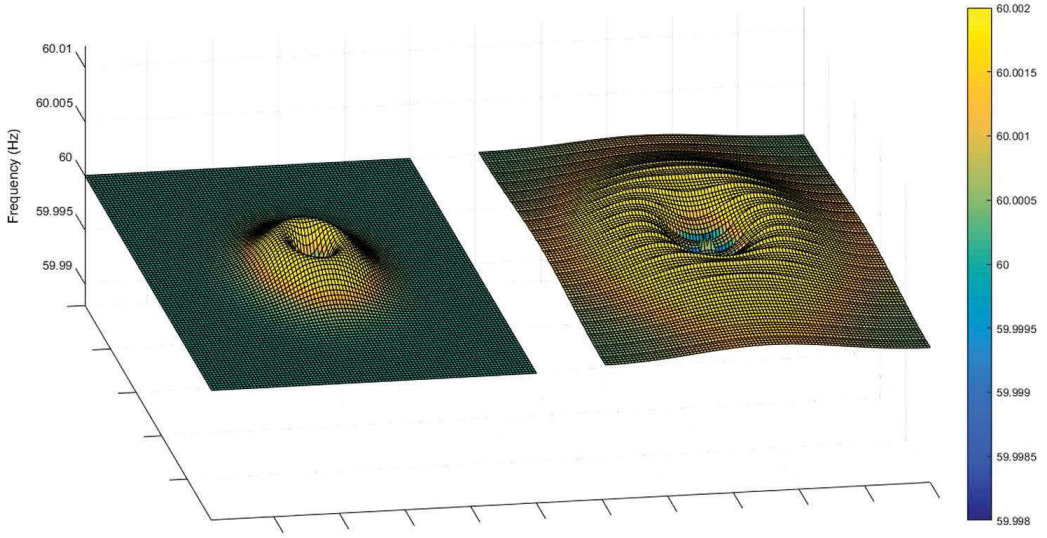

Figure 4.4. Wave propagation without PV (left) and with 80% PV (right)

The distribution of PV generation and synchronous generation for different PV penetration scenarios are shown in Figure 2.7 to Figure 2.10. It shows that PV penetration levels in southern and northeastern EI regions will be higher than the rest of EI. This indicates that the electrometrical wave propagation speed will increase in those regions.

The distribution of wave propagation speed for each scenario is presented from Figure 4.5 to Figure 4.8. The interconnection average propagation speed is given in Figure 4.9. We can see that the average propagation speed increases from 500 miles per second in the base case to around 1,800 miles per second in the 80% renewable penetration scenario. This result confirmed that the wave propagation speed would increase dramatically with the increase of PV

penetration. Furthermore, as shown in Figure 4.8, the regions with high PV penetrations tend to have higher propagation speeds, especially for the Southern and Northeastern EI regions. The increase in wave propagation speed indicates that it will take a much shorter time for a disturbance to spread across the entire interconnection. The high propagation speed also brings challenges in designing adaptive relays with electromechanical-wave-ride-through capabilities.

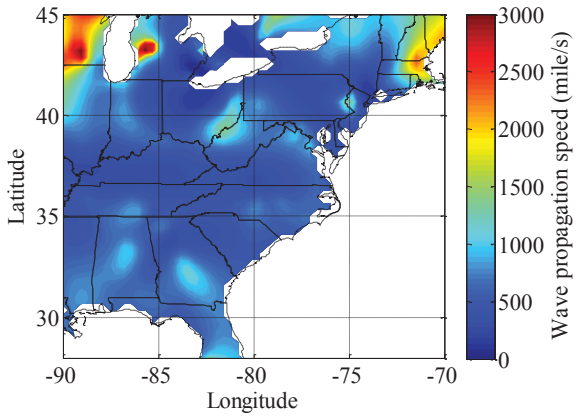

Figure 4.5. Electromechanical wave propagation speed distribution in the 5% PV penetration scenario

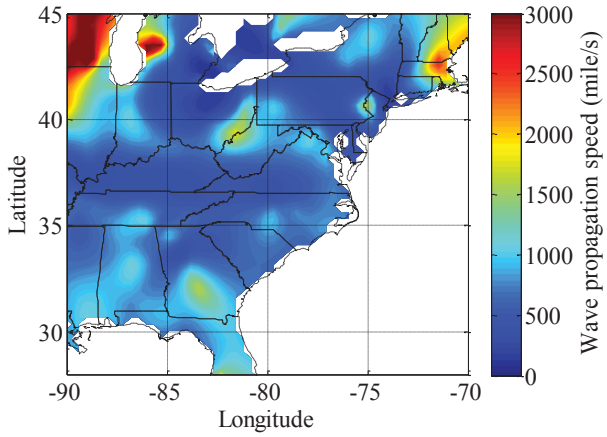

Figure 4.6. Electromechanical wave propagation speed distribution in the 25% PV penetration scenario

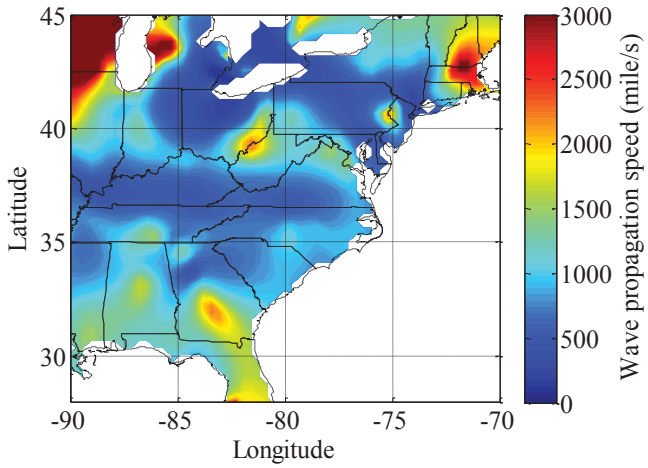

Figure 4.7. Electromechanical wave propagation speed distribution in the 45% PV penetration scenario

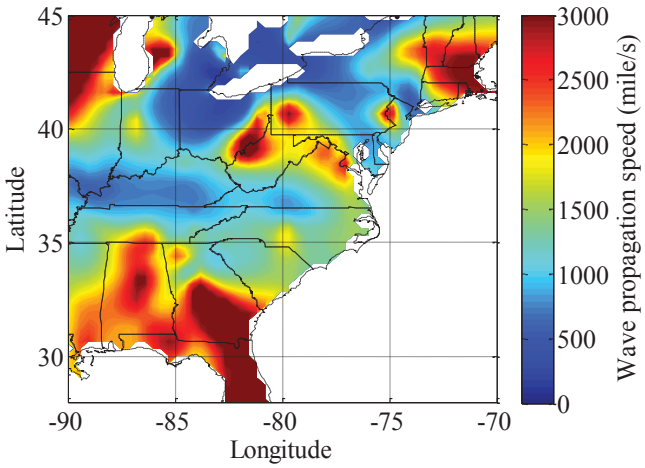

Figure 4.8. Electromechanical wave propagation speed distribution in the 65% PV penetration scenario

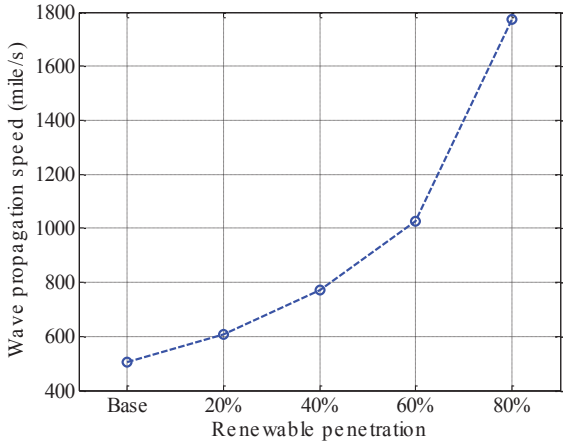

Figure 4.9. Interconnection-scale average electromechanical wave propagation speed in different PV penetration scenarios of EI

4.3.3. A Study on the electromechanical wave propagation speed, inertia, and PV penetration using a simple ring system

The objective of this study is to compare theoretical calculation and simulation result of the change of wave propagation speed with the change in inertia. A set of cases with a range of PV penetration rates was developed based on a ring system to check the applicability of the speed propagation formula (4.1) derived by Dr. Thorp in [124] to very low inertia systems.

$$|\vec{v}|^2 = \omega V^2 sin\theta/2|z|h \quad (4.1)$$

This equation indicates the square of the electromechanical wave propagation speed is proportional to the voltage per-unit value, system frequency per-unit value, while inversely proportional to the inertia and impedance for each segment of the model.

The test ring system is composed of 64 generators and 64 loads, as shown in Figure 4.10. Each generator's capacity is 150 MVA, providing 100 MW power to the grid through a step-up transformer, as shown in Figure 4.11. Each is branch is a 45-mile 230kV line.

Figure 4.12 shows simulated and the theoretical values of wave propagation speed at different inertia levels. The result shows that (4.1) [124] can accurately predict the wave propagation speed in this ring system when inertia reduces up to 93%. It also shows that when inertia is very low (98% inertia reduction), despite that the simulation result is expected to be consistent with (4.1), both simulation and actual system would be very fragile to operate at this condition.

Based on the ring system, a set of high PV penetration scenarios with different PV penetration rates was developed by replacing convention generators by PV at equidistant intervals, as shown in Figure 4.13.

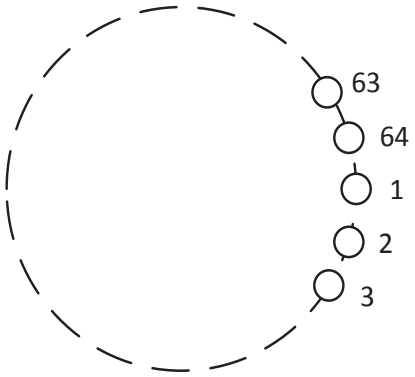

Figure 4.10. 64-generator ring system

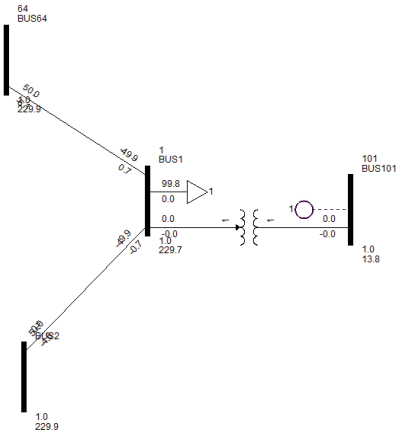

Figure 4.11. Composition of each unit in the ring system

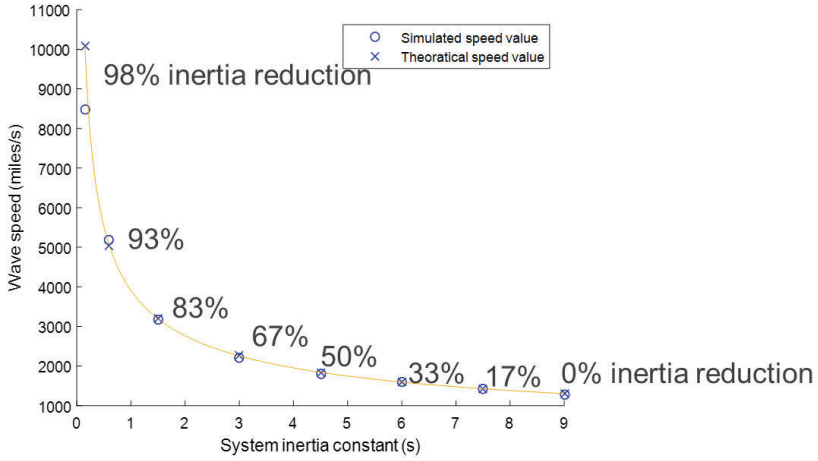

Figure 4.12. Relation between wave propagation speed and inertia reduction

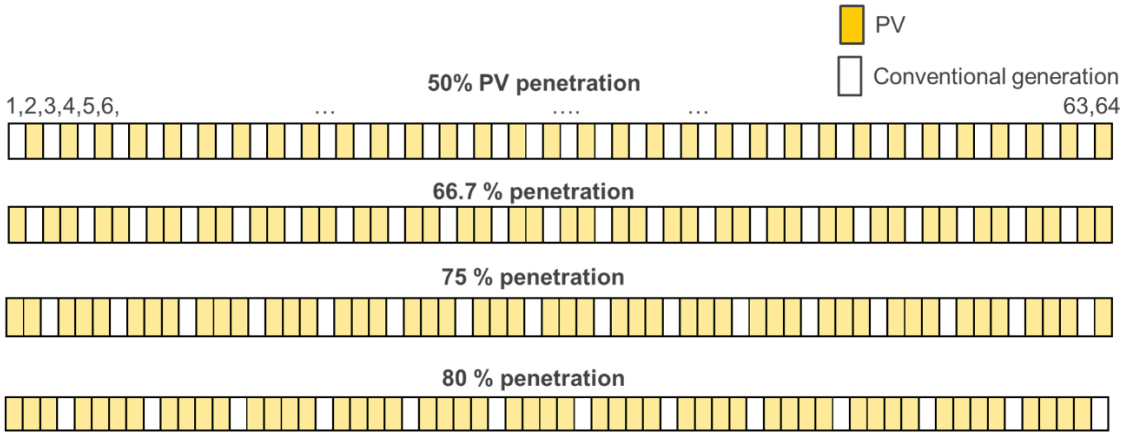

Figure 4.13. High PV penetration scenarios are developed by replacing convention generators by PV at equidistant intervals

Figure 4.14 shows the relation between wave propagation speed and PV penetration. The result shows that Equation (4.1) can still accurately predict the wave propagation speed in this high-PV ring system within the 50%-80% penetration range. The system has the non-convergence issue for >80% penetration scenarios. Systems with very-low inertia (up to 85-90% inertia reduction) will be very difficult to operate due to stability issues. Simulations can help identify potential issues due to low inertia. More work may be needed in applying (4.1) to quantitively predict the wave propagation speed in actual high-PV systems.

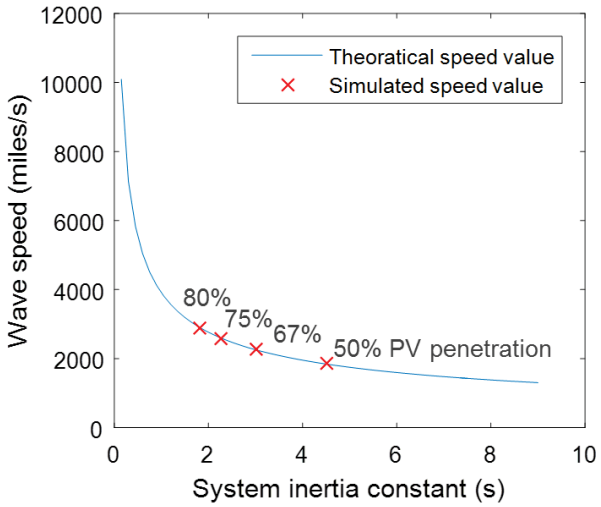

Figure 4.14. Relation between wave propagation speed and PV penetration

4.4. Conclusions

The FRCC-EI stability study results indicate that, with the increasing PV penetration level, FRCC becomes more vulnerable to the OOS instability issue. The reason is that FRCC's frequency regulation capability reduces with PV increases due to the reduction of synchronous units and relies more on the power imports from the two tie-lines, further stressing the stability of the tie-lines.

The results of the wave propagation speed showed an obvious non-linear correlation between PV penetration and wave propagation speed. Specifically, the propagation speed is roughly inversely proportional to the square root of system inertia for the same network topology and transmission parameters.

CHAPTER FIVE
FREQUENCY RESPONSE ENHANCEMENT BY CONVENTIONAL RESOURCES

The result in Chapter Two demonstrates that power grid frequency stability will be significantly impaired by the increase of PV penetration. Leveraging existing governor and load resources to provide additional power when generation after contingencies is an effective approach to improve the frequency response in high PV system. Based on the actual models of the U.S. Eastern Interconnection grid and Texas grid, this chapter investigates the capability of conventional resources in providing system frequency response. The quantitative impacts of various mitigation tactics are presented, including adjusting governor ratio, governor deadband, droop ratio, and fast load response.

5.1. Introduction

PV and wind penetration are increasing in many power grids [6, 49, 137]. The increase of PV penetration has an inevitable impact on the power grid frequency response, due to the de-commitment of synchronous units. PV is usually set to work at the Maximum Power Point Tracking (MPPT) mode so that it can hardly provide frequency response services, such as inertia and governor response [69, 121, 135, 138, 139]. Reserving headroom of PV, energy storage control, HVDC control for governor emulation and inertia emulation are research focuses to improve the frequency regulation capability of PV [140-142]. In reserving PV headroom for frequency response, a trade-off on the reserve capacity and the potential costs should be involved for economic considerations [65, 137, 141].

Despite the trend of reducing synchronous generation exists in many power grids, many synchronous units are still not likely to be retired or replaced in the foreseeable future. For example, hydro and nuclear units are competitive units in

terms of reliability and economics. Many power grids, such as the Unite States, are expanding flexible thermal units fueled by cheap and relatively clean energy, such as natural gas [49]. These units either have associated governors installed or has the potential to provide governor response. The frequency response capabilities of these units should be considered as potential frequency response resources to facilities high renewable penetration. In addition, fast responsive load can also be an important contributor of system frequency stability.

It is well accepted that the governor response capability can be enabled/disabled for most generators through local controller and the response parameters can be adjusted within a range, while the responsive load can be procured as necessary to support frequency stability [80, 143]. However, few studies have study the impact of these factors on system frequency stability in actual high-renewable large power grids. This study use the actual transmission network models of the U.S. Eastern Interconnection (EI) and the Electric Reliability Council of Texas (ERCOT) as the study cases. In this study, the impacts of the synchronous unit governor parameters, including governor deadbands, the governor ratio, the droop ratio on the system frequency response of the power grids are investigated. In addition, the effectiveness of fast load response on the system frequency response is also studied. A quantitative comparison on their impacts is provided.

The rest of this chapter is organized as follows. Section 5.2 presents the impact study of various factors on the EI frequency response under high PV penetration. Section 5.3 shows the impact of these factors on the ERCOT frequency response under high PV penetration. Section 5.4 provides a comparison and quantitative summary on these factors. Section 5.5 concludes the chapter.

5.2 EI system frequency response enhancement

The EI high-PV models with various PV penetration rates have been developed and used in various studies as documented in [69, 135, 144, 145]. The Base model without renewables has been validated using sychronphasor measurements from the FNET/GridEye system [146]. The EI system frequency response after a 4.5 GW generation loss (defined by the Critical Contingency Criteria of NERC [147]) under different PV penetration levels is shown in Figure 5.1. It shows that the frequency response deteriorates as PV penetration increases.

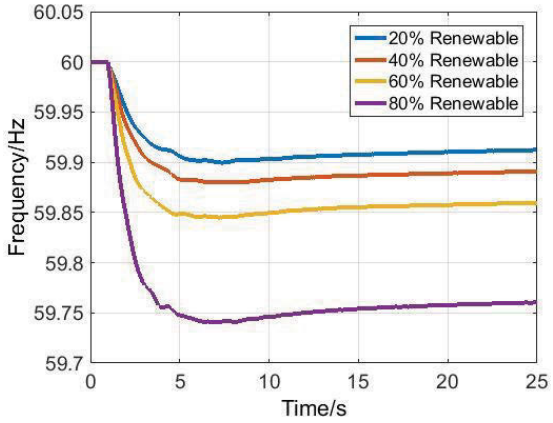

Figure 5.1. EI frequency response under different PV penetration level (4.5 GW generation loss)

5.2.1. Adjust governor droop

As a controllable parameter for synchronous generators, the governor droop[3] determines the steady-state amount of governor reaction to frequency deviation

[3] Droop is usually expressed as the percentage change in turbine/generator speed required for 100% governor action. For example, with 5% droop the full-load speed is 100% and the no-load speed is around 105%.

and thus decreasing governor droop is an option to improve frequency response. The governor droops of all EI synchronous generators were reduced from 5% to 3% (the lower boundary of WECC recommendation [148]) in Figure 5.2 to investigate this option's effectiveness. As shown by Figure 5.2, the 3% governor droop can dramatically improve frequency nadir and settling frequency. This result demonstrates that adjusting governor droop may be a cost-effective solution for frequency response improvement since it requires no additional governors. However, if the droop is set to be lower than 3%, it may lead to low frequency oscillations and other system instability issues [148].

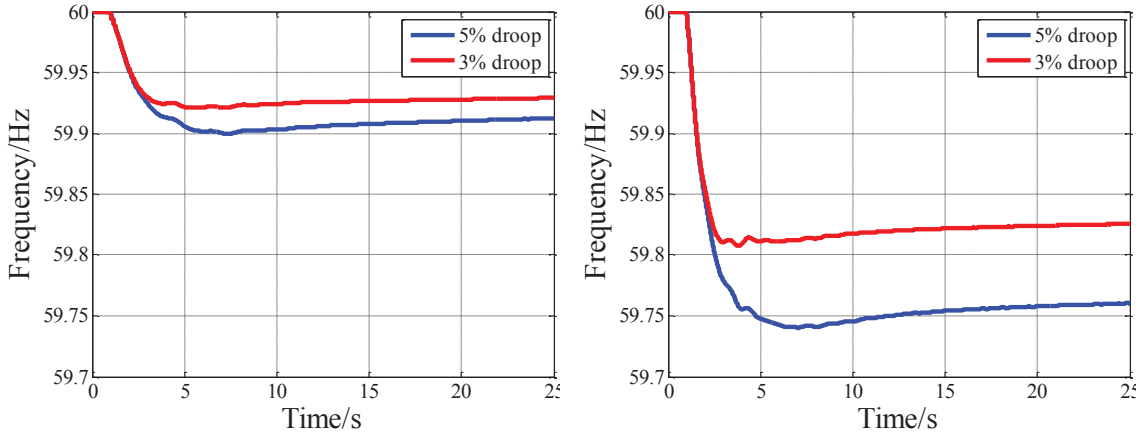

(a). 20% renewable (b). 80% renewable

Figure 5.2. EI frequency responses with different governor droop settings

5.2.2. Adjust governor deadband

Governor deadband is common in practice. It is utilized to prevent excessive governor actions caused by small and frequent load variations but it may also delay the governor responses to contingencies. Therefore, decreasing governor deadband could improve frequency response in high PV penetration scenarios. In this subsection, the average governor deadband in EI was narrowed down

from 36 mHz to 16.7 mHz (a NERC-recommended value for ERCOT [149]) to examine the effectiveness of decreased governor deadband in improving EI frequency response. Applying the largest resource contingency (4.5 GW generation loss), the simulation results with two different governor deadband settings are shown in Figure 5.3. Clearly, decreasing governor deadband improved the EI frequency nadir and settling frequency, but this magnitude of improvement is relatively limited for large contingencies. Therefore, decreasing governor deadband does not have much potential to improve EI frequency response in high PV penetration scenarios.

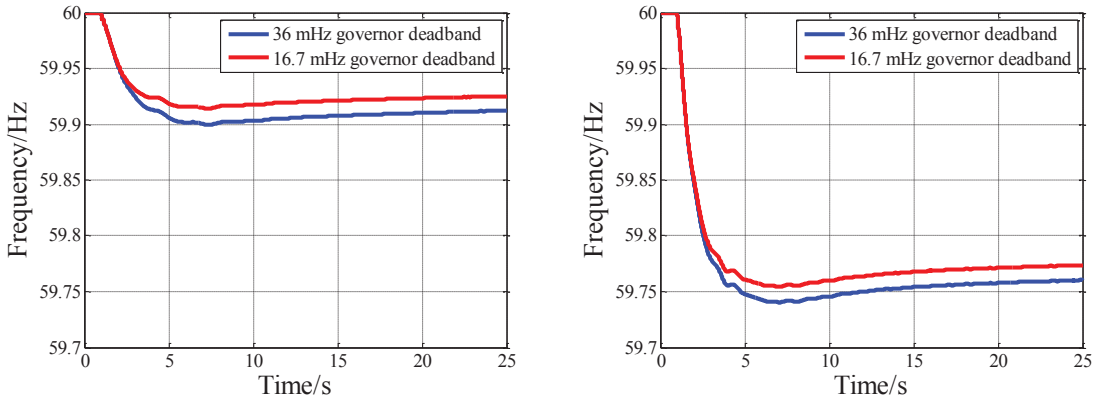

(a). 20% renewable (b). 80% renewable

Figure 5.3. EI frequency responses with different governor deadbands (20% renewable)

5.2.3. Adjust governor ratio

In the base model validation process, it had been found out that governor deadband and governor ratio were the two main factors contributing to the mismatch between simulated frequency response and actual frequency measurement [78]. Since merely putting in governor deadband was not able to tune the model to match the FNET/GridEye measurement, governor ratio in the

measurement-validated base model had been decreased to around 30% from 80% in the original model. This is also consistent with some utility companies' observation and the findings in some other studies [80]. That means, in order to prevent frequency response from declining, those "idle" governors are able to be put into service in the future. Therefore, in this subsection, governor ratio was adjusted and its impacts on the EI frequency response were studied for the largest contingency (the results of smaller contingencies will be similar). As shown in Figure 5.4, both frequency nadir and settling frequency were improved significantly due to a larger governor ratio. This is because more governors were contributing to the frequency support. In a word, if system operators want to enhance the EI system frequency response, increasing governor ratio will be an effective option. Additionally, in order to encourage more generators to participate in governor response, an ancillary service market may be established to compensate for those governor-responsive generators.

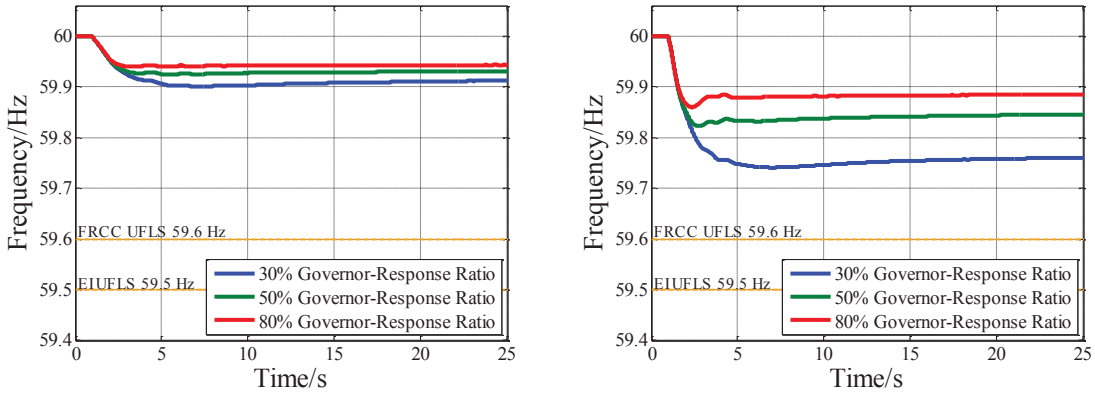

(a). 20% renewable (b). 80% renewable

Figure 5.4. EI frequency responses with different governor ratios

5.2.4. Summary of the EI system

The changes of EI frequency response metrics (including frequency nadir, settling frequency, and ROCOF) due to the abovementioned mitigation measures are calculated and documented in Table 5.1 (EI 20% renewable scenario) and Table 5.2 (EI 80% renewable scenario), respectively. It shows that the governor deadband decrease only improved the EI frequency nadir by 15 mHz in the 20% renewable scenario and by 14 mHz in the 80% renewable scenario. Comparatively, governor ratio increase and droop adjustment enabled much larger improvements in terms of both frequency nadir and setting frequency, especially in the 80% renewable scenario. It further indicates that governor ratio increase and droop adjustment are potential remedies for EI system operators to improve the EI frequency response in a high renewable penetration scenario. It is also worth mentioning that the EI system ROCOF values (measured at the first 0.5 second after the contingency) remain almost unchanged. This is because ROCOF values are mainly determined by system inertia (for a given generation loss event), which is hardly influenced by the abovementioned mitigation measures.

Table 5.1. Impact of mitigation tactics on EI frequency response metrics (20% renewable scenario)

		Benchmark	Governor Ratio Increase		Deadband Decreased to 16.7mHz	Droop Adjusted to 3%
			50%	80%		
Frequency nadir (Hz)	Value	59.900	59.925	59.940	59.915	59.921
	Change	N/A	+0.025	+0.04	+0.015	+0.021
Settling frequency (Hz)	Value	59.912	59.931	59.943	59.925	59.929
	Change	N/A	+0.019	+0.031	+0.013	+0.017
ROCOF (mHz/s)	Value	49	48	47	48	48
	Change	N/A	-1	-2	-1	-1

Table 5.2. Impact of mitigation tactics on EI frequency response metrics (80% renewable scenario)

		Benchmark	Governor Ratio Increase		Deadband Decreased to 16.7mHz	Droop Adjusted to 3%
			50%	80%		
Frequency nadir (Hz)	Value	59.741	59.823	59.860	59.755	59.808
	Change	N/A	+0.082	+0.119	+0.014	+0.067
Settling frequency (Hz)	Value	59.760	59.846	59.885	59.774	59.825
	Change	N/A	+0.086	+0.125	+0.014	+0.065
ROCOF (mHz/s)	Value	188	185	183	187	186
	Change	N/A	-3	-5	-1	-2

5.3. ERCOT frequency response enhancement

Similar to the EI, four different penetration levels of PV have been developed in ERCOT, as shown in Table 5.3. The ERCOT system frequency response for the largest N-2 contingency under various PV penetration levels are shown in Figure 5.5. It can be seen that if no mitigation tactics are applied, the ERCOT system frequency will cross the under-frequency load shedding threshold.

Table 5.3. Generation mix of high PV simulation scenarios in the ERCOT

Scenario	Instantaneous Penetration Level			
	PV	Wind	PV+Wind Total	Synchronous Generation
Interconnection Level Scenario 1	5%	15%	20%	80%
Interconnection Level Scenario 2	25%	15%	40%	60%
Interconnection Level Scenario 3	45%	15%	60%	40%
Interconnection Level Scenario 4	65%	15%	80%	20%

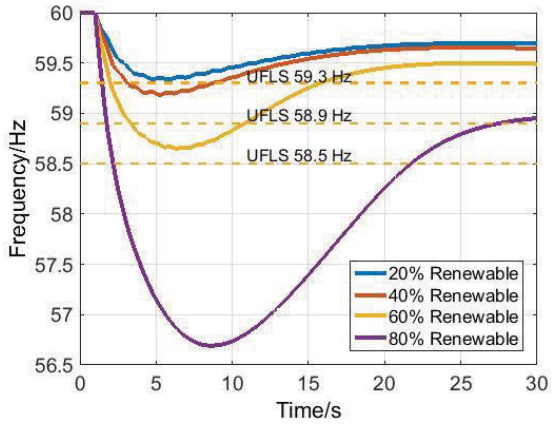

Figure 5.5. ERCOT frequency response under various PV penetration scenarios (2.7 GW generation loss, UFLS disabled)

5.3.1. Impact of high PV penetration on ERCOT UFLS

In fact, realizing its vulnerability to UFLS actions in high renewable penetration scenarios, ERCOT starts to utilize a fast frequency response (FFR) scheme provided by fast responsive loads (e.g. large industrial loads, heat pumps, industrial refrigerator loads, and storage devices) as part of its frequency response enhancement efforts [150]. Therefore, FFR and UFLS were simulated simultaneously in each high PV penetration scenario. Figure 5.6 shows the ERCOT frequency responses after the largest N-2 contingency (2.75 GW generation loss) with both FFR and UFLS. It can be seen that FFR was triggered in all scenarios (voluntary 1.4 GW load reduction at 59.7 Hz) but UFLS was triggered only in the 60% and 80% renewable penetration scenarios. For the 60% scenario, since the system frequency only marginally reached the UFLS threshold, only 0.8 GW load was dropped, as shown in Table 5.4. For the 80% scenario, dramatic frequency overshoot higher than 60 Hz were observed after UFLS actions, which may trigger over-frequency generator protection relays [151] and cause other stability issues. This overshoot was because UFLS relays

were tuned based on today's system characteristics. As a result, although only 1.35 GW (2.75 GW – 1.4 GW) load shedding was needed after FFR to fully compensate the frequency decline, a total of 3.5 GW load was dropped by UFLS. These results indicate that ERCOT may need to modify its FFR and UFLS schemes in order to accommodate 80% renewables.

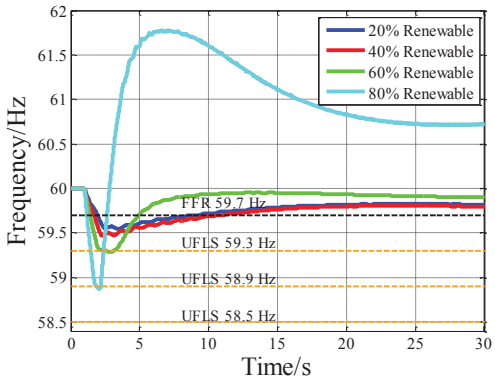

Figure 5.6. ERCOT frequency after enabling FFR and UFLS (2.75 GW generation loss)

Table 5.4. FFR and UFLS amounts in each ERCOT high PV scenario

Renewable	Event magnitude	FFR Amount	UFLS Amount/Percentage
20%	2.75 GW	1.4 GW	0
40%		1.4 GW	0
60%		1.4 GW	0.8 GW/1.14%
80%		1.4 GW	3.5 GW/5% (Stage 1)

5.3.2. Adjust governor droop

ERCOT requires all available governors are in service, its governor ratio cannot be further increased unless more governor-controlled synchronous generators are connected online. Moreover, as required by NERC, governor deadband had already been reduced to 16.7 mHz across ERCOT in 2014 [149]. Therefore, from

the generation side, only governor droop was adjusted to improve the ERCOT frequency response.

As shown in Figure 5.7 and Figure 5.8, reducing the governor droop from 5% to 3% will increase ERCOT frequency nadir and settling frequency dramatically for the 20% scenario. But for the 80% scenario, since the number of governors left was very limited, the droop adjustment was not able to improve the ERCOT frequency response obviously.

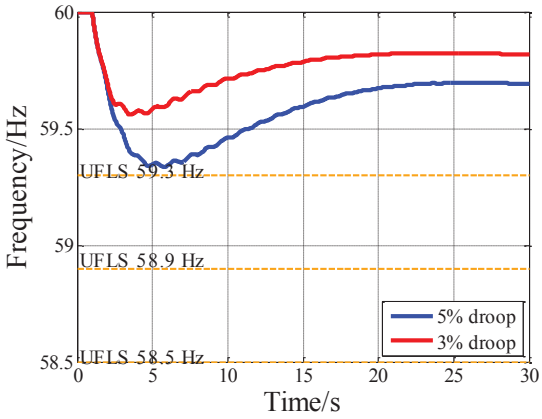

Figure 5.7. ERCOT frequency responses with different governor droops (20% renewable)

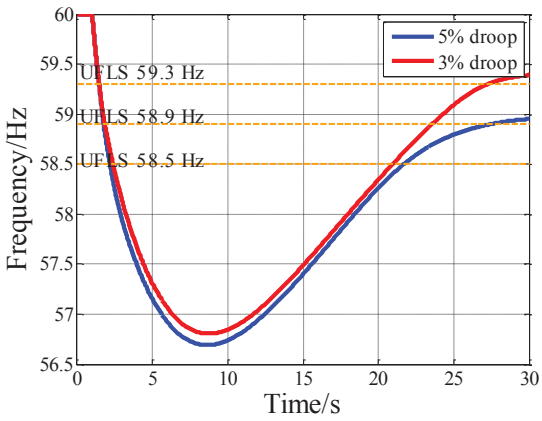

Figure 5.8. ERCOT frequency responses with different governor droops (80% renewable)

5.3.3. Use fast load response

Since droop adjustment is effective under high PV penetration due to the limited number of governors in operation, it is understandable for ERCOT to leverage Fast Frequency Response (FFR) to address the declining frequency response issue. Figure 5.10 shows the ERCOT frequency response improvement after tripping 1.4 GW FFR resources at 59.7 Hz, which demonstrates that frequency nadir and settling frequency increased significantly. These results indicate that FFR can be extremely valuable when the governor response provided by conventional synchronous generators is insufficient.

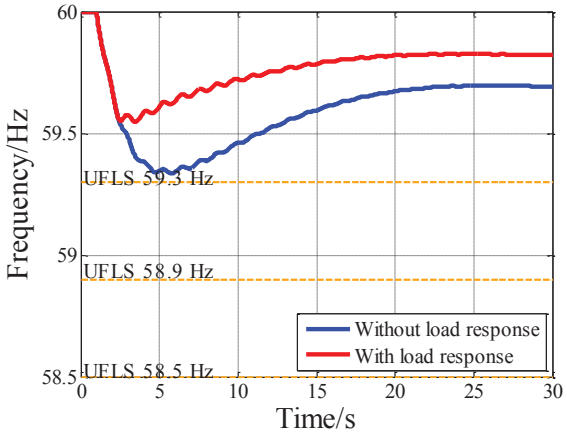

Figure 5.9. ERCOT frequency responses with fast load response (20% renewable)

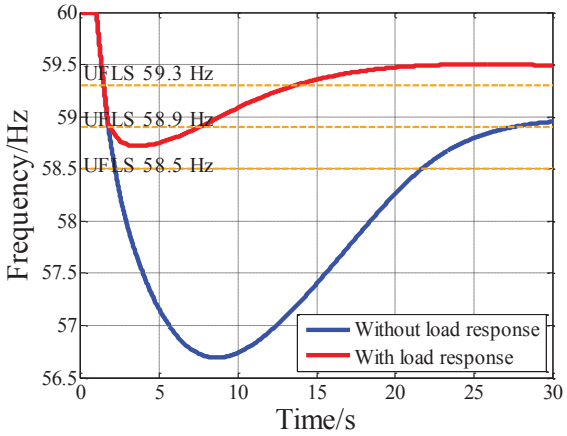

Figure 5.10. ERCOT frequency responses with fast load response (80% renewable)

5.3.4. Summary of the ERCOT system

The changes of ERCOT frequency response metrics due to governor droop adjustment and FFR are presented Table 5.5. As previously mentioned, since the number of governors is extremely limited in the ERCOT 80% renewable scenario, governor droop adjustment cannot significantly increase ERCOT's frequency nadir anymore, although it had been very effective in the 20% renewable scenario. Moreover, these two tables further demonstrate that FFR is the most effective method to arrest system frequency decline and it works regardless of the PV penetration level. Therefore, it can be anticipated that more responsive loads in power systems will participate in FFR as ERCOT renewable penetration continues to increase.

Table 5.5. Impact of mitigation tactics on ERCOT frequency response metrics (20%&80% renewable scenario)

		20% Renewable Scenario			**80% Renewable Scenario**		
		Benchmark	**Droop Adjusted to 3%**	**1.4 GW Fast Load Response at 59.7Hz**	**Base Case**	**Droop Adjusted to 3%**	**1.4 GW Fast Load Response at 59.7Hz**
Frequency nadir (Hz)	Value	59.34	59.52	59.55	56.69	56.78	58.72
	Change	N/A	+0.18	+0.21	N/A	+0.09	+2.03
Settling frequency (Hz)	Value	59.69	59.79	59.82	58.95	59.3	59.5
	Change	N/A	+0.10	+0.13	N/A	+0.35	+0.55
ROCOF (mHz/s)	Value	371	366	371	1,516	1,480	1,516
	Change	N/A	-5	0	N/A	-36	0

5.4. Conclusion

This chapter studied the influence of synchronous generation governor and fast load response on the system frequency stability. The result shown that the governor ratio (the percentage of generation providing governor response) has an obvious impact on the system frequency response. Reducing the governor droop can also make system frequency response stiffer. In addition, if load response can be activated fast, the decline of frequency can be promptly arrested.

CHAPTER SIX
STUDY OF WIND AND PV GENERATION CONTROL FOR FREQUENCY CONTROL AND OSCILLATION DAMPING

6.1. Introduction

Low system inertia and weak governor response were identified as one impact from increased renewable generation [152-154]. System inertia and governor response are crucial capabilities of a power grid's frequency stability since they are closely related to its frequency dynamics. For instance, in the first several seconds after losing a large power plant, the grid frequency drops sharply. Besides the amount of power loss, the initial rate of change of frequency (ROCOF) is mainly determined by the inertial response of the online synchronous generators. Those generators release their kinetic energy stored in the rotating mass into the grid, reducing ROCOF and allowing governors to take over for later frequency recovery. Since the amount of kinetic energy and governor response are determined by generator/load inertia and governor settings, displacing conventional synchronous generators with wind and PV generators will undermine the ability to arrest frequency drops and potentially trigger load shedding.

In recognition of the low system inertia and governor response issue, many previous studies have tried developing active power control strategies for renewable power plants to emulate frequency response of synchronous generators by utilizing inertial and governor controls [155-169]. For wind power inertia control, most control strategies utilize the kinetic energy of wind turbines to inject more active power into power grids in seconds [155-160]. Its advantage is that wind generators can still work in the maximum power point tracking (MPPT) mode in normal operation conditions but since the kinetic energy in wind turbines

has to be restored after a few seconds, the later stage of grid frequency recovery may be delayed. Another type of controls requires wind farms to reserve some power headroom for potential frequency control usage and, understandably, some wind power have to be curtailed in the normal operation conditions [170, 171].

Despite many conceptual designs of active power control, very few studies have ever tested the proposed controls on large interconnected power grid with high renewable penetration using measurement-validated grid models and realistic renewable distribution information [162, 172]. That is partially the reason why system operators have been slow in publishing grid codes for renewable power farms to provide frequency response to large, sudden power losses. Since the renewable generation frequency control may be required in the near future as renewable power plants keep increasing, it is extremely beneficial to implement and test those controls on detailed and accurate large power system models [163]. In light of this, this chapter uses two of the interconnections in the U.S., namely Eastern Interconnection (EI) and Texas Interconnection (TI or ERCOT), for case studies, which provides a valuable reference for formulating appropriate grid codes for frequency control of renewable plants. Optimized wind and damping are proposed and tested on the two interconnections in this study. Parameter determination for these controls is also discussed. PV distributions instead of uniformly distributed renewables are used in this study. Control strategies of PV and wind power plants for both frequency response and oscillation.

The reminder of this chapter is organized as follows: in Section 6.2, the advanced renewable generation controls are implemented and tested on EI and TI models, and Section 6.3 concludes the chapter.

6.2. Renewable generation active power control

In this section, the renewable generation active power control will be implemented in EI and TI systems to mitigate the negative impacts of renewable generation on frequency response and help damp oscillations. Details of the schemes of active power control for PV and wind are documented in [173]. The control diagrams of wind and PV active control are described in Appendix C.

6.2.1. Frequency response with renewable active power control

Inertia control and governor control are implemented in the EI and TI renewable power plants to demonstrate the effectiveness of these two controls on the EI and TI system frequency response improvement.

A typical generation trip event with 1 GW loss is applied to EI. The active power outputs of a wind farm in EI are shown in Figure 6.1 as an example and the same wind farm's wind turbine speed deviations are shown in Figure 6.2. The output of a PV plant is shown in Figure 6.3. The frequency responses of the EI system under different control scenarios are shown in Figure 6.4. From Figure 6.1, the wind farm inertia control enables a wind farm to increase its active power in response to the generation failure disturbance in the EI system by use of the kinetic energy stored in the wind turbines. However, this active power surge cannot last for more than several seconds and later the wind farm active power output goes through a "dip". That is because the kinetic energy stored in wind turbines must be "recharged" immediately so that the wind farm can go back to its original operation point. This process can be also observed obviously in Figure 6.2. With wind farm inertia control, the wind turbines decelerate to release the kinetic energy and then accelerates back to its original operation point due to the "recharge" process. PV power plants contribute system frequency response by reserving real power headroom, as shown in Figure 6.3. From Figure 6.4, it

can be seen that the wind farm inertia control helps decrease ROCOF (absolute value) but the frequency nadir is even lower than that of the base case. Therefore, inertia control alone is not enough to improve the EI system frequency response effectively and its merits lie in that it allows other controls (such as governor control of wind and PV) to have time to act.

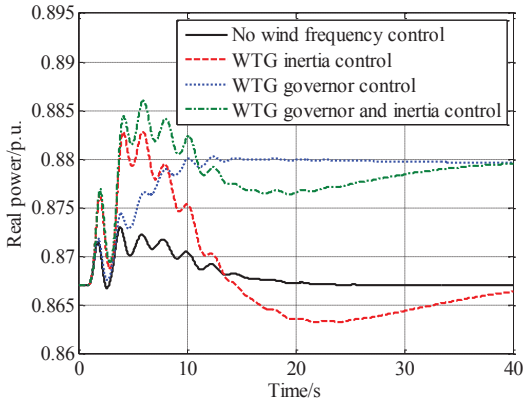

Figure 6.1. Active power output of a wind farm in EI

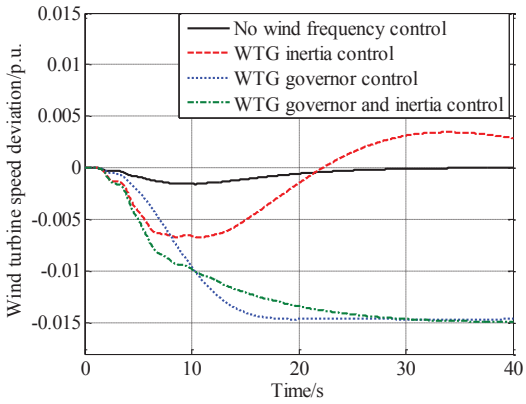

Figure 6.2. Wind turbine speed change of a wind farm in EI

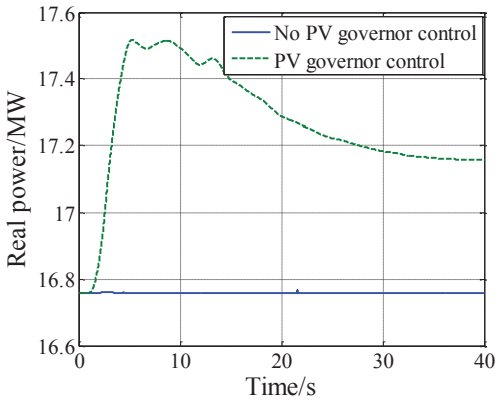

Figure 6.3. Active power output of a PV power plant in EI

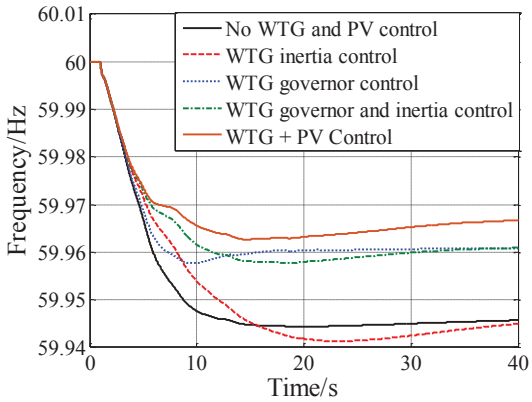

Figure 6.4. EI frequency response improvement with wind and PV controls

With wind farm governor control, since some power has been reserved by over-speeding, wind turbines decrease its speed to take utilization of the reserved power. Unlike inertia control, the increased power can last, as shown in Figure 6.1 and Figure 6.2. Figure 6.4 shows that the governor control reduces the nadir and settling frequency but not the ROCOF. This is under the assumption that enough wind and PV power has been reserved during normal conditions. Since inertia control can only reduce ROCOF and governor control can only decrease frequency nadir and settling frequency, a combination of inertia and governor controls can improve the EI system frequency response much more effectively. As shown in Figure 6.4, a combination of these controls can reduce both the ROCOF and frequency nadir. However, in order to bring the frequency back to its nominal value (60 Hz for U.S.), automatic generation control (AGC) must be involved.

Similarly, as shown in Figure 6.5, the inertia control mostly improves the TI system ROCOF and governor control reduces the frequency nadir and settling frequency. A combination of inertia and governor control can improve the TI frequency response in terms of multiple metrics. Comparing the control effects in the two systems, it can be seen that pure inertia control has relatively more obvious side effects in the EI compared with ERCOT in terms of reducing the frequency nadir. This is because the EI demonstrates the “L-shaped” frequency response, indicating inertia is not the bottleneck of the system frequency stability. If the EI only implements inertia control, the “recharging” of kinetic energy will reduce the frequency nadir significantly since the governor response of synchronous units have already reached their steady states. In contrast, this “recharging” does not significantly reduce ERCOT frequency nadir because the governors in ERCOT are still responding and the outputs of synchronous units are still increasing.

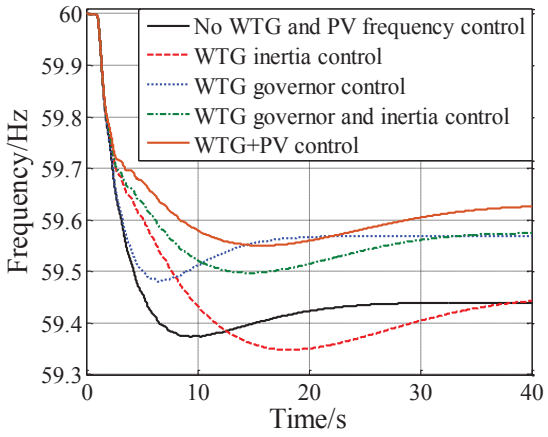

Figure 6.5. TI frequency response improvement with wind and PV controls

6.2.2. Parameter sensitivity study and tuning

It is worth noting that inertia control gain K_{wi} and governor control gain (K_{wg} and K_{pv}) are the most important parameters to the effectiveness of inertia and governor controls. As shown by Figure 6.6, a larger K_{wi} will decrease the ROCOF more effectively but make the frequency nadir even lower. There is also a risk that the wind turbines will stall if too much kinetic energy is used. Furthermore, as shown by Figure 6.7, a steeper governor droop (larger K_{wg} and K_{pv}) helps frequency nadir reduced further but that is under the assumption that more renewable output is reserved. Therefore, appropriate parameter setting is important for wind and PV active power controls, especially in a large power system with high amounts of renewables.

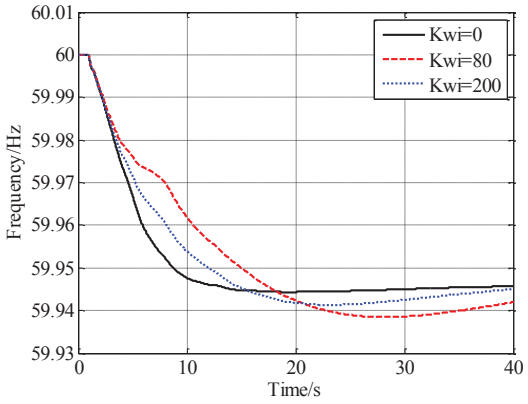

Figure 6.6. K_{wi} value change impact on frequency response

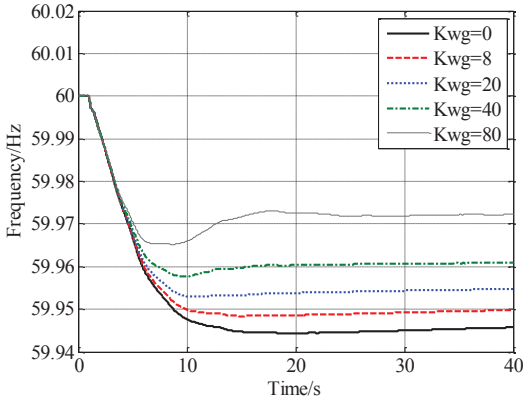

Figure 6.7. K_{wg} value change impact on frequency response

Considering the large number of renewable power plants in large power systems such as EI and TI and the constantly changing power grid conditions and wind and solar resources, a perfect parameter optimization solution will be difficult to obtain. Therefore, a straightforward and practical way to tune those parameters from a viewpoint of engineering is needed. To solve this issue, a statistical analysis of the EI generators' inertia and governor droop values is conducted and the results are given in Figure 6.8 and Figure 6.9.

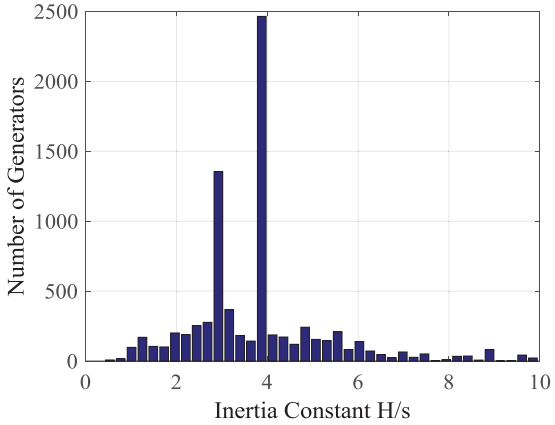

Figure 6.8. EI generator inertia value distribution

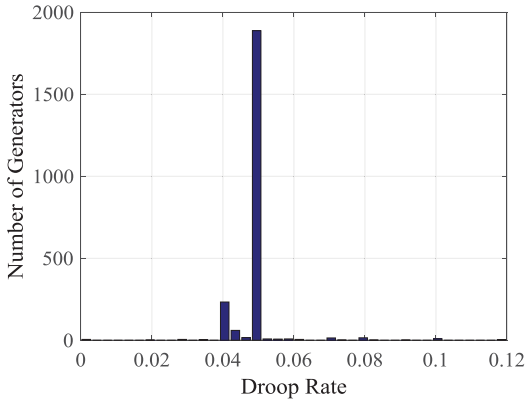

Figure 6.9. EI governor droop value (R) distribution

From Figure 6.8, the average generator inertia value is around 3.9s per 100 MW for EI generators. This average inertia value can be used as a guideline to determine the K_{wi} value of wind farm inertia controls in the EI system. For example, in order to make sure the overall system inertia is not decreased by installing a 300 MW wind farm, this wind farm's inertia control K_{wi} value can be tuned to provide a virtual inertia that is equivalent to 300 MW * 3.9s/100 MW= 11.7s. In this way, the overall system inertia can be maintained. In fact, since a variable-speed wind farm has more kinetic energy stored than a conventional synchronous generator of equivalent size, providing a virtual inertia equivalent to that of synchronous generator will not be an issue for wind farms. However, it should be noted that though the aggregated system inertia value is not decreased due to the wind farm inertia control, the system inertia geographic distribution will be changed since wind farms will be mostly located at wind-rich regions. This inertia redistribution will not significantly influence the system average frequency response but it is expected to have obvious impact on inter-area oscillations.

For the governor emulation control in renewable power plants, since the governor droop gain is usually chosen to be 20 (1/R=1/0.05) for most synchronous generators in the EI, the same value can be adopted for EI wind and PV power plants. Furthermore, the dead-band of these governor controls should be similar or even smaller than governor dead-band than synchronous generators (currently 36 mHz for generators larger than 400 MW in EI).

6.2.3. Electromechanical oscillation damping

Inertia and governor controls have been shown to be able to improve the EI and TI frequency response. This active power control capability can also be used to damp inter-area oscillations. According to the FNET/GridEye measurement,

many oscillations in the U.S. power grids were triggered by generation loss events. Therefore, it is necessary for wind and PV power plants to implement the frequency control and oscillation damping control simultaneously. Figure 6.10 shows the frequency of a 500 kV bus in EI after a generation loss event, which includes an obvious oscillation component. To increase the damping of this oscillation, oscillation control with typical parameters is installed at all the wind farms. With the simultaneous controls including governor, inertia, and oscillation damping controls, the frequency response has been improved and oscillations has been damped at the same time. This case study demonstrates the potential of renewable power plants to improve the power system's overall stability.

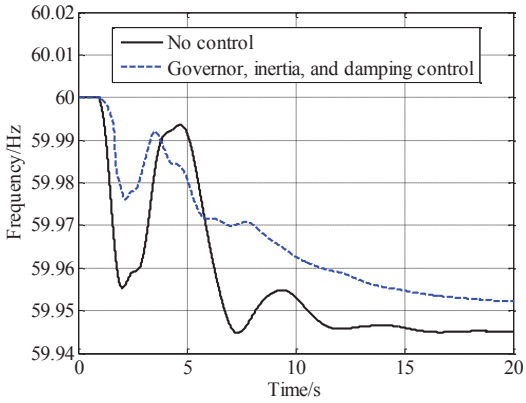

Figure 6.10. Frequency of a 500kV Bus in EI due to frequency control and oscillation damping

6 .3. Conclusion

In this chapter, renewable active power control in large power grids were studied based on measurement-validated system models and realistic renewable penetration information in two U.S. power systems. Simulation results demonstrated that active power control in renewable power plants is promising in improving the EI and TI systems' frequency response. Furthermore, a practical

approach of tuning the control parameters was discussed and the simultaneous control of frequency response and oscillation damping was tested.

CHAPTER SEVEN
ELECTROMECHANICAL WAVE PROPAGATION BASED EVENT LOCATION AND INERTIA DISTRIBUTION DETECTION IN HIGH PV POWER GRIDS

7.1 Introduction

Due to system uncertainty and complexity, modern power system operation increasingly relies on high-resolution real-time situation awareness systems [174]. Wide-area synchrophasor measurement systems (WAMS) can provide measurements with a much higher time resolution than conventional measurement systems. Therefore, WAMS are considered state-of-the-art technology for monitoring power grid dynamics [127, 175, 176]. The utility-level sensors in WAMS are called Phasor Measurement Units (PMUs). PMUs are expensive, installed in high voltage environments, and require complex installation and maintenance procedures, which hinder their deployment substantially. Also, PMU measurements are considered proprietary data, which makes exchanging data between utility companies difficult.

As a WAMS deployed at the distribution level, FNET/GridEye has been monitoring power grids using synchrophasor technology for more than 10 years [177]. Measured data include frequency, voltage phasor angles and magnitudes, and power quality. FNET/GridEye consists of two major parts: over 300 frequency disturbance recorders (FDRs)—the sensors installed on power grids worldwide—and the data center hosted at the University of Tennessee, Knoxville (UTK) and Oak Ridge National Laboratory (ORNL). Multiple applications have been developed on this quickly-deployable distribution-level synchrophasor measurement system [108, 112, 178-181]. Compared with WAMSs owned by

utilities, FNET/GridEye has many unique applications. One of such applications is disturbance location determination.

Power grids are subjected to various types of disturbances frequently, such as load variations, generator and line trip, and faults. Many disturbances are minor but large disturbances or events may lead to system emergency states. Automatic event detection and location can improve situational awareness and activate appropriate controls to prevent cascading failures [182]. Taking generation trip location as an example, detecting a generation trip event allows demand-side frequency response. Further, locating a generation trip allows each balancing authority to minimize frequency excursions and constrain the impact of the event through proper frequency control strategies, such as activating system reserve and leveraging responsive loads.

The type of event can be identified based on footprints in frequency or angle profiles. In the FNET/GridEye system, different types of events have unique characteristics on frequency measurements. For example, typical load shedding will cause a sharp increase in the frequency profile, while generator disconnection will result in a sharp frequency decrease. Line trip events will cause oscillations in frequency without changing the average frequency. A fault event will cause a relatively local frequency drop. These features can be used to detect different types of events, as investigated in [183, 184].

This chapter mainly focuses on the problem of event location. Existing disturbance location methods have two major steps: obtaining the FDR response time and estimating the location. The FDR response time can be obtained as the time frequency measurements pass a given threshold. For estimating disturbance location, the least-square disturbance location approach requires the

assumption that electromechanical wave propagation speed is established a priori and remains constant throughout the system [185]. Otherwise, the method will yield a series of suspected locations: one location for each propagation speed. However, in practice, there does not exist a uniform speed that is always valid across any given power grid. The propagation speed varies with system conditions, e.g., unit commitment and load dynamics [186, 187], making the application of the approach difficult. The method described in [188] combines power grid models and measurements to locate generator trips. However, this method heavily relies on the power grid model to calculate the propagation distance. This model dependency cannot be adequately satisfied when the model is not available or system topology changes due to operation conditions. Ref. [189] described a non-parametric approach. This approach determines the event location by partitioning the study area into two parts for each two measurements. The result of this approach may yield large or irregular areas as suspected disturbance locations. In summary, existing disturbance location approaches either rely on system models or are highly depend on specific parameters [190].

In addition, as the wind and solar photovoltaic (PV) outputs are variable, unit commitment becomes more uncertain and dynamic. However, the demand on inertia to support primary frequency response increases. Therefore, assessing the distribution of inertia has become a necessity but also a difficulty, especially in market environments. Conventional approach requires the information on event size, such as the tripped generator output. However, the event information is not usually available instantly by all the utilities and ISOs. In addition, understanding the distribution of inertia and which region is contributing how much inertia for primary frequency response is important track information for regulatory organizations such as U.S. NERC, which cannot be satisfied by a

single estimation result on system total inertia provided by the conventional method.

This chapter presents a robust and parameter-insensitive method to locate disturbances using FNET/GridEye [191]. To pinpoint the event location, this method combines Delaunay triangulation [192, 193] and bicubic 2D interpolation [194] by reconstructing the wave arrival time. In addition, under the framework of the proposed method, it is convenient to calculate the disturbance propagation speed distribution in the power grid, which is valuable when ensuring reliable protection actions under high renewable penetrations [49, 69]. Based on the propagation speed distribution, this chapter also presents a non-invasive approach to assess the system inertia using frequency transient measurements from distribution level PMUs. In estimating the inertia distribution, this approach makes use of the non-uniformity of the electromechanical wave propagation speed during generation trips or load shedding events, which happens multiple times daily for large power systems [112]. The proposed approach was validated by actual measurements from the FNET/GridEye system and the simulation results of the high renewable dynamic model representing the future U.S. Eastern Interconnection [195].

The rest of this chapter is organized as follows: Section 7.2 gives an overview on the FNET/GridEye system. Section 7.3 describes the new event location method and its implementation in FNET/GridEye. Section 7.4 describes the inertia change detection approach based on the electromechanical wave propagation. Conclusions are presented in Section 7.5.

7.2. Overview of FNET/GridEye

7.2.1. The frequency disturbance recorder

Distribution-level synchrophasor technology makes it possible to significantly decrease WAMS costs and simply deployment [196, 197]. Nevertheless, special technical challenges arise when designing hardware and software for synchrophasor measurement sensors in the distribution system [198-202]. For example, unlike transmission systems, distribution systems have much worse power quality due to the harmonics and distortions produced by various electric appliances. Under these circumstances, distribution-level sensors should be capable of capturing power grid dynamics at noisy system ends.

Embedded with a microprocessor for sampling and estimating frequency and voltage phasor, as well as other modules for GPS time synchronization and Ethernet communication, FDRs feature low manufacturing costs of about one tenth a typical transmission-level PMU [203, 204]. Additionally, FDRs' plug-and-play setup simplify installation procedures. FDRs do not sacrifice accuracy for their low cost and quick deployment [72]. In fact, FDRs have comparable or even higher accuracy than their counterparts [205]. So far, three generations of FDRs have been developed for improved measurement accuracy and data quality. Figure 7.1 shows the most widely deployed Generation-II FDR. Updates for the Generation-III FDR include enhanced functionalities on power quality measurements, and more importantly, accuracy improvement achieved by hardware and algorithm advancement. Its measurement accuracy reaches ±0.00006 Hz (for frequency) and ±0.003˚(for voltage angle) under steady state [206-209].

The deployment of FDRs in North America and FNET/GridEye coverage worldwide by 2015 are shown in Figure 7.2 and Figure 7.3, respectively. Real-time phasor measurements collected by FDRs at these locations are transmitted via Internet and collected at the data center hosted at UTK and ORNL. These measurements feed multiple applications including online monitoring, online analysis, and offline data mining, revealing valuable insights into power grid dynamic behaviors [146, 210].

Figure 7.1. Generation-II FDR

Figure 7.2. The FDR location map in North America

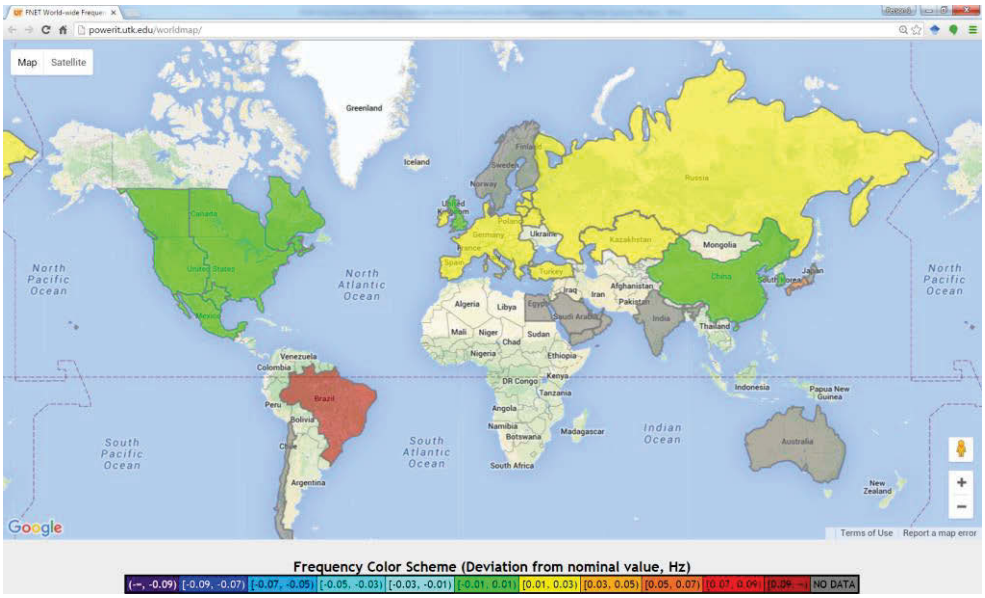

Figure 7.3. Worldwide FDR deployment and the frequency map

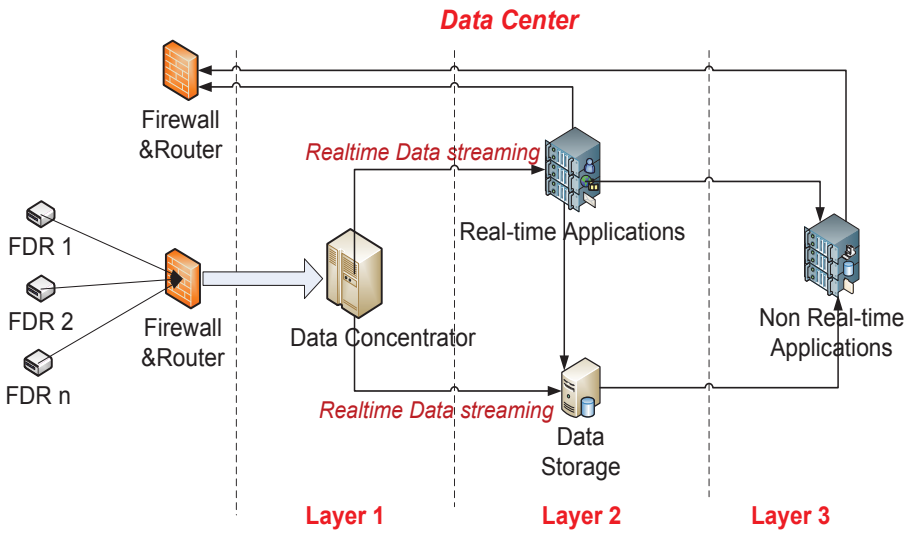

Figure 7.4. The FNET/GridEye data center structure

7.2.2. The FNET/GridEye data center

The FNET/GridEye data center can manage, processing, and safely archiving measurements systematically. It has a multi-layer structure, as shown in Figure 7.4 [72, 211, 212].

The first layer of the data center is the data concentrator, in which TCP/IP data packages are extracted, interpreted, error-checked, time-aligned, and then streamed into the subsequent layer. The second layer includes two agents: the real-time application agent and the data storage agent. Various modules are running on the real-time application agent to monitor power grid dynamic behaviors based on streaming data. For example, on this agent, the real-time event detection module monitors disturbances on the interconnection scale and sends out event alerts to system operators. Meanwhile, the data storage agent archives phasor measurement data streams and outputs from the real-time application agent for off-line applications. All data are archived in an efficient format to preserve data integrity while saving space. In the third layer, the non-real-time application agent runs offline applications to further exploit the archived data [213]. The archived data is a valuable information source for power grid research. For example, the dynamic models of U.S. power grids could be validated through comparing the actual system frequency responses (stored in the archived phasor measurements) with the model-based simulation results [214].

The multi-layer structure of the FNET/GridEye server facilitates efficient concentrating, processing, and archiving of wide-area measurements to successfully meet the timeliness requirements of various functionalities [207, 215, 216]. Based on the FNET/GridEye platform, a variety of visualization and analytics applications have been developed, and they are widely adopted by the

academia, the industry, and government agencies [111]. These applications enable system operators to keep better aware of the spatiotemporal evolvement of power grid dynamics rendered by various disturbances and changing environments.

7.3. Disturbance location determination based on electromechanical wave propagation

Since the interconnection-level power grid is large and the FDR distribution is coarse, FDR measurement in disturbance location is not available except for those cases in which disturbances happen in FDR-installed locations. A disturbance of the power grid results in speed changes of generator rotors, similar to the phenomenon of wave dissemination on a water's surface. The speed of generator rotors, which is directly proportional to frequency measurements, is a good indicator of the electromechanical wave impact. To determine the disturbance location, the proposed method uses frequency measurements of distribution-level FDRs sparsely distributed across a wide area. This method adopts Delaunay triangulation and bicubic 2D interpolation to locate disturbances in a more accurate way. The workflow of the proposed method includes the following steps. Figure 7.5 shows the structure of this workflow.

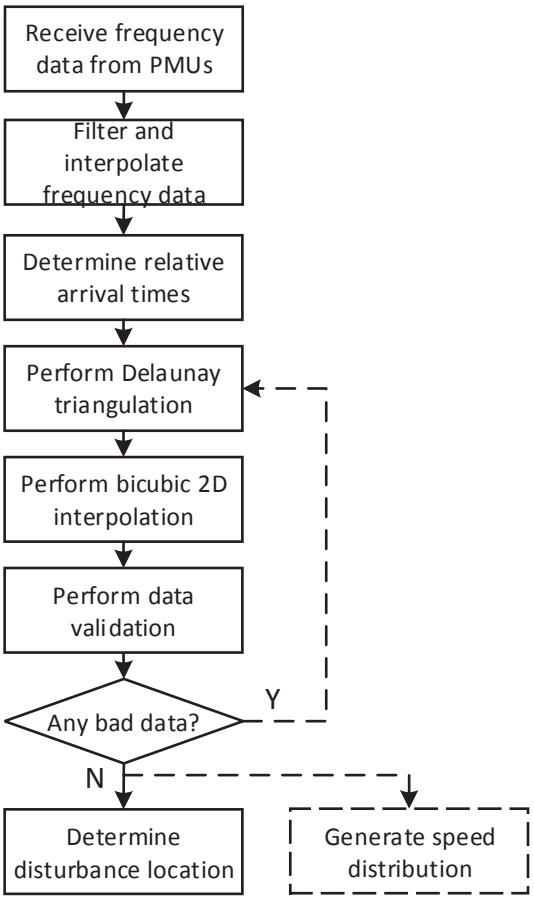

Figure 7.5. A flow chart of the disturbance location method

1) align frequency measurements based on GPS timestamps;
2) filter and interpolate frequency measurements to eliminate aliasing and reconstruct frequency profiles;
3) extract relative arrival times;
4) perform Delaunay triangulation from FDR GPS coordinates;
5) interpolate the response time in the spatial domain using bicubic 2D interpolation;
6) locate the disturbance by searching the minimum relative arrival time;
7) validate measurements to eliminate impact from bad data; and
8) calculate the propagation speed distribution.

7.3.1. Frequency measurement filtering, interpolation, and relative arrival time

FDRs measure the frequency at different locations during a power grid disturbance. A moving average filter removes the high frequency noise from frequency data during disturbance events. An equivalent form of the average filter for frequency measurement is defined as:

$$\bar{f} = \frac{1}{N}\sum_{i=1}^{N} f_i \quad (7.1)$$

where *N* is the size of the moving window. For the reporting rate of ten measurements per second in the current FNET/GridEye system, N is set to 5. After filtering, the frequency measurements are interpolated before obtaining the time delay of arrival for each FDR. The aim of implementing interpolation is to reconstruct the frequency during the periods between the reporting time snapshots, so that a better estimation of the arrival time can be obtained. In this chapter, linear interpolation is applied.

As an example, a generation trip disturbance happened at 13:48:05 (UTC) on Nov. 21st, 2014. During this event, 61 FDRs were streaming data at different

locations of the U.S. Eastern Interconnection (EI) power grid. The frequency dropped from 60.005 Hz to around 59.975 Hz through an “L” profile, which is a typical for frequency response given a generation trip disturbance. Figure 7.6 shows the filtered and interpolated frequency data of the detected disturbance event from multiple FDR units. The start time of the decrease of frequency relates to the distance of the FDR and the disturbance location. Those FDR units that are closer to the disturbance source have sharper and earlier decreases in frequency measurement. To calculate the relative arrival time, a threshold of frequency f_T is applied. Subroutines detect the disturbance and determine the threshold f_T and the common reference time t_R for a specific disturbance automatically.

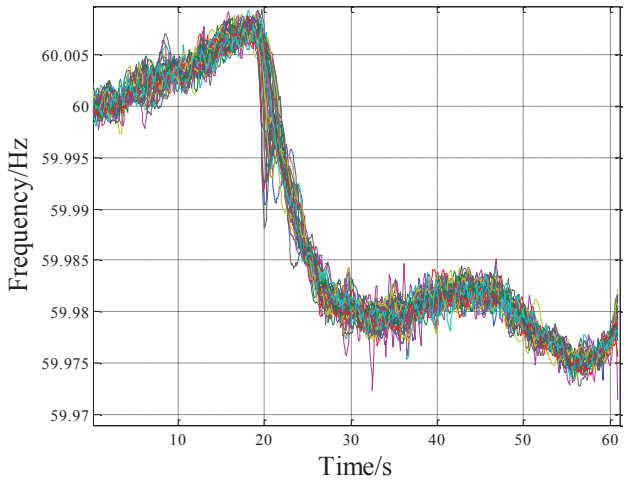

Figure 7.6. Filtered frequency (5-point median) of the detected disturbance

Determining the threshold value f_T involves four steps.

1) calculate the system average frequency;
2) calculate the ROCOF (rate of change of frequency) of the average frequency;

3) determine the event start time based on ROCOF; and
4) calculate the threshold where $f_T = \text{frequency at the event start time} - \Delta f$.

Δf is the frequency deviation threshold. This value can be easily determined by examining typical disturbances in a specific system. For the EI, this value is 0.005 Hz. In step 3, the event start time is determined by confirming that after a timestamp (the event start time), the majority ROCOF values (75% for the EI) during a consecutive period (4 second for the EI) are larger than a threshold ROCOF (1 mHz/s for the EI). A majority (75% for the EI) of ROCOF passing the threshold is enough to confirm the event occurrence because of the influence of oscillations stirred up by event disturbances. The relative arrival time is then defined as the difference between the common reference time t_R and the time of a FDR's frequency exceeding the threshold. For the case shown in Figure 7.6, f_T is calculated to be 60.0014 Hz and t_R is selected as18.8 s, respectively, as shown in Figure 7.7. It is worth noting that the purpose of introducing t_R is to set a common reference of the response time. It does not influence the event location result.

Table 7.1 lists the relative arrival time of some FDRs and Figure 7.8 graphically shows the relative arrival time of FDRs at different locations. Blue dots represent earlier response time whereas red ones represent relatively later responses. It shows that FDRs in four states: Kansas, Missouri, Arkansas, and Louisiana, had the smallest response time recorded (~0.7s). The New England area, which was remote from the disturbance, had the largest delay of response.

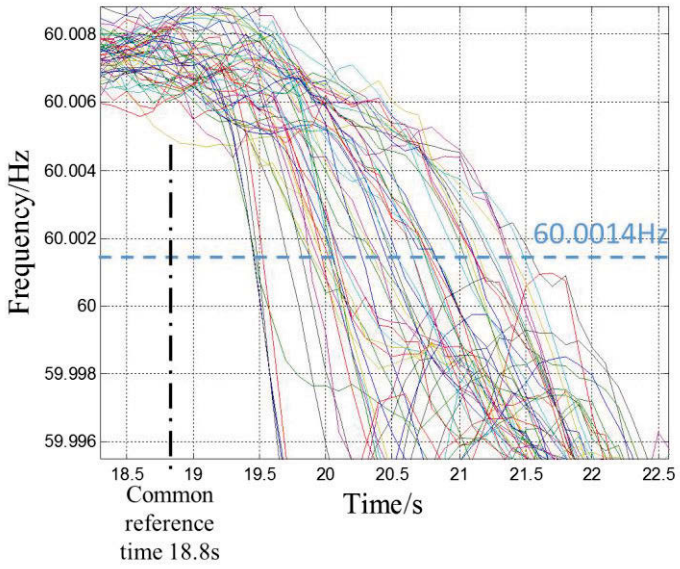

Figure 7.7. Relative arrival time calculation

Table 7.1. Relative arrival time of some FDRs

FDR #	FDR Location		Relative Arrival Time (s)
	State	Location (City or Company)	
844	KS	Dodge City	0.7870
941	KS	Wakeeney	0.7608
647	AR	Little Rock	0.7709
979	LA	Shreveport	0.8273
886	MO	Kansas City	0.7595
777	NE	LES	0.9996
756	MO	Franklin	1.1798
1027	MS	Jackson	1.1941
906	TX	Pleasant Hill	1.1252
792	VA	Hay Market	2.1406
1048	NY	Fredonia	2.2970

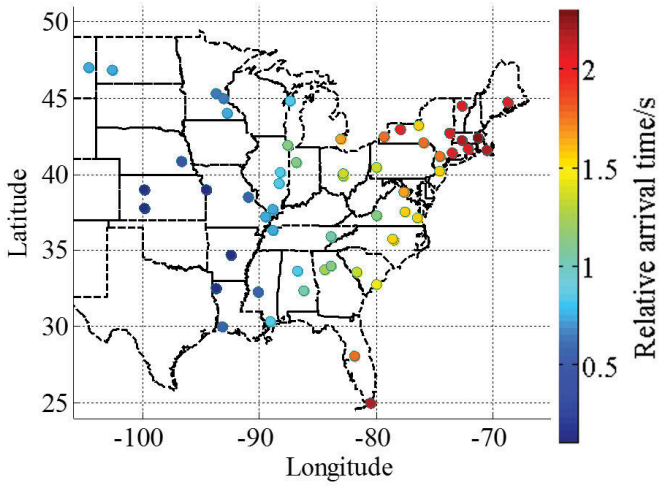

Figure 7.8. Relative arrival time of FDRs at different locations

7.3.2. Delaunay triangulation and bicubic 2D interpolation

Intuitively, the true disturbance location would be in an area that has the minimum relative arrival time. Since the propagation speed is unknown and may vary with power grid status, state-of-the-art methods that are highly parameter dependent cannot give a unique solution for the disturbance location or start time. In contrast, the proposed approach combines Delaunay triangulation and bicubic 2D interpolation to yield a parameter-insensitive method, robust against parameter errors. Delaunay triangulation partitions the area into triangles using existing FDR locations and a nearest neighbor approach, ensuring that no FDR is within the circumcircle of a triangle formed by three other FDRs. In this method, the indicator of whether FDR_i is within the triangle formed by the location of three other FDRs (FDR_A, FDR_B, FDR_C) is $M_{i-A,B,C}$ as shown in (7.2). This value should be positive for points lying inside the circumcircles when the FDRs at A, B, C are sorted counter-clockwise. As Delaunay triangulation in a 2D space is a frequently-performed routine, the Association for Computing Machinery (ACM) archives a standard algorithm (Algorithm 872) [217].

$$M_{i-A,B,C} = \begin{vmatrix} lon_A - lon_i & lat_A - lat_i & (lon_A^2 - lon_i^2) + (lat_A^2 - lat_i^2) \\ lon_B - lon_i & lat_B - lat_i & (lon_B^2 - lon_i^2) + (lat_B^2 - lat_i^2) \\ lon_C - lon_i & lat_C - lat_i & (lon_C^2 - lon_i^2) + (lat_C^2 - lat_i^2) \end{vmatrix} \quad (7.2)$$

Figure 7.9 shows the spatial Delaunay triangulation of FDR locations in the EI. Delaunay triangulation minimizes the maximum angle of all triangulations that connect each set of three FDR locations, allowing the reconstruction of the responses time at locations that have no FDR installed.

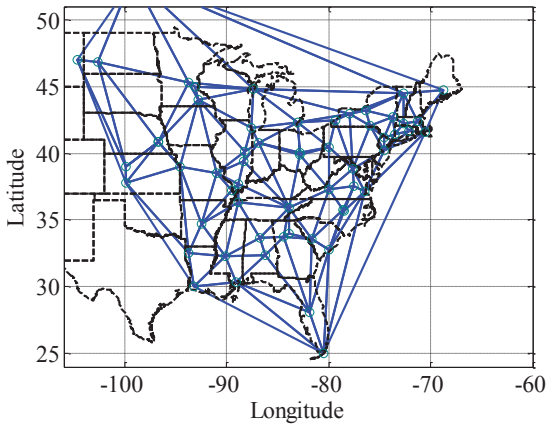

Figure 7.9. Delaunay triangulation of FDR locations in the U.S. Eastern Interconnection

After Delaunay triangulation, this method interpolates the FDR response time using bicubic 2D interpolation for each triangle. The interpolated arrival time for each triangle has the following form:

$$T(lon, lat) = \sum_{u=0}^{5} \left(\sum_{v=0}^{5-u} a_{u,v} lon^u lat^v \right) \quad (7.3)$$

where $a_{u,v}$ are the parameters of the polynomial calculated using the triangle-based surface fitting method described in [218], improved from its previous version in [219]. One implementation of this algorithm is ACM Algorithm 761 as documented in [220, 221].

Figure 7.10 shows the contour map of the bicubic 2D interpolation result. Bicubic 2D interpolation computes a two-dimension cubic function to fit the triangulated response time at the scattered points. The blue areas in Figure 7.10 show the locations with smaller response time, indicating locations near the disturbance, whereas the red areas represent significant latency in response due to wave propagation delay.

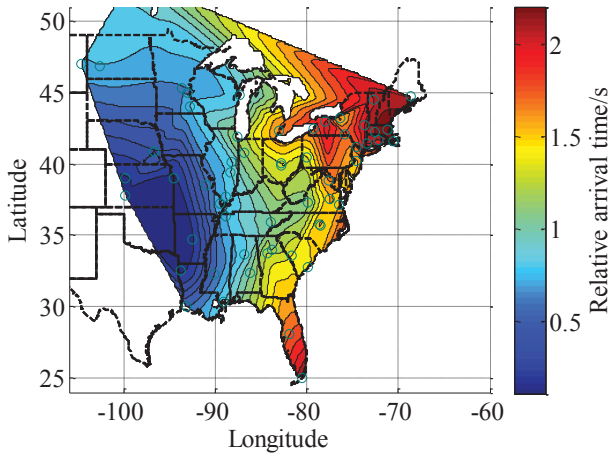

Figure 7.10**.** The contour map of time of ROCOF passing a threshold for all FDRs

7.3.3. Pinpointing event location and calculating the event start time

The method then scans the mesh grid to look for the point that has the global minimum response time, which is then designated as the estimated disturbance location, as shown in Figure 7.11. For this case, the computational time consumption to find the disturbance location is 0.461 seconds using a desktop with a 3.2 GHz CPU. Figure 7.12 shows a comparison of the actual and estimated disturbance locations. The red, blue, and white dots denote, respectively, the actual location, the estimated location based on the proposed method, and the estimated location based on the method in [222]. The distance between the actual and estimated disturbance locations using the proposed

method is 15.8 miles, while the value is 100.5 miles using the method in [222]. This result illustrates the small error typical of the proposed method.

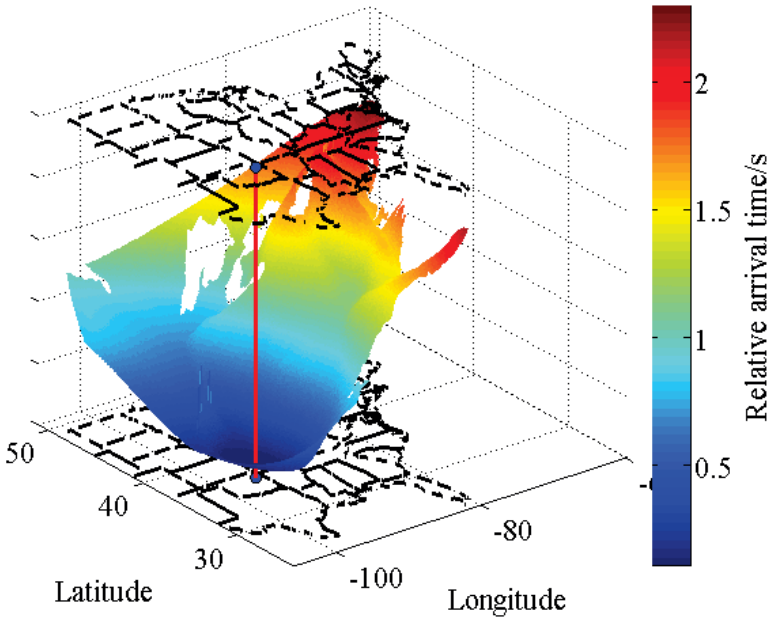

Figure 7.11. Pinpointing the event location on the contour map

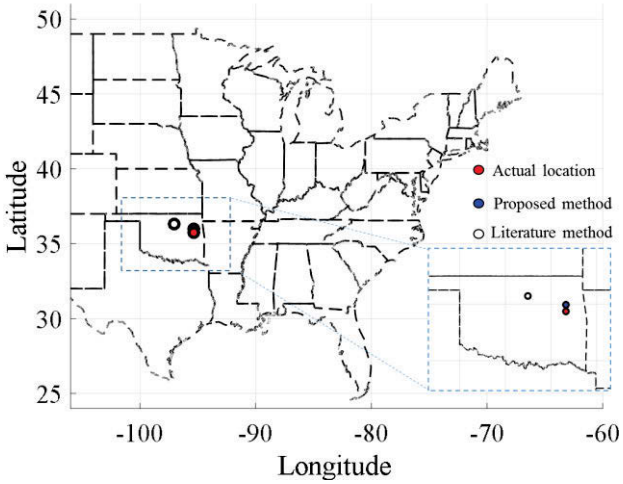

Figure 7.12. *Estimated and actual disturbance location*

Assuming the disturbance location estimation is denoted by $(lon_{event}, lat_{event})$ and the response time at this location is denoted by t_{min}, then the actual disturbance start time is estimated as $t_{event} = t_{min} + t_R$, where t_R is the common time reference for calculating the relative arrival time for all FDRs.

7.3.4. Data validation

FDR (or PMU) data may include bad data with erroneous timestamps due to GPS loss, clock error, or leap second issues. Therefore, after obtaining the estimated event location and start time, it is necessary to double check the credibility of the relative arrival time. This validation applies a linear regression method for data validation. The distance between the FDR location and the estimated event location is defined as

$$D_{(FDR_n,event)} = Distance\{(lon_{FDR_n}, lat_{FDR_n}), (lon_{event}, lat_{event})\} \quad (7.4)$$

The measured propagation time is calculated as

$$\Delta t_{(FDR_n,event)} = t_{FDR_n} - t_{event} \quad (7.5)$$

Then the distance and the measured propagation time for each FDR: $\{D_{(FDR_n,event)}, \Delta t_{(FDR_n,event)}\}|_{n=1,2,..n}$ are checked using linear regression, assuming propagation speed is constant, which means the propagation response time delay is proportional to the distance between the FDR location and estimated event location. A threshold is used to find the outliers of the measurements:

$$\left|\Delta t_{(FDR_n,event)} - \Delta t'_{(FDR_n,event)}\right| > \delta_t \quad (7.6)$$

where $\Delta t'_{(FDR_n,event)}$ is the propagation time from the estimated event location to FDR *n* obtained from linear regression; δ_t is the tolerance of the deviation between the measurement and the linear regression result. As a typical practice in identifying outliers in linear regression, δ_t is selected as 1.5 times of the interquartile range of near $\Delta t'_{(FDR_n,event)}$. If any FDR is found to be an outlier, then this problematic FDR will be reported to the operator and its data will be

deleted before recalculating the event location using Delaunay triangulation and interpolation. An example of the measurement with a time stamp issue is shown in Figure 7.13. The Michigan State unit has a measurement with an incorrect timestamp, as marked by the black arrow.

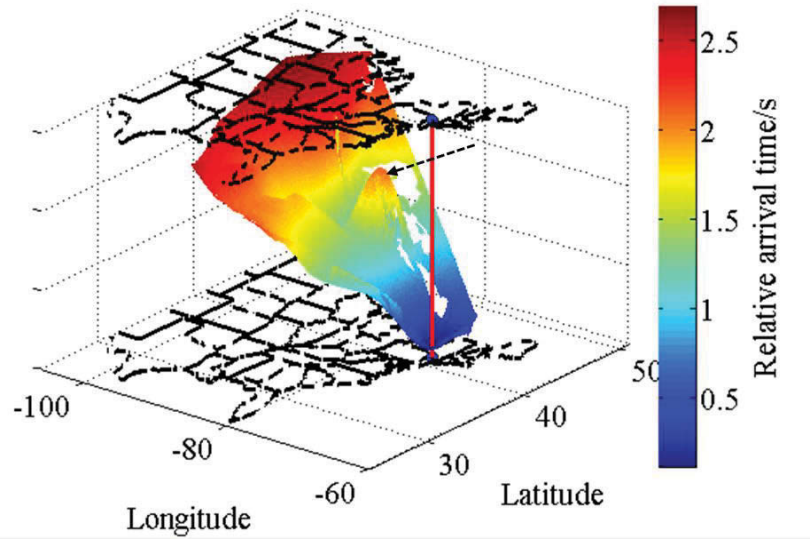

Figure 7.13. Detecting measurement with time stamp issues in Michigan

To test the robustness of the proposed method, eight events from August, 2013 to June, 2015 were tested using the proposed algorithm. The actual and estimated event locations are shown in Figure 7.14. The average distance between the estimated location and actual event location is 19.3 miles with a standard deviation of 9.8 miles. Because the maximum angle in the triangle constructed on grid edges must be large due to the lack of FDRs on one side, the surface fitting result has relatively large errors. Therefore, relatively larger errors are often seen for cases in which the actual disturbance location is near the grid edge.

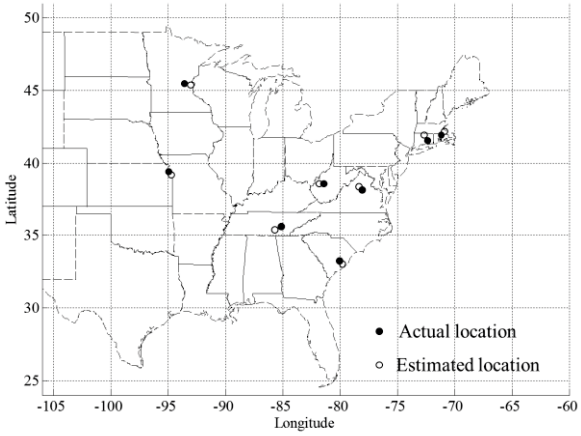

Figure 7.14**.** Actual and estimated event locations in the eight test cases

7.3.5. Application to a line trip disturbance using FNET/GridEye measurements

Since the proposed method is based on electromechanical wave propagation, its basic tenants can be applied to large load shedding, line trips, and faults, if the electromechanical wave propagation can be observed in measurements. An example of estimating line trip location is shown in Figure 7.15 and Figure 7.16. As line trip causes relatively local disturbances, only part of the EI is mapped in contour in Figure 7.15. The distance between the estimated location and the midpoint of the tripped line is 23 miles, as shown in Figure 7.16.

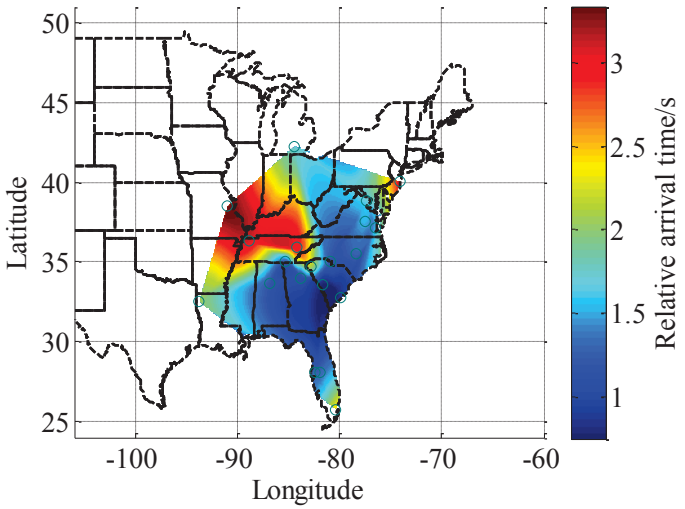

Figure 7.15. Relative arrival time distribution of a line trip disturbance

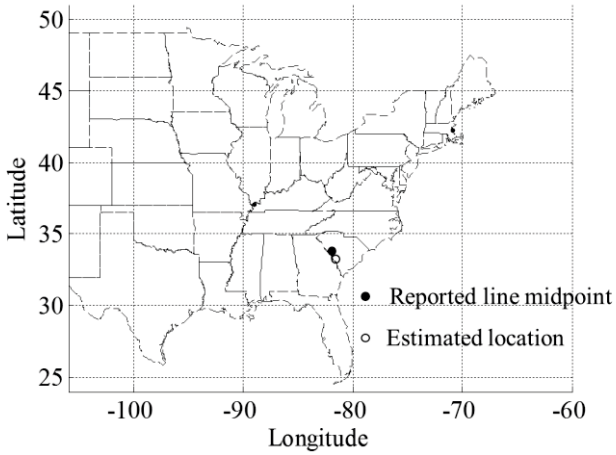

Figure 7.16. Line trip location estimation result

7.4. Non-invasive identification of inertia distribution change using FNET/GridEye measurements

The propagation of electromechanical wave is a transient process when the electrical angular frequency disturbance propagates from the event location to the rest of the system. The propagation speed is influenced by many factors, including the system topology, line parameters, voltage level, generator and load inertia.

Due to its complexity in nature, the continuum model is proposed to study the theory of electromechanical wave propagation [223]. In this ideal model considering all impact factors, the square of the electromechanical wave propagation speed is inversely proportional to the inertia distribution: $|\vec{v}|^2 = \omega V^2 sin\theta/2|z|h$, where ω is the electrical angular frequency (p.u.). V is the voltage magnitude (p.u.). θ is the line impedance angle ($\theta \approx \pi/2$ in transmission networks). $|z|$ is the line impedance (p.u.). v is the electromechanical wave propagation speed. This formula indicates that under high renewable penetration, the dominant impact factor of the propagation speed that varies on a daily basis is the generation and load inertia distribution. Without losing the generality, the relation between inertia distribution and the propagation speed is expressed as:$\vec{v} = f(h)$. f is a function, in which $|\vec{v}|$ decrease monotonically with the increase of h. Therefore, h can be expressed as

$$h = \bar{f}^{-1}(|\vec{v}|) \tag{7.7}$$

The electromechanical wave propagation speed $|\vec{v}|$ can be calculated based on the distribution level PMU measurement. The time delay of arrival (TDOA) of the frequency disturbance at one PMU differs from that at another PMU due to the difference in distance between the PMUs and the disturbance location. Thus the TDOA can be obtained by setting a threshold of frequency and recording the time

when the frequency crosses the threshold. The propagation speed of each point could be obtained from the local footprint of wave propagation:

$$|\vec{v}| = 1 \Big/ \left|\frac{d\overrightarrow{\mathrm{TDOA}}}{d\vec{s}}\right| \tag{7.8}$$

where $\vec{s}$ is the per unit distance along the direction of wave propagation. $d\overrightarrow{\mathrm{TDOA}}/d\vec{s}$ can be decomposed in to the longitude and the latitude direction as:

$$\frac{d\overrightarrow{\mathrm{TDOA}}}{d\vec{s}} = \left|\frac{\partial\overrightarrow{\mathrm{TDOA}}}{\partial\overrightarrow{c_{lon}}}\right| \vec{e}_{lon} + \left|\frac{\partial\overrightarrow{\mathrm{TDOA}}}{\partial\overrightarrow{c_{lat}}}\right| \vec{e}_{lat} = \left|\frac{\partial\overrightarrow{\mathrm{TDOA}}}{|\overrightarrow{c_{lon}}|\partial\vec{e}_{lon}}\right| \vec{e}_{lon} + \left|\frac{\partial\overrightarrow{\mathrm{TDOA}}}{|\overrightarrow{c_{lat}}|\partial\vec{e}_{lat}}\right| \vec{e}_{lat} \tag{7.9}$$

where $|\overrightarrow{c_{lon}}|$ and $|\overrightarrow{c_{lat}}|$ are the coefficients of per unit distance at this location for one degree of longitude and latitude, respectively. Their values can be obtained from the Haversine formula:

$$a_{lon} = 2 \cdot cos(\varphi_0) sin^2(\pi/360); \;\; a_{lat} = sin^2(\pi/360); \tag{7.10.a}$$

$$c_k = 2 \cdot atan2\left(\sqrt{a_k}, \sqrt{(1-a_k)}\right); \;\; k = lon, lat \tag{7.10.b}$$

$$|\overrightarrow{c_k}| = R \cdot c_k; \quad k = lon, lat \tag{7.10.c}$$

where φ_0 is the latitude of the location, R is the earth radius. Substitute to the equation above, one can obtain:

$$h = \bar{f}^{-1}\left(\sqrt{\left|\frac{1}{|\overrightarrow{c_{lon}}|}\left|\frac{\partial\overrightarrow{\mathrm{TDOA}}}{\partial\vec{e}_{lon}}\right|\right|^2 + \left|\frac{1}{|\overrightarrow{c_{lat}}|}\left|\frac{\partial\overrightarrow{\mathrm{TDOA}}}{\partial\vec{e}_{lat}}\right|\right|^2}\right) \tag{7.11}$$

$\left|\partial\overrightarrow{\mathrm{TDOA}}/\partial\vec{e}_{lon}\right|$ and $\left|\partial\overrightarrow{\mathrm{TDOA}}/\partial\vec{e}_{lat}\right|$ are the gradient of the TDOA in the longitude and latitude direction for per degree distance, respectively.

Applying the proposed approach, Figure 7.17 shows two estimated inertia distribution of the Eastern U.S. using FNET/GridEye measurements [112]. Both cases used generator trip events happened in Missouri U.S. The first case was in winter, while the other case was in an autumn. It can be seen that the winter case has slower propagation speed because of higher system inertia. This comparison shows the effectiveness of the proposed approach in identifying changes in inertia distribution using actual PMU measurements.

Figure 7.18 shows the application in identifying the system inertia change due to changes in renewable instantaneous output and unit commitment. Here, the 2030 Eastern Interconnection dynamic model is used. Figure 7.18 (a) shows the base case propagation speed distribution. Figure 7.18 (b) shows the propagation speed distribution when the renewable penetration in the New England ISO increased to 45% during a sunny day. It can be seen that the proposed approach can clearly identify the inertia decrease due to high renewable output in the New England area.

7.5. Conclusion

This chapter demonstrates a new disturbance location determination method implemented on a wide-area frequency monitoring network—FNET/GridEye. Without requiring a pre-determined propagation speed value, the proposed method can accurately pinpoint disturbance locations in the power grid. In addition, this method is robust to timestamp-shifting and measurement error. Based on this method, the real-time distribution of electromechanical wave propagation speed can also be calculated. The proposed method has the generality to be implemented in other WAMSs. In addition, this chapter presents a new approach to identify the system inertia change based on electromechanical wave propagation. Actual measurement and simulation data validates the effectiveness of the approach.

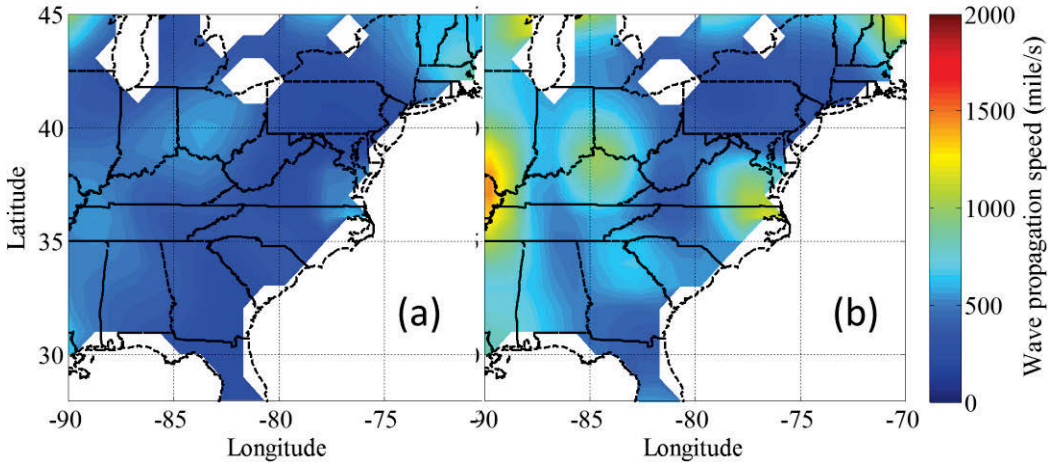

Figure 7.17. Seasonal change of wave propagation speed distribution based on FNET/GridEye measurements ((a) 2014 winter and (b) 2014 autumn)

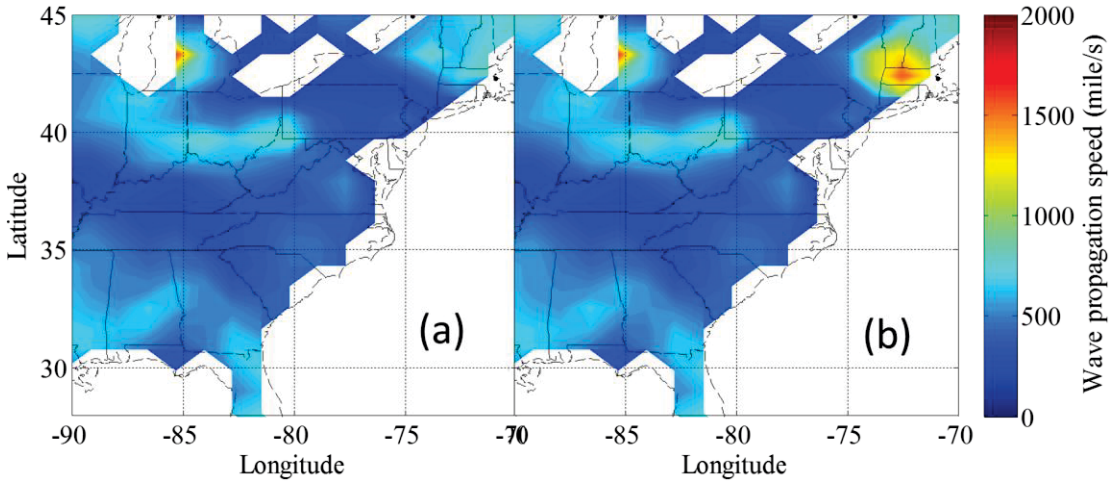

Figure 7.18. Change of wave propagation speed distribution when PV instantaneous output increased in NEISO (a) Base case; (b) PV output increases in NEISO

CHAPTER EIGHT
IDENTIFY CHALLENGES AND PROTOTYPE NEXT-GENERATION POWER GRID DATA ARCHITECTURE FOR HIGH RENEWABLE POWER GRIDS

8.1. Introduction

The goal of power systems is to achieve efficient, reliable, and sustainable supply of electricity. Due to the energy technology development, renewable generation expansion, and increasing concerns about environment, power systems face both challenges and opportunities. With the increase of load, wind, solar, electric vehicles, energy storage, and controllable devices, power system operation is more complex than ever [224]. In the meantime, information and communication technologies are also providing new opportunities for the power grid to transformed into a flexible system with two-way energy and information flow. This evolvement relies on collecting, processing, and utilizing data in a dedicatedly coordinated manner [225].

8.2. Summary of existing studies on power grid data architecture

A typical definition of data architecture is that “data architecture is a set of rules, policies, standards and models that govern and define the type of data collected and how it is used, stored, managed and integrated within an organization and its database systems.” As the essential part of making use of data, data architecture describes how data will be collected, transferred, stored, and used in information systems, serving as the backbone and determining the structure of every cyber-physical system.

Since sensors, communication, storage, controllers, actuators, and applications in power grids are constantly changing, it is desirable that the data architecture

has flexibility, interoperability, and scalability to provide support for emerging functions. Some identified challenges and requirements in for future power grid data architecture are listed in Table 8.1. To investigate latest efforts to bridge these gaps, this subsection reviews recent research on grid data architecture in the following aspects: data collection, data transmission, data service layer, data utilization (e.g., data analytics), as well as interoperability and cyber security. A summary of existing data architecture research is shown in Table 8.2 [226].

Table 8.1. Challenges in power grid data architecture

Challenges	**Explanations**
Data volume	Increasing number of measurement apparatus and systems in the generation, transmission, and distribution levels.
Diversity and heterogeneity	Various formats of data from different devices, as well as external data sources, such as weather, economy, and other energy systems (such as natural gas).
Data Quality	Latency, inaccuracy, and loss of data may significantly increase system risk and operation cost.
Processing and Computation	Large amounts of data may need to be analyzed for decision making within a very short time, such as a close-loop control.

8.2.1. Data collection

Grid Edge: This project focuses on the technology, business, and policy in medium- and low-voltage power grids for the increasing growth of distributed energy, microgrids, and demand response from the customer's perspective [227]. Grid Edge emphasizes the collection and analytic functions of multiple data terminals, e.g., advanced metering infrastructure, especially the data behind meters. It proposes a taxonomy architecture consisting of five layers (the physical asset layer, the network and control layer, the grid-edge application

layer, the data analytics layer, and the market evolution layer) to help visualize the various layers and technologies in them.

iTESLA: The Innovative Tools for Electrical System Security within Large Areas (iTESLA) project aims to develop a powerful toolbox to support dynamic security assessment and decision making of the pan-European electricity transmission network considering uncertainties [228]. To collect and exchange data among different regions, the project defines a set of requirements on external data provided by the different transmission system operators and recommends associated formats to carry the information. This project provides three open source prototype tools to convert data formats.

8.2.2. Data transmission

GridStat: GridStat is a data middleware based on a publish-subscribe mechanism, which is designed to deliver real-time operational data of the electric power grid. There are two layers in GridStat middleware: the data transportation layer, and the management layer. The data transportation layer is comprised of routers, which support routing and multicast services. The management layer consists of quality of service (QoS) brokers, which perform resource allocation in the data layer to establish paths that meet the QoS requirements of each subscription request [229]. Recently, GridStat has been integrated into several pilot projects for demonstration and further testing. For instance, it was integrated in GridSim to perform a holistic real-time simulation of power system and communication system in 2011.

NASPInet: NASPInet, a project of NASPI (the North American SynchroPhasor Initiative), aims to provide an "industrial grade", secure, standardized, distributed, and scalable data communication infrastructure which supports synchrophasor

applications in North America. NASPInet is intended to facilitate the secure exchange of both real-time streaming data and historical data. It is expected to support both one-tone unicast and one-to-many publisher-subscriber based data sharing in an efficient manner [230]. NASPI carried out several projects on NASPInet to demonstrate interoperable IEC 61850 90-5 based phasor data exchange over a Wide Area Network (WAN), and IP multicast routing of phasor data across a WAN, etc.

OpenADR: Open Automated Demand Response (OpenADR) specifies a set of data models and services for data exchange among utilities, Independent System Operators (ISO) and customer appliances participating in automated demand response programs using a common language and an existing communication infrastructure such as the Internet. Two protocols: hypertext transfer protocol (HTTP) and extensible messaging and presence protocol (XMPP), are supported by OpenADR for different deployment scenarios [231]. Up to now, over 60 utilities and controls vendors have already announced or have deployed OpenADR-based systems.

8.2.3. Data service layer

GridOPTICS™: GridOPTICS™ or Grid Operation and Planning Technology Integrated Capabilities Suite is a software framework developed by the Pacific Northwest Nation Lab (PNNL) for power system operations and planning [232]. This effort envisions a flexible, scalable software architecture for integrating a range of data collection, analysis, simulation and visualization technologies. This framework would enable plug-and-play of various analysis, modeling and visualization software tools for fast and accurate control of the power grid. To bridge the data access for different control purposes, a scalable and thin layer of event processing that hides the complexity of data storage and management is

also provided. Recently, several demo applications have been developed based on GridOPTICS™, e.g., graphical contingency analysis, net interchange schedule, and event detection.

SAFE: The IBM Solution Architecture for Energy and Utilities Framework (SAFE) is a software platform to extract actionable information from all data sources and to facilitate faster solution deployment and integration [233]. SAFE helps utilities integrate processes and related information throughout a company. SAFE can extract actionable information from all data sources (e.g., facility infrastructure, assets, customers, and workers) to enable new software capabilities related to smart energy utility management. This framework ensures that solutions from IBM business partners can be integrated more easily by providing pre-certified compatibility validation.

SERA: The Microsoft Smart Energy Reference Architecture (SERA) provides a valuable reference to accelerate development and guide deployments for the smart energy ecosystem [234]. Its holistic architecture design facilitates data and business process integration. SERA is intended to address prevailing systems and issues in enough detail to be useful, but without so much detail as to be untenable. In addition, SERA can help identify potential products and solutions that enable this architectural vision.

INDE: The Accenture Intelligent Network Data Enterprise (INDE) provides a template architecture based on the best practices and accumulated experience. The standards-based reference architecture consists of several components: a sensor network architecture, a data acquisition, transportation, and storage framework, a data integration platform, a visualization platform, a cyber-security framework, and a grid data analytics catalog, etc. [226]. INDE can be considered

as an interlayer software between raw grid data and high-level applications to manage massive real-time data and to transform them into useful, actionable information.

8.2.4. Data utilization

In the iTESLA project, the data mining methods applicable to the platform have been defined and described, which mainly fall into three modules: basic statistical, machine learning, and density estimation and sampling [228]. The identified methods have been applied to different examples using real data samples. For instance, a system prototype based on IEEE RTS has been established using these methods and the historical data from Marseille and Nancy. Methodologies for performing data mining has been outlined and applied to sampling, topology prediction, and the identification of positive and negative rules.

8.2.5. Interoperability

NIST framework: The National Institute of Standards and Technology (NIST) proposes a conceptual architecture of smart grid including seven domains (generation, transmission, distribution, customers, markets, operations, and service providers) and describes the data flow and energy flow among these domains to show they are interrelated [235]. The NIST model has been widely recognized since it is a valuable reference for research and industries to identify white-space standards that are highly desired to realize interoperable smart grid.

IEEE P2030: Based on the conceptual architecture proposed by NIST, the IEEE P2030 standard provides a smart grid interoperability reference model (SGIRM), which analyzes the interoperability of smart grids from three perspectives: power system, communication technology, and information technology [236]. Under this framework, IEEE P2030 provides interoperability guidelines to integrate the

information and communication technology into the energy systems. These guidelines will support the data management and information exchange for various applications in smart grids.

IEC communication architecture: This seamless communication architecture is proposed by IEC TC 57 based on several core standards (IEC 61850, IEC 61970, and IEC 61968), which focuses on the communication requirements of applications in power systems [237]. This architecture contains power utility communication standards including semantic data models, services and protocols. Furthermore, IEC has developed the smart grid standards map giving the relationship between the smart grid elements and over 100 related IEC standards. It can help researchers and stakeholders easily and instantly identify standards required for smart grid implementation.

Smart Grid Reference Architecture (SGRA): European standard development organizations extend the NIST conceptual model by adding two important elements: distributed energy resource (DER) and flexibility. The DER model allows addressing the role of DER in European objectives, while the flexibility concept can group consumption, production and storage together in a flexible entity (still under study) [238]. The extended European conceptual model indicates that interoperability should be implemented in different layers (Business, Function, Information, Communication and Component), hierarchical levels of power system management, and the complete electrical energy conversion chain.

GridWise® Alliance: GridWise® Alliance proposes an interoperability context-setting framework to provide a context for identifying interoperability issues [239]. Eight interoperability categories related to systems integration and interoperation

in the electric industry are identified and further divided into three aspects: technical, informational, and organizational. In addition, a smart grid interoperability maturity model is developed by GridWise, which provides a means to measure interoperability maturity for interoperability progress assessment, gap analysis, and interoperability improvement.

Intelligrid: The project Intelligrid divides power system functions into six categories to address the business needs of power system operation requirements for today's and future power systems [239]. Intelligrid also defines a communication and information environment including configuration, quality of service, security, and data management requirements for better interoperability in each function categories.

GridBlocks: The Cisco GridBlocks™ architecture provides a forward-looking view on how the electrical grid can be integrated with digital communications across the power delivery chain. The model is a starting point for creating utility-specific designs, and offers guidance on deployment of grid-specific applications [240]. It also lays out a framework for designing and deploying comprehensive management and security solutions across the grid. This will help utilities to lower the total cost of ownership of their communication infrastructure, as well as create additional value by helping to enable new utility services.

8.2.6. Cyber security

SGIP: The Smart Grid Interoperability Panel (SGIP) published the guidelines for smart grid cyber *security*, which proposes a logical reference *model* that shows logical interfaces linking actors and suggests the types of information exchanged [241]. SGIP extends each of the seven major domains of the NIST conceptual model to several sub-domains that exchange information and make decisions for

smart grids. SGIP also defines the logical interfaces among the sub-domains. These logical interfaces describe where the smart grid should provide security and what technology requirements the smart grid needs to ensure security. Also, a Risk Management Framework is proposed to assess the risk of smart grid components and systems, providing guidance on security practices.

TCIPG: The Trustworthy Cyber Infrastructure for the Power Grid (TCIPG), focuses on the security of data transmission and computation systems in power utilities [242]. It studies the methods to increase the ability osf power grid infrastructures to withstand cyber-attacks and other failures due to natural causes or operation errors. TCIPG research covers the following categories: a). wide-area and local-area management, monitoring *and* control security b) detection, response and management of cyber events. c). methods and tools for assessment power grids' resilience to cyber-attacks and cyber-events. The security research in TCIPG covers different data layers vulnerable to security issues in future power grids.

8.3. Next-generation data architecture for high-renewable power grids

Current research projects cover many important aspects of power grid data architecture, such as data transmission, the data service layer, interoperability, and network security. Extensive research results have been achieved through multiple conceptual designs, as well as some prototype system development and demonstration. New requirements for the data architecture due to renewable integration and demand response are well-studied. Nevertheless, some research gaps still need to be explored.

(1) Most current research is in the theoretical and methodology research stage. Since a specific technology or an architecture design needs a corresponding use case for verification, practical projects to demonstrate the performance of conceptual designs are necessary. In addition, interoperability experiments are needed to testify if an architecture meets interoperability requirements, and detailed technical implementation guidelines should also be formulated.

(2) Structural requirements for emerging applications like distributed control, real-time closed-loop control remain to be addressed. For instance, designing communication protocols for control message transmission in real-time wide-area closed-loop control is still a challenge.

(3) An open source power grid application development platform can be established based on standard data sources and interfaces. This will help developers to focus more on algorithms and control strategies designing, and not worrying about interfaces and data formats.

Considering the data architecture requirements and challenges for high renewable power grids, a reference data architecture framework is presented in Figure 8.1. The necessary elements of the data architecture include the following aspects.

8.3.1. Data acquisition

Grid operation and control applications highly relies on data with sufficient quality and quantity. The data collection and actuation layer contains an increasing number of sensors and actuators in power systems. High performance data

acquisition hardware and software are required for capturing the fast dynamics of the system components:

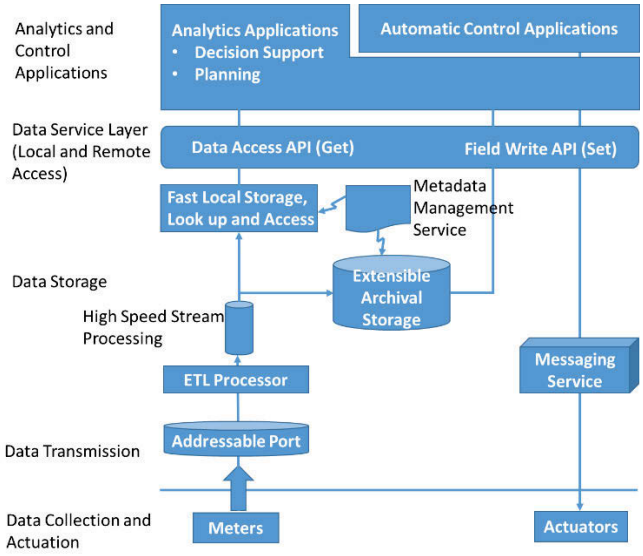

Figure 8.1. A reference framework of data architecture for future power grids [243].

- High-frequency sensors are needed to collect the states of power grids.
- High-speed analog-digital signal circuits are essential to form the real-time data stream.
- Precise universal time information is required to synchronize and tag the data.

The various types and increasing number of sensors and actuators may create huddles originated from this bottom layer towards upper layers including communication infrastructure, distributed controllers and control centers. One additional improvement target in this layer is the standardization of data formats to provide more interoperability and scalability.

8.3.2. Data condition and synchronization, data storage

Since data from various resources in power grids can have different communication delay or formats, the raw data may need some pre-processing procedures, such as timestamp aligning for synchrophasor data and Extract, Transform, and Load (ETL) to format heterogeneous data, for easy storage, querying, and analysis. Real-time applications need fast data storage such as a memory-based database to achieve fast data querying. Off-line applications need high volume and structural databases, as well as distributed techniques.

Metadata is expected to play an increasingly important role in this process. The metadata, which is often referred as “data of data”, include information on how to use data, such as the data format and information on data security management. In addition, metadata improves the transparency of power grid data sources and increases the reuse rates of database interfaces.

8.3.3. Data middleware/API

Data middleware provides data communication interfaces for applications and databases in the power grid. These interfaces offer data exchange approaches. The middleware of the data system provides two types of data service: 1) High-performance real-time data service. This service operates a large amount of real-time data to meet the demand of increasing volumes of real-time data in emerging applications. 2) Flexible historical data service. The services feeds historical data into various off-line analysis and commercial applications in power grids.

The data middleware provides data service for various applications within one control center. Combining the metadata and generic data interfaces, many inherited interfaces can be developed for specific applications to provide specific

data service satisfying different requirements. The communication media in data middleware can be wired or wireless networks, from sensors to local controllers or regional grid control centers, from controllers to actuators, or between controllers. Different communication protocols vary on costs, bandwidth, security, and latency. The adoption of communication depends on the specific communication demands. In addition, since data middleware implements unified data service management, the bandwidth resource of the communication can be dynamically optimized.

Data middleware is expected to possess a high level of interoperability, which facilitates all components of a system to exchange information and use that information for the correct execution of specified functions. One effective way to achieve interoperability is standardization.

8.3.4. Control middleware/API

Power grid control is the main measure to ensure the power grid safety and stability. Due to the deregulation of power markets and the development of distribution resources and demand response, applications are constantly improving and extending. The power grid applications, depending on their focuses, cover wide ranges of spatial, timing, and physical layers of the power grid. These applications tend to exist in a modular form to improve scalability. They are typically capable of exchanging analysis results between each other to achieve more advanced control and analysis functions [244].

For example, in wide-area real-time control applications, the control signals generated by applications are sent to control middleware, which further transmits it to remote control actuators. The control middleware should have short time delay and can manage the delivery of multiple control signals simultaneously to

coordinate the execution. These control applications are also closely tied with advanced situational awareness applications supported various other hardware and software for monitoring and analysis. They can also be linked to other management applications to allow accountability and other market or regulation considerations.

8.4. Conclusions

This chapter identified the challenges in data architecture for operating future high-renewable power grid. A conceptual data architecture and its characteristics are defined to meet the identified requirements and bridge the gaps. Although this chapter aims to cover the data architecture on various perspective, this study remains at the conceptual level. More detailed technical studies, prototype design, system testing, and filed demonstration are required to realize the conceptual architecture.

Table 8.2. Overview on power grid architecture research

Project Name	Objective/Content	Major accomplishments	Focus on data architecture
Grid Edge	· Technology, business, and policy in medium- and low-voltage power grid	· Grid edge taxonomy architecture	· Data collection · Data analytics
iTESLA	· Dynamic security assessment considering uncertainties	· Definition of required external data needs · Conversion tools for format conversion · Uncertainties modeling for security assessments	· Data analytics · Data collection and management
GridStat	· Delivery of power grid operational status information	· Publish-Subscribe based data middleware	· Data transmission
NASPInet	· Data communication infrastructure to support synchrophasor applications	· High-level conceptual synchrophasor communication architecture	· Data transmission
OpenADR	· Standardized and interoperable automated demand response	· An open and interoperable information exchange model for demand response	· Data transmission
GridOPTICS™	· Next-generation concepts and tools for grid operation and planning	· A software framework for power system operations and planning	· Data management · Software framework
INDE	· High performance in smart grid data management	· Accenture Intelligent Network Data Enterprise Platform	· Data management
SERA	· Enables technology innovation and advancements needed to create smart grid ecosystems	· Smart Energy Reference Architecture · Information architecture using Microsoft technologies	· Software framework
SAFE	· Smarter utility solutions across all areas of a utility	· Solution Architecture for Energy and Utilities	· Software framework

Table 8.2. Continued

Project Name	Objective/Content	Major accomplishments	Focus on data architecture
NIST framework	· Guidelines for interoperable standards	· Framework and roadmap for smart grid interoperability standards	· Interoperability
IEEE P2030	· Guidelines for smart grid interoperability	· Smart grid interoperability reference model including power system, communication, and information technology architecture	· Interoperability
IEC TC 57	· IEC Smart Grid Standardization Roadmap	· TC 57 reference architecture · Service-oriented architecture	· Interoperability
SGRA	· Provides guidelines for smart grid interoperability	· Smart Grid Reference Architecture	· Interoperability
GridWise	· Establishes interoperability principles	· Interoperability Context- Setting Framework · Smart Grid Interoperability Maturity Model	· Interoperability
IntelliGrid	· Integrates energy delivery systems and information systems	· Power system functions definition and analysis · IntelliGrid Architecture Framework	· Interoperability
GridBlocks	· Integrates information and communication technologies into electric power systems	· Smart Grid Reference Architecture · Cisco GridBlocks Architecture	· Interoperability
SGIP	· Accelerates the implementation of interoperable smart grid devices/systems	· Smart grid logical reference model · Catalog of standards for smart grid	· Cyber security
TCIPG	· Secures low-level devices, communications, and data systems	· Application-aware detection and recovery mechanisms · Protocol definition for secure data transportation · A combined simulation/testbed environment	· Cyber security

CHAPTER NINE
CONCLUSIONS

This dissertation mainly explores electromechanical dynamics of future high renewable power grids. Conclusions obtained in this dissertation's study include:

1. A scenario creation method is proposed to capture the variation and correlation of load and wind power across regions for large-scale power grids. This scenario creation method can efficiently incorporate uncertainties and operation details into the MIP model for generation and transmission expansion co-optimization. The scenario creation method is verified through comparing the long-term and short-term simulation results of the US EI system.

2. The frequency response of the EI under high PV penetration shows that the system frequency response performance decreases with the increase of PV penetration. In addition, regional frequency could drop much sharper and activate UFLS under high PV penetration.

3. High PV penetration has substantial impact on the inter-area oscillation of the EI, including oscillation frequencies, damping, and mode shapes. It is found that oscillation frequency increases and damping slightly decreases as PV penetration increases in the EI system. It is also found that variations in PV control strategies and parameters may create new oscillation modes.

4. Simulation results indicate that, as PV penetration increases, Florida (FRCC) becomes more vulnerable to rotor angle instability and loss of synchronization with the EI. An obvious correlation is observed between PV penetration and electromechanical wave propagation speed in the EI. The average propagation

speed increases from 500 miles per second for the base case to around 1,800 miles per second for the 80% renewable penetration scenario.

5. Synchronous generation governor and fast load response can significantly influence system frequency stability. More specifically, results show that the governor ratio (the percentage of generation providing governor response) has an obvious impact on the system frequency response. Reducing the governor droop can also make system frequency deviation smaller after contingencies. In addition, if load response can be activated fast, the decline of frequency can be quickly stopped. Besides, active power control of renewable generation has large potential in improving the EI and ERCOT systems' frequency response.

6. Electromechanical wave propagation is utilized for event location without requiring a pre-assumed propagation speed and inertia distribution change detection. The disturbance location and inertia distribution change information is useful to improve the resilience of future high renewable power grids.

LIST OF REFERENCES

1. Manickavasagam, M., M.F. Anjos, and W.D. Rosehart, *Sensitivity-based chance-constrained Generation Expansion Planning.* Electric Power Systems Research, 2015. **127**: p. 32-40.
2. Mirhosseini Moghaddam, M., et al., *Coordinated decisions for transmission and generation expansion planning in electricity markets.* International Transactions on Electrical Energy Systems, 2013. **23**(8): p. 1452-1467.
3. Mortaz, E., et al., *Transmission expansion planning using multivariate interpolation.* Electric Power Systems Research, 2015. **126**: p. 87-99.
4. Sousa, A.S. and E.N. Asada, *Long-term transmission system expansion planning with multi-objective evolutionary algorithm.* Electric Power Systems Research, 2015. **119**: p. 149-156.
5. Hemmati, R., R.-A. Hooshmand, and A. Khodabakhshian, *Coordinated generation and transmission expansion planning in deregulated electricity market considering wind farms.* Renewable Energy, 2016. **85**: p. 620-630.
6. Zhang, Y., J. Wang, and X. Wang, *Review on probabilistic forecasting of wind power generation.* Renewable and Sustainable Energy Reviews, 2014. **32**: p. 255-270.
7. Wang, Q., et al. *Analyzing the impacts of increased wind power on generation Revenue Sufficiency*. in *Power and Energy Society General Meeting (PESGM), 2016*. 2016. IEEE.
8. Zhang, Y. and J. Wang, *K-nearest neighbors and a kernel density estimator for GEFCom2014 probabilistic wind power forecasting.* International Journal of Forecasting, 2016. **32**(3): p. 1074-1080.
9. Zhang, Y., J. Wang, and X. Luo, *Probabilistic wind power forecasting based on logarithmic transformation and boundary kernel.* Energy Conversion and Management, 2015. **96**: p. 440-451.
10. Zhang, B., et al., *Review of Reactive Power Dispatch Strategies for Loss Minimization in a DFIG-based Wind Farm.* Energies, 2017. **10**(7): p. 856.
11. Lopez, A., et al., *US renewable energy technical potentials: a GIS-based analysis.* Contract, 2012. **303**: p. 275-3000.
12. Wang, R., et al. *A Novel Transmission Planning Method for Integrating Large-Scale Wind Power*. in *Power and Energy Engineering Conference (APPEEC), 2012 Asia-Pacific*. 2012. IEEE.
13. Aghaei, J., et al., *Generation and Transmission Expansion Planning: MILP–Based Probabilistic Model.* Power Systems, IEEE Transactions on, 2014. **29**(4): p. 1592-1601.
14. Wang, J., et al., *Flexible Transmission Expansion Planning for Integrating Wind Power Based on Wind Power Distribution Characteristics.* Journal of Electrical Engineering & Technology, 2015. **10**(3): p. 709-718.
15. Dehghan, S., N. Amjady, and A. Kazemi, *Two-stage robust generation expansion planning: a mixed integer linear programming model.* Power Systems, IEEE Transactions on, 2014. **29**(2): p. 584-597.

16. da Rocha, M.C. and J.T. Saraiva, *A discrete evolutionary PSO based approach to the multiyear transmission expansion planning problem considering demand uncertainties.* International Journal of Electrical Power & Energy Systems, 2013. **45**(1): p. 427-442.
17. Hinojosa, V., N. Galleguillos, and B. Nuques, *A simulated rebounding algorithm applied to the multi-stage security-constrained transmission expansion planning in power systems.* International Journal of Electrical Power & Energy Systems, 2013. **47**: p. 168-180.
18. Bakirtzis, G.A., P.N. Biskas, and V. Chatziathanasiou, *Generation expansion planning by MILP considering mid-term scheduling decisions.* Electric Power Systems Research, 2012. **86**: p. 98-112.
19. Zhao, J.H., et al., *Flexible transmission network planning considering distributed generation impacts.* Power Systems, IEEE Transactions on, 2011. **26**(3): p. 1434-1443.
20. Zhang, Y., et al., *An Extension of Reduced Disjunctive Model for Multi-Stage Security-Constrained Transmission Expansion Planning.* IEEE Transactions on Power Systems, 2017.
21. Park, J.-B., et al., *An improved genetic algorithm for generation expansion planning.* Power Systems, IEEE Transactions on, 2000. **15**(3): p. 916-922.
22. Sepasian, M.S., et al., *A multiyear security constrained hybrid generation-transmission expansion planning algorithm including fuel supply costs.* Power Systems, IEEE Transactions on, 2009. **24**(3): p. 1609-1618.
23. Kannan, S., et al., *Application of NSGA-II algorithm to generation expansion planning.* Power Systems, IEEE Transactions on, 2009. **24**(1): p. 454-461.
24. Murugan, P., S. Kannan, and S. Baskar, *NSGA-II algorithm for multi-objective generation expansion planning problem.* Electric Power Systems Research, 2009. **79**(4): p. 622-628.
25. Yang, N. and F. Wen, *A chance constrained programming approach to transmission system expansion planning.* Electric Power Systems Research, 2005. **75**(2): p. 171-177.
26. Jabr, R., *Robust transmission network expansion planning with uncertain renewable generation and loads.* Power Systems, IEEE Transactions on, 2013. **28**(4): p. 4558-4567.
27. Pozo, D., E.E. Sauma, and J. Contreras, *A three-level static MILP model for generation and transmission expansion planning.* Power Systems, IEEE Transactions on, 2013. **28**(1): p. 202-210.
28. Jin, S. and S.M. Ryan, *A tri-level model of centralized transmission and decentralized generation expansion planning for an electricity market—Part I.* Power Systems, IEEE Transactions on, 2014. **29**(1): p. 132-141.
29. Alizadeh, B. and S. Jadid, *Reliability constrained coordination of generation and transmission expansion planning in power systems using mixed integer*

programming. Generation, Transmission & Distribution, IET, 2011. **5**(9): p. 948-960.
30. Alizadeh, B. and S. Jadid, *A dynamic model for coordination of generation and transmission expansion planning in power systems.* International Journal of Electrical Power & Energy Systems, 2015. **65**: p. 408-418.
31. Fallahi, F., et al., *The value of energy storage in optimal non-firm wind capacity connection to power systems.* Renewable Energy, 2014. **64**: p. 34-42.
32. Javadi, M., M. Saniei, and H. Rajabi Mashhadi, *An augmented NSGA-II technique with virtual database to solve the composite generation and transmission expansion planning problem.* Journal of Experimental & Theoretical Artificial Intelligence, 2014. **26**(2): p. 211-234.
33. Unsihuay-Vila, C., et al., *Multistage expansion planning of generation and interconnections with sustainable energy development criteria: A multiobjective model.* International Journal of Electrical Power & Energy Systems, 2011. **33**(2): p. 258-270.
34. Moeini-Aghtaie, M., A. Abbaspour, and M. Fotuhi-Firuzabad, *Incorporating large-scale distant wind farms in probabilistic transmission expansion planning—Part I: Theory and algorithm.* Power Systems, IEEE Transactions on, 2012. **27**(3): p. 1585-1593.
35. Yu, H., et al., *A chance constrained transmission network expansion planning method with consideration of load and wind farm uncertainties.* Power Systems, IEEE Transactions on, 2009. **24**(3): p. 1568-1576.
36. Orfanos, G.A., P.S. Georgilakis, and N.D. Hatziargyriou, *Transmission expansion planning of systems with increasing wind power integration.* Power Systems, IEEE Transactions on, 2013. **28**(2): p. 1355-1362.
37. Gu, Y., J.D. McCalley, and M. Ni, *Coordinating large-scale wind integration and transmission planning.* Sustainable Energy, IEEE Transactions on, 2012. **3**(4): p. 652-659.
38. Dehghan, S., N. Amjady, and A.J. Conejo, *Reliability-Constrained Robust Power System Expansion Planning.* Power Systems, IEEE Transactions on, 2016.
39. Arabali, A., et al., *A Multi-Objective Transmission Expansion Planning Framework in Deregulated Power Systems With Wind Generation.* Power Systems, IEEE Transactions on, 2014. **29**(6): p. 3003-3011.
40. Chen, B., et al., *Robust optimization for transmission expansion planning: Minimax cost vs. minimax regret.* Power Systems, IEEE Transactions on, 2014. **29**(6): p. 3069-3077.
41. Roh, J.H., M. Shahidehpour, and L. Wu, *Market-based generation and transmission planning with uncertainties.* Power Systems, IEEE Transactions on, 2009. **24**(3): p. 1587-1598.

42. Borges, C.L.T. and V.F. Martins, *Multistage expansion planning for active distribution networks under demand and distributed generation uncertainties.* International Journal of Electrical Power & Energy Systems, 2012. **36**(1): p. 107-116.
43. Delgado, D. and J. Claro, *Transmission network expansion planning under demand uncertainty and risk aversion.* International Journal of Electrical Power & Energy Systems, 2013. **44**(1): p. 696-702.
44. Yu, H., C. Chung, and K. Wong, *Robust transmission network expansion planning method with Taguchi's orthogonal array testing.* Power Systems, IEEE Transactions on, 2011. **26**(3): p. 1573-1580.
45. Maghouli, P., et al., *A scenario-based multi-objective model for multi-stage transmission expansion planning.* Power Systems, IEEE Transactions on, 2011. **26**(1): p. 470-478.
46. Feng, Y. and S.M. Ryan, *Scenario construction and reduction applied to stochastic power generation expansion planning.* Computers & Operations Research, 2013. **40**(1): p. 9-23.
47. Bent, R., A. Berscheid, and G.L. Toole. *Generation and transmission expansion planning for renewable energy integration*. in *Power Systems Computation Conference (PSCC)*. 2011. Citeseer.
48. Kamyab, G.-R., M. Fotuhi-Firuzabad, and M. Rashidinejad, *A PSO based approach for multi-stage transmission expansion planning in electricity markets.* International Journal of Electrical Power & Energy Systems, 2014. **54**: p. 91-100.
49. You, S., et al., *Co-optimizing generation and transmission expansion with wind power in large-scale power grids—Implementation in the US Eastern Interconnection.* Electric Power Systems Research, 2016. **133**: p. 209-218.
50. Energy Exemplar, *PLEXOS Integrated Energy Model.* 2014.
51. Charles River Associates, *Working Draft of MRN-NEEM Modeling Assumptions and Data Sources for EIPC Capacity Expansion Modeling.* 2010.
52. Haffner, S., et al., *Branch and bound algorithm for transmission system expansion planning using a transportation model.* IEE Proceedings-Generation, Transmission and Distribution, 2000. **147**(3): p. 149-156.
53. Romero, R., et al. *Analysis of heuristic algorithms for the transportation model in static and multistage planning in network expansion systems*. in *Generation, Transmission and Distribution, IEE Proceedings-*. 2003. IET.
54. Hadley, S.W., *Additional EIPC Study Analysis: Interim Report on High Priority Topics*. 2013, Oak Ridge National Laboratory (ORNL). .
55. Hadley, S., et al., *Electric Grid Expansion Planning with High Levels of Variable Generation*. 2015, ORNL/TM-2015/515: Oak Ridge National Laboratory.

56. Energy Exemplar, *Co-Optimization of Transmission and Other Resources*. 2015, National Association of Regulatory Utility Commisioners.
57. Wu, L., et al. *Observation of inertial frequency response of main power grids worldwide using FNET/GridEye*. in *Power and Energy Society General Meeting (PESGM), 2016*. 2016. IEEE.
58. Tan, J., et al. *Investigating Power System Primary and Secondary Reserve Interaction under High Wind Power Penetration Using Frequency Response Model*. in *Grid of the Future Symposium, Chicago*. 2015.
59. Tan, J., et al., *Investigating Power System Primary and Secondary Reserve Interaction under High Wind Penetration Using Frequency Response Model*. 2015, NREL (National Renewable Energy Laboratory (NREL), Golden, CO (United States)).
60. Guo, J., et al. *An ensemble solar power output forecasting model through statistical learning of historical weather dataset*. in *Power and Energy Society General Meeting (PESGM), 2016*. 2016. IEEE.
61. Till, M.J., et al. *Frequency response of the Eastern Interconnection due to increased wind generation*. in *2014 IEEE PES General Meeting| Conference & Exposition*. 2014. IEEE.
62. Eto, J.H., *Use of frequency response metrics to assess the planning and operating requirements for reliable integration of variable renewable generation.* Lawrence Berkeley National Laboratory, 2011.
63. Eftekharnejad, S., et al., *Impact of increased penetration of photovoltaic generation on power systems.* IEEE transactions on power systems, 2013. **28**(2): p. 893-901.
64. Tamimi, B., C. Cañizares, and K. Bhattacharya, *System stability impact of large-scale and distributed solar photovoltaic generation: The case of Ontario, Canada.* IEEE Transactions on Sustainable Energy, 2013. **4**(3): p. 680-688.
65. Seneviratne, C. and C. Ozansoy, *Frequency response due to a large generator loss with the increasing penetration of wind/PV generation–A literature review.* Renewable and Sustainable Energy Reviews, 2016. **57**: p. 659-668.
66. Yan, R., et al., *The combined effects of high penetration of wind and PV on power system frequency response.* Applied Energy, 2015. **145**: p. 320-330.
67. SunShot, E.E., *US Department of Energy, 2012. SunShot Vision Study: February 2012. NREL Report No. BK5200-47927*. DOE/GO-102012-3037.
68. Tan, J., et al. *Developing High PV Penetration Cases for Frequency Response Study of US Western Interconnection*. in *Green Technologies Conference (GreenTech), 2017 Ninth Annual IEEE*. 2017. IEEE.
69. You, S., et al. *Impact of High PV Penetration on U.S. Eastern Interconnection Frequency Response*. in *Power and Energy Society General Meeting (PESGM), 2017*. 2017. IEEE.

70. Eastern Interconnection Planning Collaborative, *Phase 2 Report: DOE Draft – Part 1 Interregional Transmission Development and Analysis for Three Stakeholder Selected Scenarios.* 2013.
71. Kou, G., et al. *Developing generic dynamic models for the 2030 eastern interconnection grid*. in *2014 IEEE PES T&D Conference and Exposition*. 2014. IEEE.
72. Zhang, Y., et al., *Wide-area frequency monitoring network (FNET) architecture and applications.* Smart Grid, IEEE Transactions on, 2010. **1**(2): p. 159-167.
73. Liu, Y., et al., *Wide-Area-Measurement System Development at the Distribution Level: An FNET/GridEye Example.* IEEE Transactions on Power Delivery, 2016. **31**(2): p. 721-731.
74. Subcommittee, N., *ALR1-12 interconnection frequency response.* http://www.nerc.com/pa/RAPA/ri/Pages/InterconnectionFrequencyResponse.aspx, 2015.
75. Lauby, M., et al. *Eastern interconnection frequency response trends*. in *Power and Energy Society General Meeting (PES), 2013 IEEE*. 2013. IEEE.
76. Ingleson, J.W. and D.M. Ellis. *Tracking the eastern interconnection frequency governing characteristic*. in *IEEE Power Engineering Society General Meeting, 2005*. 2005. IEEE.
77. Chen, L., *Wide-area measurement application and power system dynamics.* 2011.
78. Kou, G., et al., *Impact of governor deadband on frequency response of the US Eastern Interconnection.* IEEE Transactions on Smart Grid, 2016. **7**(3): p. 1368-1377.
79. Kou, G., S. Hadley, and Y. Liu, *Dynamic model validation with governor deadband on the eastern interconnection.* Oak Ridge Nat. Lab., Power and Energy Syst. Group, Oak Ridge, TN, USA, Tech. Rep. ORNL/TM-2014/40, 2014.
80. Miller, N., et al., *Eastern frequency response study.* Contract, 2013. **303**: p. 275-3000.
81. Singarao, V.Y. and V.S. Rao, *Frequency responsive services by wind generation resources in United States.* Renewable and Sustainable Energy Reviews, 2016. **55**: p. 1097-1108.
82. Bloomberg New Energy Finance, *H1 2015 North American PV Outlook.* 2015.
83. United States Department of Agriculture, *Land Value 2015 Summary.* 2015.
84. Bloom, A., A. Townsend, and D. Palchak, *The Eastern Renewable Generation Integration Study: Flexibility and High Penetrations of Wind and Solar.* 2015.

85. Clark, K., R. Walling, and N. Miller. *Solar photovoltaic (PV) plant models in PSLF*. in *2011 IEEE Power and Energy Society General Meeting*. 2011. IEEE.
86. Altman, R. and Y. Kazachkov, *PSS®E Modeling Package for GE Photovoltaic Converters.* Siemens Energy, Inc., 2011.
87. Subcommittee, N., *Balancing and frequency control.* NERC, Princeton, 2011.
88. Kou, G., et al. *Rotor angle stability and inter-area oscillation damping studies on the US Eastern Interconnection (EI) under high wind conditions*. in *Power and Energy Society General Meeting (PESGM), 2016*. 2016. IEEE.
89. Vittal, E., M. O'Malley, and A. Keane, *Rotor angle stability with high penetrations of wind generation.* IEEE transactions on Power Systems, 2012. **27**(1): p. 353-362.
90. Edrah, M., K.L. Lo, and O. Anaya-Lara, *Impacts of high penetration of DFIG wind turbines on rotor angle stability of power systems.* IEEE Transactions on Sustainable Energy, 2015. **6**(3): p. 759-766.
91. Vittal, E., M. O'Malley, and A. Keane, *A steady-state voltage stability analysis of power systems with high penetrations of wind.* IEEE Transactions on Power Systems, 2010. **25**(1): p. 433-442.
92. Miller, N.W., et al. *Frequency Response of the US Eastern Interconnection Under Conditions of High Wind and Solar Generation*. in *2015 Seventh Annual IEEE Green Technologies Conference*. 2015. IEEE.
93. Liu, Y., et al., *Frequency Regulation and Oscillation Damping Contributions of Variable-Speed Wind Generators in the U.S. Eastern Interconnection (EI).* Sustainable Energy, IEEE Transactions on, 2015. **6**(3): p. 951-958.
94. Tsourakis, G., B.M. Nomikos, and C.D. Vournas, *Contribution of doubly fed wind generators to oscillation damping.* IEEE Transactions on energy conversion, 2009. **24**(3): p. 783-791.
95. Gautam, D., V. Vittal, and T. Harbour, *Impact of increased penetration of DFIG-based wind turbine generators on transient and small signal stability of power systems.* IEEE Transactions on Power Systems, 2009. **24**(3): p. 1426-1434.
96. Quintero, J., et al., *The impact of increased penetration of converter control-based generators on power system modes of oscillation.* IEEE Transactions on Power Systems, 2014. **29**(5): p. 2248-2256.
97. Bin, W. and S. Kai, *Location methods of oscillation sources in power systems: a survey.* Journal of Modern Power Systems and Clean Energy, 2017. **5**(2): p. 151-159.
98. Wang, B. and K. Sun, *Formulation and characterization of power system electromechanical oscillations.* IEEE Transactions on Power Systems, 2016. **31**(6): p. 5082-5093.

99. Wang, B., X. Su, and K. Sun, *Properties of the Frequency–Amplitude Curve.* IEEE Transactions on Power Systems, 2017. **32**(1): p. 826-827.
100. Shah, R., N. Mithulananthan, and R. Bansal, *Oscillatory stability analysis with high penetrations of large-scale photovoltaic generation.* Energy Conversion and Management, 2013. **65**: p. 420-429.
101. Eftekharnejad, S., et al., *Small signal stability assessment of power systems with increased penetration of photovoltaic generation: A case study.* IEEE Transactions on Sustainable Energy, 2013. **4**(4): p. 960-967.
102. Shah, R., et al. *Impact of large-scale PV penetration on power system oscillatory stability*. in *IEEE PES General Meeting*. 2010. IEEE.
103. Tamimi, B., C. Cañizares, and K. Bhattacharya. *Modeling and performance analysis of large solar photo-voltaic generation on voltage stability and inter-area oscillations*. in *2011 IEEE Power and Energy Society General Meeting*. 2011. IEEE.
104. Shah, R., N. Mithulananthan, and R. Bansal, *Damping performance analysis of battery energy storage system, ultracapacitor and shunt capacitor with large-scale photovoltaic plants.* Applied energy, 2012. **96**: p. 235-244.
105. Du, W., H. Wang, and R. Dunn. *Power system small-signal oscillation stability as affected by large-scale PV penetration*. in *2009 International Conference on Sustainable Power Generation and Supply*. 2009. IEEE.
106. Elliott, R., et al. *Impact of increased photovoltaic generation on inter-area oscillations in the Western North American power system*. in *2014 IEEE PES General Meeting| Conference & Exposition*. 2014. IEEE.
107. You, S., et al., *Impact of High PV Penetration on the Inter-area Oscillations in the US Eastern Interconnection.* IEEE Access, 2017.
108. You, S., et al., *Oscillation mode identification based on wide-area ambient measurements using multivariate empirical mode decomposition.* Electric Power Systems Research, 2016. **134**: p. 158-166.
109. You, S., et al. *Ring-down oscillation mode identification using multivariate empirical mode decomposition*. in *Power and Energy Society General Meeting (PESGM), 2016*. 2016. IEEE.
110. Liu, Y., et al., *A Distribution Level Wide Area Monitoring System for the Electric Power Grid – FNET/GridEye.* IEEE Access, 2017.
111. Liu, Y., S. You, and Y. Liu, *Smart Transmission & Wide Area Monitoring System*, in *Communication, Control and Security for the Smart Grid*. 2017, IET.
112. Liu, Y., et al., *Recent developments of FNET/GridEye—A situational awareness tool for smart grid.* CSEE Journal of Power and Energy Systems, 2016. **2**(3): p. 19-27.

113. Wu, L., et al. *Statistical Analysis of the FNET/GridEye-detected Inter-area Oscillations in Eastern Interconnection (EI)*. in *Power & Energy Society General Meeting, 2017 IEEE*. 2017. IEEE.
114. Cui, Y., et al., *Inter-area Oscillation Statistical Analysis of the US Eastern Interconnection.* The Journal of Engineering, 2017. **1**(1).
115. Crow, M.L. and A. Singh, *The matrix pencil for power system modal extraction.* IEEE Transactions on Power Systems, 2005. **20**(1): p. 501-502.
116. Zhu, Y., et al. *Microgrid security assessment and islanding control by Support Vector Machine*. in *Power & Energy Society General Meeting, 2015 IEEE*. 2015. IEEE.
117. Akhrif, O., et al., *Application of a multivariable feedback linearization scheme for rotor angle stability and voltage regulation of power systems.* IEEE Transactions on Power Systems, 1999. **14**(2): p. 620-628.
118. Faulk, D. and R. Murphy. *Comanche peak unit No 2 100 percent load rejection test–underfrequency and voltage phasors measured across TU electric system*. in *Protective Relay Conference Texas A&M*. 1994.
119. Phadke, A. and J. Thorp, *Electromechanical Wave Propagation.* Synchronized Phasor Measurements and Their Applications, 2008: p. 223-243.
120. Gardner, R.M., J.K. Wang, and Y. Liu. *Power system event location analysis using wide-area measurements*. in *Power Engineering Society General Meeting, 2006. IEEE*. 2006. IEEE.
121. You, S., et al., *Non-Invasive Identification of Inertia Distribution Change in High Renewable Systems Using Distribution Level PMU.* IEEE Transactions on Power Systems, 2017.
122. Zhang, Y., et al., *Chance-Constrained Two-Stage Unit Commitment under Uncertain Load and Wind Power Output Using Bilinear Benders Decomposition.* IEEE Transactions on Power Systems, 2017.
123. Semlyen, A., *Analysis of disturbance propagation in power systems based on a homogeneoue dynamic model.* Power Apparatus and Systems, IEEE Transactions on, 1974(2): p. 676-684.
124. Thorp, J.S., C.E. Seyler, and A.G. Phadke, *Electromechanical wave propagation in large electric power systems.* Circuits and Systems I: Fundamental Theory and Applications, IEEE Transactions on, 1998. **45**(6): p. 614-622.
125. Dersin, P. and A.H. Levis, *Aggregate feasibility sets for large power networks*. 1984: Laboratory for Information and Decision Systems, Massachusetts Institute of Technology.
126. Parashar, M., J.S. Thorp, and C.E. Seyler, *Continuum modeling of electromechanical dynamics in large-scale power systems.* Circuits and Systems I: Regular Papers, IEEE Transactions on, 2004. **51**(9): p. 1848-1858.

127. Tsai, S.-J., et al., *Frequency sensitivity and electromechanical propagation simulation study in large power systems.* Circuits and Systems I: Regular Papers, IEEE Transactions on, 2007. **54**(8): p. 1819-1828.
128. Lesieutre, B.C., E. Scholtz, and G.C. Verghese. *Impedance matching controllers to extinguish electromechanical waves in power networks*. in *Control Applications, 2002. Proceedings of the 2002 International Conference on*. 2002. IEEE.
129. Zhong, Z., et al., *Power system frequency monitoring network (FNET) implementation.* Power Systems, IEEE Transactions on, 2005. **20**(4): p. 1914-1921.
130. Liu, Y., et al., *A Distribution Level Wide Area Monitoring System for the Electric Power Grid–FNET/GridEye.* IEEE Access, 2017. **5**: p. 2329-2338.
131. Markham, P.N. and Y. Liu. *Electromechanical speed map development using FNET/GridEye frequency measurements*. in *PES General Meeting| Conference & Exposition, 2014 IEEE*. 2014. IEEE.
132. You, S., et al., *Disturbance Location Determination Based on Electromechanical Wave Propagation in FNET/GridEye--a Distribution-Level Wide-Area Measurement System.* IET Generation, Transmission & Distribution, 2017.
133. Tan, J. and Y. Zhang, *Coordinated Control Strategy of a Battery Energy Storage System to Support a Wind Power Plant Providing Multi-Timescale Frequency Ancillary Services.* IEEE Transactions on Sustainable Energy, 2017. **8**(3): p. 1140-1153.
134. Tan, J. and Y. Zhang, *Coordinated Control Strategy of a Battery Energy Storage System to Support a Wind Power Plant Providing Multi-Timescale Frequency Ancillary Services.* IEEE Transactions on Sustainable Energy, 2017.
135. You, S., et al., *Impact of High PV Penetration on the Inter-Area Oscillations in the US Eastern Interconnection.* IEEE Access, 2017. **5**: p. 4361-4369.
136. You, S., et al. *Impact of high PV penetration on US eastern interconnection frequency response*. in *Proc. Power Energy Soc. General Meeting (PESGM)*. 2017.
137. Nanou, S.I., A.G. Papakonstantinou, and S.A. Papathanassiou, *A generic model of two-stage grid-connected PV systems with primary frequency response and inertia emulation.* Electric Power Systems Research, 2015. **127**: p. 186-196.
138. Delille, G., B. Francois, and G. Malarange, *Dynamic frequency control support by energy storage to reduce the impact of wind and solar generation on isolated power system's inertia.* IEEE Transactions on Sustainable Energy, 2012. **3**(4): p. 931-939.
139. Zhu, Y., J. Yao, and D. Wu. *Comparative study of two stages and single stage topologies for grid-tie photovoltaic generation by PSCAD/EMTDC*. in

Advanced Power System Automation and Protection (APAP), 2011 International Conference on. 2011. IEEE.
140. Yuan, Z., et al. *Frequency Control Capability of VSC-HVDC for Large Power Systems*. in *Power & Energy Society General Meeting, 2017 IEEE*. 2016. IEEE.
141. Liu, Y., S. You, and Y. Liu, *Study of Wind and PV Frequency Control in U.S. Power Grids – EI and TI Case Studies.* IEEE Power and Energy Technology Systems Journal, 2017.
142. Datta, M., et al., *A frequency-control approach by photovoltaic generator in a PV–diesel hybrid power system.* IEEE Transactions on Energy Conversion, 2011. **26**(2): p. 559-571.
143. Miller, N., *Western Wind and Solar Integration Study Phase 3: Frequency Response and Transient Stability*. 2014.
144. You, S., et al., *Model Development Practice to Study Large Power Grid Dynamics with Photovoltaic Penetration Increases — A Case Study of the U.S. Eastern Interconnection*, in *2018 IEEE/PES Transmission and Distribution Conference and Exposition*. 2018.
145. You, S., et al., *U.S. Eastern Interconnection (EI) Electromechanical Wave Propagation and the Impact of High PV Penetration on Its Speed*, in *2018 IEEE/PES Transmission and Distribution Conference and Exposition*. 2018.
146. Zhang, Y., et al., *Impacts of Power Grid Frequency Deviation on Time Error of Synchronous Electric Clock and Worldwide Power System Practices on Time Error Correction.* Energies, 2017. **10**(9): p. 1283.
147. NERC, *Standard BAL-003-1 — Frequency Response and Frequency Bias Setting.* 2014.
148. WECC Criterion, *PRC-001-WECC-CRT-1.2— Governor Droop Setting.* 2016.
149. NERC, *BAL-001-TRE-1 — Primary Frequency Response in the ERCOT Region.* 2016.
150. Li, W., P. Du, and N. Lu, *Design of a New Primary Frequency Control Market for Hosting Frequency Response Reserve Offers from both Generators and Loads.* IEEE Transactions on Smart Grid, 2017.
151. NERC, *Standard PRC-024-2 — Generator Frequency and Voltage Protective Relay Settings.* 2015.
152. Miller, N., et al., *Emergency response: US system frequency with high wind penetration.* IEEE Power and Energy Magazine, 2013. **11**(6): p. 63-71.
153. Zhang, Y., et al., *Role of wind power in primary frequency response of an interconnection.* National Renewable Energy Laboratory (NREL), Golden, CO, USA, 2013.
154. Singhvi, V., et al. *Impact of wind active power control strategies on frequency response of an interconnection*. in *Power and Energy Society General Meeting (PES), 2013 IEEE*. 2013. IEEE.

155. Arani, M.F.M. and E.F. El-Saadany, *Implementing virtual inertia in DFIG-based wind power generation.* IEEE Transactions on Power Systems, 2013. **28**(2): p. 1373-1384.
156. Morren, J., et al., *Wind turbines emulating inertia and supporting primary frequency control.* IEEE Transactions on Power Systems, 2006. **21**(1): p. 433-434.
157. Lalor, G., A. Mullane, and M. O'Malley, *Frequency control and wind turbine technologies.* IEEE Transactions on Power Systems, 2005. **20**(4): p. 1905-1913.
158. Keung, P.-K., et al., *Kinetic energy of wind-turbine generators for system frequency support.* IEEE Transactions on Power Systems, 2009. **24**(1): p. 279-287.
159. Kayikçi, M. and J.V. Milanovic, *Dynamic contribution of DFIG-based wind plants to system frequency disturbances.* IEEE Transactions on Power Systems, 2009. **24**(2): p. 859-867.
160. Ruttledge, L., et al., *Frequency response of power systems with variable speed wind turbines.* IEEE transactions on Sustainable Energy, 2012. **3**(4): p. 683-691.
161. Ramtharan, G., N. Jenkins, and J. Ekanayake, *Frequency support from doubly fed induction generator wind turbines.* IET Renewable Power Generation, 2007. **1**(1): p. 3-9.
162. Gevorgian, V., Y. Zhang, and E. Ela, *Investigating the impacts of wind generation participation in interconnection frequency response.* IEEE transactions on Sustainable Energy, 2015. **6**(3): p. 1004-1012.
163. Sun, Y.-z., et al. *Review on frequency control of power systems with wind power penetration*. in *Power System Technology (POWERCON), 2010 International Conference on*. 2010. IEEE.
164. Morren, J. and S.W. De Haan, *Ridethrough of wind turbines with doubly-fed induction generator during a voltage dip.* IEEE Transactions on energy conversion, 2005. **20**(2): p. 435-441.
165. Chang-Chien, L.-R., W.-T. Lin, and Y.-C. Yin, *Enhancing frequency response control by DFIGs in the high wind penetrated power systems.* IEEE transactions on power systems, 2011. **26**(2): p. 710-718.
166. Miller, N., K. Clark, and M. Shao. *Frequency responsive wind plant controls: Impacts on grid performance*. in *Power and Energy Society General Meeting, 2011 IEEE*. 2011. IEEE.
167. Miller, N., et al. *Frequency responsive controls for wind plants in grids with wind high penetration*. in *Power and Energy Society General Meeting, 2012 IEEE*. 2012. IEEE.
168. Wilches-Bernal, F., J.H. Chow, and J.J. Sanchez-Gasca, *A Fundamental Study of Applying Wind Turbines for Power System Frequency Control.* IEEE Transactions on Power Systems, 2016. **31**(2): p. 1496-1505.

169. Hoke, A.F., et al., *The Frequency-Watt Function: Simulation and Testing for the Hawaiian Electric Companies*. 2017, National Renewable Energy Laboratory (NREL), Golden, CO (United States).
170. Tuohy, A., et al., *Unit commitment for systems with significant wind penetration.* IEEE Transactions on Power Systems, 2009. **24**(2): p. 592-601.
171. Makarov, Y.V., et al., *Operational impacts of wind generation on California power systems.* IEEE Transactions on Power Systems, 2009. **24**(2): p. 1039-1050.
172. Miller, N., et al. *Frequency response of California and WECC under high wind and solar conditions*. in *Power and Energy Society General Meeting, 2012 IEEE*. 2012. IEEE.
173. Liu, Y., S. You, and Y. Liu, *Study of Wind and PV Frequency Control in US Power Grids–EI and TI Case Studies.* IEEE Power and Energy Technology Systems Journal, 2017.
174. Amin, S.M. and B.F. Wollenberg, *Toward a smart grid: power delivery for the 21st century.* Power and Energy Magazine, IEEE, 2005. **3**(5): p. 34-41.
175. Phadke, A.G. and J.S. Thorp, *Synchronized phasor measurements and their applications*. 2008: Springer Science & Business Media.
176. Beau, J., et al., *An Introduction to Synchrophasors.* University of Tennessee, Knoxville, Tennessee: p. 37996-2250.
177. Liu, Y. *A US-wide power systems frequency monitoring network*. in *Power Systems Conference and Exposition, 2006. PSCE'06. 2006 IEEE PES*. 2006. IEEE.
178. You, S., et al. *Ring-down oscillation mode identification using multivariate empirical mode decomposition*. in *Proc. 2016 IEEE Power and Energy Society General Meeting*. 2016.
179. Guo, J., *Data Analytics and Application Developments Based on Synchrophasor Measurements.* 2016.
180. Chai, J., *Wide-Area Measurement-Based Applications for Power System Monitoring and Dynamic Modeling.* 2016.
181. Hwang, J.K. and Y. Liu, *Discrete Fourier transform-based parametric modal identification from ambient data of the power system frequency.* IET Generation, Transmission & Distribution, 2016. **10**(1): p. 213-220.
182. Ju, W., K. Sun, and J. Qi, *Multi-Layer Interaction Graph for Analysis and Mitigation of Cascading Outages.* IEEE Journal on Emerging and Selected Topics in Circuits and Systems, 2017.
183. Wang, W., et al., *Multiple event detection and recognition through sparse unmixing for high-resolution situational awareness in power grid.* IEEE Transactions on Smart Grid, 2014. **5**(4): p. 1654-1664.
184. Guo, J., et al., *Design and implementation of a real-time off-grid operation detection tool from a wide-area measurements perspective.* IEEE Transactions on Smart Grid, 2015. **6**(4): p. 2080-2087.

185. Gardner, R.M., Z. Zhong, and Y. Liu, *Location determination of power system disturbances based on frequency responses of the system*. 2010, Google Patents.
186. Christy, C. and Y. Zhu. *The application of simple thermal models to improve dynamic load models*. in *Electric Power and Energy Conversion Systems (EPECS), 2013 3rd International Conference on*. 2013. IEEE.
187. Yongli, Z. *Simulation study of PEM Fuel cell and its dynamic characteristics*. in *Power and Energy Society General Meeting (PES), 2013 IEEE*. 2013. IEEE.
188. Lapinski, S. and D. Alphenaar, *Method and system for AC power grid monitoring*. 2006, Google Patents.
189. Gardner, R.M., J.K. Wang, and Y. Liu. *Power system event location analysis using wide-area measurements*. in *2006 IEEE Power Engineering Society General Meeting*. 2006. IEEE.
190. You, S., et al., *Power System Disturbance Location Determination Based on Rate of Change of Frequency*. 2016: U.S.
191. You, S., et al., *Disturbance Location Determination Based on Electromechanical Wave Propagation in FNET/GridEye -- a Distribution-Level Wide-Area Measurement System.* IET Generation, Transmission & Distribution, 2017.
192. Lee, D.-T. and B.J. Schachter, *Two algorithms for constructing a Delaunay triangulation.* International Journal of Computer & Information Sciences, 1980. **9**(3): p. 219-242.
193. Shewchuk, J.R., *Triangle: Engineering a 2D quality mesh generator and Delaunay triangulator*, in *Applied computational geometry towards geometric engineering*. 1996, Springer. p. 203-222.
194. Watson, D., *Contouring: a guide to the analysis and display of spatial data*. Vol. 10. 2013: Elsevier.
195. You, S., et al., *Non-Invasive Identification of Inertia Distribution Change in High Renewable Systems Using Distribution Level PMU.* Power Systems, IEEE Transactions on, 2017.
196. Xu, C., et al., *Practical issues in frequency disturbance recorder design for wide-area monitoring.* Electrical Power Quality and Utilisation. Journal, 2005. **11**(1): p. 69-76.
197. Yao, W., et al., *Synchronized Wireless Measurement of High Voltage Power System Frequency Using Mobile Embedded Systems.* IEEE Transactions on Industrial Electronics, 2017.
198. Liu, Y., et al., *Wide-Area Measurement System Development at the Distribution Level: an FNET/GridEye Example.* Power Delivery, IEEE Transactions on, 2016.

199. Yao, W., et al., *Pioneer Design of Non-contact Synchronized Measurement Devices Using Electric and Magnetic Field Sensors.* IEEE Transactions on Smart Grid, 2017.
200. Zhan, L., et al., *Utilization of chip-scale atomic clock for synchrophasor measurements.* IEEE Transactions on Power Delivery, 2016. **31**(5): p. 2299-2300.
201. Yao, W., et al., *Impact of GPS signal loss and its mitigation in power system synchronized measurement devices.* IEEE Transactions on Smart Grid, 2016.
202. Yao, W., et al., *A novel method for phasor measurement unit sampling time error compensation.* IEEE Transactions on Smart Grid, 2016.
203. Wang, L., et al. *Frequency disturbance recorder design and developments*. in *Power Engineering Society General Meeting, 2007. IEEE*. 2007. IEEE.
204. Yao, W., et al., *GPS signal loss in the wide area monitoring system: Prevalence, impact, and solution.* Electric Power Systems Research, 2017. **147**: p. 254-262.
205. Culliss, J.A., *A 3rd Generation Frequency Disturbance Recorder: A Secure, Low Cost Synchophasor Measurement Device.* 2015.
206. Zhao, J., et al. *Measurement accuracy limitation analysis on synchrophasors*. in *Power & Energy Society General Meeting, 2015 IEEE*. 2015. IEEE.
207. Chai, J., et al. *Application of wide area power system measurement for digital authentication*. in *Transmission and Distribution Conference and Exposition (T&D), 2016 IEEE/PES*. 2016. IEEE.
208. Zhao, J., A. Goldstein, and Y. Liu. *Model of parameterized PMU estimation error*. in *Power & Energy Society General Meeting, 2017 IEEE*. 2017. IEEE.
209. Zhao, J., et al. *PMU error impact on measurement-based applications*. in *Power & Energy Society General Meeting, 2017 IEEE*. 2017. IEEE.
210. Yao, W., et al., *Source Location Identification of Distribution-level Electric Network Frequency Signals at Multiple Geographic Scales.* IEEE Access, 2017.
211. Zhou, D., et al., *Distributed data analytics platform for wide-area synchrophasor measurement systems.* IEEE Transactions on Smart Grid, 2016. **7**(5): p. 2397-2405.
212. Liu, Y., et al., *Wide Area Monitoring through Synchrophasor Measurement.* Smart Grid Handbook.
213. Liu, L., et al. *Power grid disturbance analysis using frequency information at the distribution level*. in *Smart Grid Communications (SmartGridComm), 2014 IEEE International Conference on*. 2014. IEEE.
214. Yingchen, Z., et al., *Wind Power Plant Model Validation Using Synchrophasor Measurements at the Point of Interconnection.* Sustainable Energy, IEEE Transactions on, 2015. **6**(3): p. 984-992.

215. You, S., et al. *A survey on next-generation power grid data architecture*. in *2015 IEEE Power & Energy Society General Meeting*. 2015. IEEE.
216. You, S., et al. *Data Architecture for the Next-Generation Power Grid: Concept, Framework, and Use Case*. in *Information Science and Control Engineering (ICISCE), 2015 2nd International Conference on*. 2015. IEEE.
217. Chernikov, A.N. and N.P. Chrisochoides, *Algorithm 872: Parallel 2D constrained Delaunay mesh generation.* ACM Transactions on Mathematical Software (TOMS), 2008. **34**(1): p. 6.
218. Akima, H., *A method of bivariate interpolation and smooth surface fitting for irregularly distributed data points.* ACM Transactions on Mathematical Software (TOMS), 1978. **4**(2): p. 148-159.
219. Akima, H., *A method of bivariate interpolation and smooth surface fitting for values given at irregularly distributed points*. Vol. 1. 1975: US Department of Commerce, Office of Telecommunications.
220. Akima, H., *Algorithm 761: scattered-data surface fitting that has the accuracy of a cubic polynomial.* ACM Transactions on Mathematical Software (TOMS), 1996. **22**(3): p. 362-371.
221. *ACM Collected Algorithms.* Website: http://calgo.acm.org/.
222. Ye, Y., *Wide-area situational awareness application developments.* 2011.
223. Thorp, J.S., C.E. Seyler, and A.G. Phadke, *Electromechanical wave propagation in large electric power systems.* IEEE Transactions on Circuits and Systems I: Fundamental Theory and Applications, 1998. **45**(6): p. 614-622.
224. Farhangi, H., *The path of the smart grid.* IEEE power and energy magazine, 2010. **8**(1).
225. Li, F., et al., *Smart transmission grid: Vision and framework.* IEEE transactions on Smart Grid, 2010. **1**(2): p. 168-177.
226. You, S., et al. *A survey on next-generation power grid data architecture*. in *Power & Energy Society General Meeting, 2015 IEEE*. 2015. IEEE.
227. Klemun, M., *Grid Edge: Utility Modernization in the Age of Distributed Generation.* Greentech Media Inc, 2013.
228. Lemaitre, C. and P. Panciatici. *iTesla: Innovative tools for electrical system security within large areas*. in *PES General Meeting| Conference & Exposition, 2014 IEEE*. 2014. IEEE.
229. Hauser, C.H., D.E. Bakken, and A. Bose, *A failure to communicate: next generation communication requirements, technologies, and architecture for the electric power grid.* IEEE Power and Energy Magazine, 2005. **3**(2): p. 47-55.
230. Myrda, P.T. and K. Koellner. *Naspinet-the internet for synchrophasors*. in *System Sciences (HICSS), 2010 43rd Hawaii International Conference on*. 2010. IEEE.

231. Ghatikar, G. and R. Bienert. *Smart grid standards and systems interoperability: a precedent with OpenADR*. in *proceedings of the Grid Interop Forum*. 2011.
232. Gorton, I., et al. *GridOPTICS (TM) A Novel Software Framework for Integrating Power Grid Data Storage, Management and Analysis*. in *System Sciences (HICSS), 2013 46th Hawaii International Conference on*. 2013. IEEE.
233. Kehoe, M., et al., *Smarter cities series: a foundation for understanding IBM smarter cities.* Redguides for Business Leaders, IBM, 2011.
234. Rohjans, S., et al. *Survey of smart grid standardization studies and recommendations*. in *Smart grid communications (SmartGridComm), 2010 first IEEE international conference on*. 2010. IEEE.
235. Bryson, J. and P. Gallagher, *NIST framework and roadmap for smart grid interoperability standards, release 2.0.* National Institute of Standards and Technology (NIST), Tech. Rep. NIST Special Publication 1108R2, 2012: p. 2-0.
236. Photovoltaics, D.G. and E. Storage, *IEEE Guide for Smart Grid Interoperability of Energy Technology and Information Technology Operation with the Electric Power System (EPS), End-Use Applications, and Loads.* 2011.
237. Roadmap, I.S.G.S., *SMB Smart Grid Strategic Group SG3*. 2010, Edition.
238. CEN-CENELEC-ETSI, S.G.C., *Group: Smart grid reference architecture (November 2012).* URI: https://ec. europa. eu/energy/sites/ener/files/documents/xpert_group1_reference_architecture. pdf, 2015.
239. Council, G.A., *GridWise Interoperability Context-Setting Framework.* Smart Grids Interoperability, 2008: p. 1-52.
240. Liu, X. and H. Cao. *A Study of Smart Grid Communication Architecture*. in *Proceedings of International Conference on Computer Science and Information Technology*. 2014. Springer.
241. Grid, N.S., *Introduction to NISTIR 7628 guidelines for smart grid cyber security.* Guideline, Sep, 2010.
242. Sanders, W.H. *TCIPG: Trustworthy cyber infrastructure for the power grid overview*. in *Innovative Smart Grid Technologies (ISGT), 2012 IEEE PES*. 2012. IEEE.
243. You, S., et al. *Data Architecture for the Next-Generation Power Grid: Concept, Framework, and Use Case*. in *Information Science and Control Engineering (ICISCE), 2015 2nd International Conference on*. 2015. IEEE.
244. Liu, H., et al. *The design and implementation of the enterprise level data platform and big data driven applications and analytics*. in *Transmission and Distribution Conference and Exposition (T&D), 2016 IEEE/PES*. 2016. IEEE.

245. Guo, J., et al. *Events associated power system oscillations observation based on distribution-level phasor measurements*. in *T&D Conference and Exposition, 2014 IEEE PES*. 2014. IEEE.
246. Ngamroo, I., et al., *A robust SMES controller design for stabilization of inter-area oscillations based on wide area synchronized phasor measurements.* Electric Power Systems Research, 2009. **79**(12): p. 1738-1749.
247. Tang, K. and G.K. Venayagamoorthy, *Damping inter-area oscillations using virtual generator based power system stabilizer.* Electric Power Systems Research, 2015. **129**: p. 126-141.
248. Liu, H., et al., *ARMAX-Based Transfer Function Model Identification Using Wide-Area Measurement for Adaptive and Coordinated Damping Control.* Smart Grid, IEEE Transactions on, 2015. **PP**(99): p. 1-1.
249. Maslennikov, S., et al. *A test cases library for methods locating the sources of sustained oscillations*. in *Power and Energy Society General Meeting (PESGM), 2016*. 2016. IEEE.
250. Duan, N., et al. *Analysis of power system oscillation frequency using differential Groebner basis and the harmonic balance method*. in *Power & Energy Society General Meeting, 2015 IEEE*. 2015. IEEE.
251. Zhu, Y., B. Wang, and K. Sun. *Damping control for power systems using energy storage*. in *Control And Decision Conference (CCDC), 2017 29th Chinese*. 2017. IEEE.
252. Zhu, Y., et al., *Damping Control for a Target Oscillation Mode Using Battery Energy Storage.* Journal of modern power systems and clean energy, 2018.
253. Slootweg, J. and W. Kling, *The impact of large scale wind power generation on power system oscillations.* Electric Power Systems Research, 2003. **67**(1): p. 9-20.
254. Duan, N. and K. Sun, *Power System Simulation Using the Multistage Adomian Decomposition Method.* IEEE Transactions on Power Systems, 2017. **32**(1): p. 430-441.
255. Duan, N., et al. *Applying reduced generator models in the coarse solver of parareal in time parallel power system simulation*. in *PES Innovative Smart Grid Technologies Conference Europe (ISGT-Europe), 2016 IEEE*. 2016. IEEE.
256. Duan, N. and K. Sun. *Application of the adomian decomposition method for semi-analytic solutions of power system differential algebraic equations*. in *PowerTech, 2015 IEEE Eindhoven*. 2015. IEEE.
257. Duan, N. and K. Sun, *Stochastic Power System Simulation Using the Adomian Decomposition Method.* arXiv preprint arXiv:1710.02415, 2017.
258. Zhang, S., X. Xie, and J. Wu, *WAMS-based detection and early-warning of low-frequency oscillations in large-scale power systems.* Electric Power Systems Research, 2008. **78**(5): p. 897-906.

259. Farrokhifard, M., M. Hatami, and M. Parniani, *Novel approaches for online modal estimation of power systems using PMUs data contaminated with outliers.* Electric Power Systems Research, 2015. **124**: p. 74-84.
260. Chakhchoukh, Y., V. Vittal, and G.T. Heydt, *PMU based state estimation by integrating correlation.* Power Systems, IEEE Transactions on, 2014. **29**(2): p. 617-626.
261. Pierre, J.W., D.J. Trudnowski, and M.K. Donnelly, *Initial results in electromechanical mode identification from ambient data.* Power Systems, IEEE Transactions on, 1997. **12**(3): p. 1245-1251.
262. Kakimoto, N., et al., *Monitoring of interarea oscillation mode by synchronized phasor measurement.* Power Systems, IEEE Transactions on, 2006. **21**(1): p. 260-268.
263. Ning, J., X. Pan, and V. Venkatasubramanian, *Oscillation modal analysis from ambient synchrophasor data using distributed frequency domain optimization.* Power Systems, IEEE Transactions on, 2013. **28**(2): p. 1960-1968.
264. Liu, G. and V.M. Venkatasubramanian. *Oscillation monitoring from ambient PMU measurements by frequency domain decomposition*. in *Circuits and Systems, 2008. ISCAS 2008. IEEE International Symposium on*. 2008. IEEE.
265. Hauer, J.F., C. Demeure, and L. Scharf, *Initial results in Prony analysis of power system response signals.* Power Systems, IEEE Transactions on, 1990. **5**(1): p. 80-89.
266. Ye, Y., R.M. Gardner, and Y. Liu. *Oscillation analysis in western interconnection using distribution-level phasor measurements*. in *Power and Energy Society General Meeting, 2011 IEEE*. 2011. IEEE.
267. Laila, D.S., A.R. Messina, and B.C. Pal, *A refined Hilbert–Huang transform with applications to interarea oscillation monitoring.* Power Systems, IEEE Transactions on, 2009. **24**(2): p. 610-620.
268. Alkan, A. and A.S. Yilmaz, *Frequency domain analysis of power system transients using Welch and Yule–Walker AR methods.* Energy conversion and management, 2007. **48**(7): p. 2129-2135.
269. Papy, J.-M., L. De Lathauwer, and S. Van Huffel, *Common pole estimation in multi-channel exponential data modeling.* Signal Processing, 2006. **86**(4): p. 846-858.
270. Messina, A.R., et al., *Nonstationary approaches to trend identification and denoising of measured power system oscillations.* Power Systems, IEEE Transactions on, 2009. **24**(4): p. 1798-1807.
271. Yang, D., et al., *Identification of dominant oscillation mode using complex singular value decomposition method.* Electric Power Systems Research, 2012. **83**(1): p. 227-236.

272. Hamdan, A., *An investigation of the significance of singular value decomposition in power system dynamics.* International Journal of Electrical Power & Energy Systems, 1999. **21**(6): p. 417-424.
273. Thambirajah, J., N.F. Thornhill, and B.C. Pal, *A multivariate approach towards interarea oscillation damping estimation under ambient conditions via independent component analysis and random decrement.* Power Systems, IEEE Transactions on, 2011. **26**(1): p. 315-322.
274. Zhou, N., J. Pierre, and R. Wies. *Estimation of low-frequency electromechanical modes of power systems from ambient measurements using a subspace method*. in *Proceedings of the North American Power Symposium*. 2003. sn.
275. De Moor, B. and P. Van Overschee, *Numerical algorithms for subspace state space system identification*, in *Trends in Control*. 1995, Springer. p. 385-422.
276. Wies, R.W., J.W. Pierre, and D.J. Trudnowski, *Use of ARMA block processing for estimating stationary low-frequency electromechanical modes of power systems.* Power Systems, IEEE Transactions on, 2003. **18**(1): p. 167-173.
277. Zhou, N., et al., *Robust RLS methods for online estimation of power system electromechanical modes.* Power Systems, IEEE Transactions on, 2007. **22**(3): p. 1240-1249.
278. Zhou, N., et al., *Electromechanical mode online estimation using regularized robust RLS methods.* Power Systems, IEEE Transactions on, 2008. **23**(4): p. 1670-1680.
279. Larsson, M. and D.S. Laila. *Monitoring of inter-area oscillations under ambient conditions using subspace identification*. in *Power & Energy Society General Meeting, 2009. PES'09. IEEE*. 2009. IEEE.
280. Robertson, D.C., et al., *Wavelets and electromagnetic power system transients.* Power Delivery, IEEE Transactions on, 1996. **11**(2): p. 1050-1058.
281. Zhou, N., et al. *An algorithm for removing trends from power-system oscillation data*. in *Power and Energy Society General Meeting-Conversion and Delivery of Electrical Energy in the 21st Century, 2008 IEEE*. 2008. IEEE.
282. Dosiek, L., et al., *Mode shape estimation algorithms under ambient conditions: A comparative review.* Power Systems, IEEE Transactions on, 2013. **28**(2): p. 779-787.
283. Ju, W., B. Wang, and K. Sun, *Can Nonlinear Electromechanical Oscillation be Analyzed Using an Equivalent SMIB System?*
284. Liu, H., et al. *Comparison of MIMO system identification methods for electromechanical oscillation damping estimation*. in *Power and Energy Society General Meeting (PESGM), 2016*. 2016. IEEE.

285. Trudnowski, D., J. Johnson, and J. Hauer, *Making Prony analysis more accurate using multiple signals.* Power Systems, IEEE Transactions on, 1999. **14**(1): p. 226-231.
286. Crow, M. and A. Singh, *The matrix pencil for power system modal extraction.* Power Systems, IEEE Transactions on, 2005. **20**(1): p. 501-502.
287. Nezam Sarmadi, S. and V. Venkatasubramanian, *Electromechanical mode estimation using recursive adaptive stochastic subspace identification.* Power Systems, IEEE Transactions on, 2014. **29**(1): p. 349-358.
288. Lee, K. and K. Poon, *Analysis of power system dynamic oscillations with heat phenomenon by Fourier transformation.* Power Systems, IEEE Transactions on, 1990. **5**(1): p. 148-153.
289. Rueda, J.L., C. Juárez, and I. Erlich, *Wavelet-based analysis of power system low-frequency electromechanical oscillations.* Power Systems, IEEE Transactions on, 2011. **26**(3): p. 1733-1743.
290. Han, S., Z. Xu, and C. Wu, *Mode shape estimation and mode checking for IAO using correlation analysis technique.* Electric Power Systems Research, 2011. **81**(6): p. 1181-1187.
291. Zhang, P., et al., *Synchronized measurement based estimation of inter-area electromechanical modes using the Ibrahim time domain method.* Electric Power Systems Research, 2014. **111**: p. 85-95.
292. Shukla, S., S. Mishra, and B. Singh, *Empirical-mode decomposition with Hilbert transform for power-quality assessment.* Power Delivery, IEEE Transactions on, 2009. **24**(4): p. 2159-2165.
293. Wu, M.-C. and N.E. Huang, *Biomedical data processing using HHT: A review*, in *Advanced Biosignal Processing*. 2009, Springer. p. 335-352.
294. Lei, Y., et al., *A review on empirical mode decomposition in fault diagnosis of rotating machinery.* Mechanical Systems and Signal Processing, 2013. **35**(1): p. 108-126.
295. Huang, N.E. and Z. Wu, *A review on Hilbert‐Huang transform: Method and its applications to geophysical studies.* Reviews of Geophysics, 2008. **46**(2).
296. Huang, N.E., et al. *The empirical mode decomposition and the Hilbert spectrum for nonlinear and non-stationary time series analysis*. in *Proceedings of the Royal Society of London A: Mathematical, Physical and Engineering Sciences*. 1998. The Royal Society.
297. Messina, A. and V. Vittal, *Extraction of dynamic patterns from wide-area measurements using empirical orthogonal functions.* Power Systems, IEEE Transactions on, 2007. **22**(2): p. 682-692.
298. Rilling, G., et al., *Bivariate empirical mode decomposition.* Signal Processing Letters, IEEE, 2007. **14**(12): p. 936-939.
299. Rehman, N.U. and D.P. Mandic, *Empirical mode decomposition for trivariate signals.* Signal Processing, IEEE Transactions on, 2010. **58**(3): p. 1059-1068.

300. Yang, W., et al., *Bivariate empirical mode decomposition and its contribution to wind turbine condition monitoring.* Journal of Sound and Vibration, 2011. **330**(15): p. 3766-3782.
301. Molla, M.K., et al. *Separation of EOG artifacts from EEG signals using bivariate EMD*. in *Acoustics Speech and Signal Processing (ICASSP), 2010 IEEE International Conference on*. 2010. IEEE.
302. Rehman, N. and D.P. Mandic. *Multivariate empirical mode decomposition*. in *Proceedings of The Royal Society of London A: Mathematical, Physical and Engineering Sciences*. 2009. The Royal Society.
303. Mutlu, A.Y. and S. Aviyente, *Multivariate empirical mode decomposition for quantifying multivariate phase synchronization.* EURASIP Journal on Advances in Signal Processing, 2011. **2011**: p. 7.
304. Fleureau, J., et al., *Multivariate empirical mode decomposition and application to multichannel filtering.* Signal Processing, 2011. **91**(12): p. 2783-2792.
305. Wang, Y.-H., et al., *On the computational complexity of the empirical mode decomposition algorithm.* Physica A: Statistical Mechanics and its Applications, 2014. **400**: p. 159-167.
306. *FNET/GridEye Web Display.* http://fnetpublic.utk.edu/.
307. Hiyama, T., N. Suzuki, and T. Funakoshi. *On-line identification of power system oscillation modes by using real time FFT*. in *Power Engineering Society Winter Meeting, 2000. IEEE*. 2000. IEEE.
308. Guo, J., et al. *Real-time Power System Electromechanical Mode Estimation Implementation and Visualization Utilizing Synchrophasor Data*. in *2016 IEEE PES Transmission and Distribution Conference and Exposition*. 2016. IEEE.
309. Quintero, J., G. Liu, and V.M. Venkatasubramanian. *An oscillation monitoring system for real-time detection of small-signal instability in large electric power systems*. in *Power Engineering Society General Meeting, 2007. IEEE*. 2007. IEEE.
310. Van de Vyver, J., et al., *Droop control as an alternative inertial response strategy for the synthetic inertia on wind turbines.* IEEE Transactions on Power Systems, 2016. **31**(2): p. 1129-1138.
311. Miao, Z., et al., *Control of DFIG-based wind generation to improve interarea oscillation damping.* IEEE Transactions on Energy Conversion, 2009. **24**(2): p. 415-422.

APPENDICES

Appendix A: Oscillation mode identification based on multivariate empirical mode decomposition

A.1. Introduction

Power system oscillation is a common phenomenon in interconnected power grids. Insufficient damping of inter-area oscillation may increase system risks and even cause failures [245]. Therefore, fast detection and analysis on inter-area oscillations are critical to activate proper oscillation damping controls to increase system reliability [99, 114, 246-252]. Moreover, as the conditions of modern power girds vary more constantly and significantly with the increase of renewables, energy storage and other distributed resources, updating the oscillation information is becoming more important but also challenging [253].

Approaches to analyze the oscillation modes of power grids fall into two categories: model-based methods and measurement-based methods. Model-based methods analyze system oscillation based on detailed system dynamic models using eigenvalue analysis approaches. It is becoming difficult for system operators to use model-based approaches due to many factors, such as the computation burden of large-scale dynamic simulations, changing environments, information privacy issues and parameter inaccuracy (e.g. inadequate modeling of loads) [226, 254-257]. Applying synchrophasor measurement technology, Wide-Area Measurement Systems (WAMSs) provide a powerful tool to monitor and analyze the dynamics of interconnected power grids [72, 258, 259]. Since large disturbances are rare and usually destructive in modern power grids, system event data are far from enough for real-time estimation of system oscillation modes. It is necessary to provide oscillation information to system operators under normal operation conditions. Studies on ambient synchrophasor measurements show that there is a constant level of noise caused by load

variations or other environmental disturbances at the transmission level [260] and the distribution level [72]. These ambient sychronphasor measurements have been recently used as a data source to extract real-time inter-area oscillation information.

Since ambient measurements were first used in Ref. [261] to analyze the electromechanical oscillation, multiple approaches have been developed based on various signal processing techniques. There are two main categories of methods for oscillation analysis based on ambient and event data: transfer function based methods and subspace methods. Transfer-function-based methods directly estimate mode shape through treating measurements as system outputs. Typical transfer function based methods include Fourier transform [262-264], the Prony's method [265], the Matrix-Pencil method [266], Empirical Mode Decomposition (EMD) [267], the Yule-Walker method [268], the Total Least Squares method [269], wavelet analysis [270], and the singular value decomposition method [271, 272], etc. To increase analysis efficiency, Ref. [263] adopted a FFT-based distributed optimization method to select the dominant measurement channels for estimating each oscillation mode based on ambient data. Ref. [273] proposed a two-step method which comprised of independent component analysis and random decrement to estimate the oscillation mode. Different from transfer-function-based methods, subspace methods obtain the oscillation mode information through identifying the system state space model using the measurements [261]. Typical subspace methods include the Canonical Variate Algorithm [274], the N4SID algorithm [275], and the autoregressive moving average block-processing method [276]. Recently, Ref. [277] proposed the robust recursive least square algorithm to analyze measurement data. Ref. [278] improved this method by proposing a regularized robust recursive least square method.

Existing transfer function based methods have limitations in one or two of the following aspects. *a) The capability to analyze drifting, non-stationary signals and provide localized results.* Oscillation may drift frequently in ambient measurements [279]. For example, a high damping local oscillation mode may stimulate an inter-area oscillation mode with a pseudo negative damping ratio within a short duration. Existing methods may not be able to find the appropriate time window for analyzing this inter-area oscillation due to this drifting [280]. In addition, some measurements are mixed with fluctuations unrelated to oscillations, such as the frequency fluctuations caused by normal system operation and regulations [281]. These non-stationary measurements usually lead to difficulties to accurately analyze the subtle oscillation modes [282, 283]. For example, the Prony's method requires the signal to be zero-mean and stationary, which may result to difficulties to analyze signals with high amplitude trends [276]. *b) The capability to analyze multi-channel signals.* Most existing methods can only process one signal so they must analyze multiple signals in a separate way [284]. they usually require measurements from critical devices, which has good observability (e.g., branch flow and bus frequency) on certain inter-area oscillation modes [258, 261, 267, 271, 276-278, 282, 285-291]. If the measurement that has good oscillation observability is not available in some areas, single-channel methods may not be able to provide oscillation information in these areas. Therefore, there is a need of developing multi-channel methodology to extract oscillation information utilizing high-noise measurements, which individually have less observability on oscillation.

The aim of this study is to introduce multi-channel EMD based methods: Bivariate EMD (BEMD), Trivariate EMD (TEMD), and Multivariate EMD (MEMD), to facilitate identifying inter-area oscillation mode using multi-channel ambient synchrophasor measurements. Particularly, MEMD is investigated in details

using real-world ambient measurements. The test results show that MEMD has better performance than typical oscillation identification methods. For convenience, wide-area frequency measurements are adopted for illustration and analysis in the following sections. The introduced methods and descriptions are also applicable to other wide-area measurement data such as instantaneous real power, voltage angle, and current [108, 109].

The rest of this chapter is organized as follows. Section A.2 describes the original form of the EMD method. Section A.3 expands it to bivariate, trivariate, and multivariate empirical mode decomposition to identify oscillation. Section A.4 presents two test cases to verify the proposed methods. Conclusions are provided in Section A.5.

A.2. Background — empirical mode decomposition based oscillation identification

EMD was developed for analyzing non-stationary signals that commonly exist in many science and engineering fields [1]. Due to its data-driven nature and the strong capability in analyzing non-stationary signals to provide information on localized amplitudes and frequencies, EMD has been proved to be effective for time-frequency analysis in various areas, such as power quality assessment [292], biomedical signals [293], mechanical signals [294], and geographical signals [295]. For oscillation identification, EMD has been applied to analyze transient measurements [267].

In EMD-based oscillation identification, a frequency measurement signal can be viewed as a linear combination of short-term frequency fluctuation components and long-term frequency trends [296]. Short-term frequency fluctuations are defined as the evolution feature of frequency measurements $f(t)$ between local

frequency maxima and minima. Subtracting this fast fluctuation component, which is denoted by $\tilde{f}_1(t)$, from $f(t)$, one can identify the "slower" frequency trend $\bar{\bar{f}}_1(t)$ that supports the short-term frequency fluctuation component, so that

$$f(t) = \bar{\bar{f}}_1(t) + \tilde{f}_1(t) \quad \text{(A.1)}$$

where $\tilde{f}_1(t)$ is termed an intrinsic mode function (IMF). As raw measurements have noises or measurement errors, $\tilde{f}_1(t)$ represents these high-frequency elements. $\bar{\bar{f}}_1(t)$ is still oscillatory after subtracting the fast fluctuation component $\tilde{f}_1(t)$ from $f(t)$. The same decomposition method can be applied to $\bar{\bar{f}}_1(t)$ as $\bar{\bar{f}}_1(t) = \bar{\bar{f}}_2(t) + \tilde{f}_2(t)$. After recursive decompositions, the representation of the original frequency measurement $f(t)$ becomes

$$f(t) = \bar{\bar{f}}_M(t) + \sum_{m=1}^{M} \tilde{f}_m(t) \quad \text{(A.2)}$$

where $\tilde{f}_m(t)$ is the *m*th IMF of frequency measurements and $\bar{\bar{f}}_M(t)$ is the residual frequency. Each iterative step for decomposing the frequency signal into one IMF has the iterative procedures as shown in Table A.1 [2].

In Step 5), the IMF criterion to stop the sifting process for generating one IMF is that the normalized square deviation of two consecutive sifted signals is smaller than a threshold.

$$\sum_{t=1}^{T} \left[\frac{\left| \tilde{f}_{m,l+1} - \tilde{f}_{m,l} \right|^2}{\tilde{f}_{m,l}^{\,2}} \right] \leq \bar{D}_{\text{EMD}} \quad \text{(A.3)}$$

where *l* and *l*+1 denote two successive sifting operations. The typical value of $\bar{D}$ is between 0.2 and 0.3 [296]. The stopping criterion for the outer iterative loop (decomposing IMFs) is that the residue $\bar{\bar{f}}_K(t)$ becomes a monotonic signal, from which no more IMFs can be extracted.

Since the original EMD can only process the real-value (univariate) time series signal, existing work on oscillation identification are limited to applying classical

EMD or Ensemble EMD (EEMD, a modified version of EMD) on simulation data or transient measurements [267, 297]. As described in Section A.1, ambient measurements may contain valuable information such as common oscillation components that reflect inter-area oscillation modes. This information may be difficult to extract using univariate EMD due to low signal/noise ratio environments.

A.3. Methodology — multivariate empirical mode decomposition based ambient oscillation mode identification

A.3.1. bivariate/trivariate empirical mode decomposition for oscillation identification

The bivariate (complex) EMD (BEMD) [298] and the trivariate EMD (TEMD) [299] enhanced the capability of identifying synchronous behaviors of bivariate and trivariate signals. In many fields, BEMD and TEMD has been proved to be able to determine common frequency components through simultaneous decomposition of two or three signals, such as equipment condition monitoring [300] and biomedical signal analysis [301]. Since inter-area oscillations typically happen in two or three areas, if the measurements from two or three areas are available, it is possible to apply BEMD and TEMD to multiple channels of frequency ambient measurements to improve oscillation identification. Based on their basic algorithm formulation [298, 299], the iterative procedures to extract each oscillation component based on BEMD and TEMD are developed in Table A.2 and Table A.3, respectively.

The IMF criterion to stop the IMF sifting are extensions of (A.3) to multiple signals. For example, the IMF criterion for the TEMD case is shown in (A.4).

$$\frac{1}{3}\sum_{A,B,C}\sum_{t=1}^{T}\left[\frac{\left|\tilde{f}_{m,l+1}-\tilde{f}_{m,l}\right|^2}{\tilde{f}_{m,l}^{\,2}}\right] \leq \overline{D}_{\mathrm{TEMD}} \tag{A.4}$$

The criterion to stop decomposing the next IMF is that all residual signal projections have less than two extrema (for BEMD) or three extrema (for TEMD).

A.3.2. Multivariate Empirical Mode Decomposition for Oscillation Identification

Multivariate EMD (MEMD) was developed for analyzing complex, nonlinear, and dynamic signals [302]. The simultaneous analysis of multi-channel signals using MEMD has been proved to be capable to analyze multichannel signals in a synchronized approach [303]. This synchronized approach helps to identify the oscillation modes that exists in multiple channels with low amplitudes, which may be neglected in mono-channel analysis [304]. This feature makes MEMD a competitive candidate method for oscillation mode identification based on wide-area ambient measurements.

The essence of EMD-based methods is based on local maxima and minima information, but local extrema definition are not obvious for multiple-channel frequency signals [302]. Therefore, the main difficulty of extending EMD to MEMD for frequency analysis is to generate the frequency envelops based on local extrema. Assuming $\{\boldsymbol{f}_N(t)\}_{t=1}^{T} = \{f_1(t), f_2(t), \dots, f_N(t)\}$, the main steps of applying MEMD [302] for oscillation mode identification are described in Table A.4.

The IMF criterion in Step 6) to stop the sifting iteration is shown in (A.5).

$$\frac{1}{N}\sum_{n=1}^{N}\sum_{t=1}^{T}\left[\frac{\left|\tilde{f}_{m,l+1}-\tilde{f}_{m,l}\right|^2}{\tilde{f}_{m,l}^{\,2}}\right] \le \overline{D}_{\mathrm{MEMD}} \qquad \text{(A.5)}$$

The outer iteration loop for generating the next IMF terminates when signal projections $p^{\theta_k}(t)\}_{k=1}^{K}$ have less than three extrema.

Using MEMD, multi-channel ambient frequency measurements are analyzed as an *n* dimensional matrix and decomposed into several IMFs components based

on the iterative process in Table A.4. Each IMF contains the localized frequency, amplitude, and phase angle information for each frequency signal and oscillation mode. Dominant oscillation modes can be identified based on the energy of each IMF given by

$$E_{k,\infty} = \sum_{t=1}^{T} \sum_{n=1}^{N} \left[\tilde{f}_k(t)[n]\right]^2 \quad \text{(A.6)}$$

In some situations, the measurements may have high-magnitude trends that are extracted as high-energy IMFs. These high magnitude trends can be easily excluded from inter-area oscillations as the IMF for all signals have very close phase angles. Additionally, it is also easy to distinguish these IMFs from their frequencies, which are usually lower than typical interarea oscillation frequencies.

Through the Hilbert Transform [296], the localized frequency and amplitude values for each IMF and each signal can be obtained as

$$f_H(t) = \frac{P}{\pi} \int_{-\infty}^{+\infty} \frac{f(\tau)}{t-\tau} d\tau \quad \text{(A.7)}$$

$$z(t) = f(t) + i f_H(t) = a(t) e^{i\varphi(t)} \quad \text{(A.8)}$$

where $a(t)$ is the localized amplitude obtained by $a(t) = \left[f^2(t) + {f_H}^2(t)\right]^{1/2}$. $\varphi(t)$ is the localized angle calculated by $\varphi(t) = \arcsin(f_H(t)/a(t))$. The instantaneous frequency for all IMFs and signals can be obtained as $\omega(t) = d\varphi(t)/dt$. The joint instantaneous frequency and amplitude of one IMF denote the frequency and amplitude for an oscillation mode considering all signals at the system level, and they are obtained by

$$f_{\mathrm{IMF},l}(t) = \frac{\sum_{n=1}^{N} \left(a_{\mathrm{IMF},l,n}(t) \cdot f_{\mathrm{IMF},l,n}(t)\right)}{\sum_{n=1}^{N} a_{\mathrm{IMF},l,n}(t)} \quad \text{(A.9)}$$

$$a_{\mathrm{IMF},l}(t) = 1/N \cdot \sum_{n=1}^{N} a_{\mathrm{IMF},l,n}(t) \quad \text{(A.10)}$$

The joint instantaneous frequency and amplitude for each IMF can be graphed for visualization in the time domain. This information can help operators

understand real-time oscillation information, as well as resonance-stimulated oscillations based on the oscillation occurrence sequence. In addition, the computational complexity of EMD-based algorithms are proved to be equivalent to Fast Fourier Transform (FFT) [305], indicating MEMD is suitable for online oscillation identification.

A.4. Case studies based on FNET/GridEye measurements

This section shows two cases to investigate the features of TEMD and MEMD for oscillation identification based on FNET/GridEye ambient measurements. As a WAMS at the distribution level, the FNET/GridEye system is capable of monitoring the power grid with high dynamic accuracy [198, 306]. A frequency disturbance recorder (FDR) can measure power grid voltage, angle, and frequency at the 120V outlets. These highly accurate synchrophasor measurements at transmitted across the Internet at a 10Hz report rate (i.e. 10 frequency samples per second) and collected by the main server located at the University of Tennessee. Table A.5 shows the description on the three cases using FNET/GridEye ambient measurements.

A.4.1. Case 1: The NPCC system

A simulation model is built based on the Northeast Power Coordinating Council (NPCC) system in the U.S. Eastern Interconnection. With its interfaces represented by generators, this model has 48 generators and 206 branches. Figure A.1 shows the diagram of the reduced NPCC system. This system has been tuned to have both local and inter-area oscillation modes.

A generation trip event was simulated at Bus 115. The frequency measurements of 11 selected buses are obtained from PSS/E simulation and plotted in Figure A.2. It shows that some local oscillation modes are mixed with the inter-area

oscillation modes in frequency measurements, for example the local oscillation reflected in Bus 134's frequency.

Figure A.3 shows IMF 1 to IMF 6 obtained by MEMD. In Figure A.3, three oscillation modes can be identified: a local oscillation mode shown in IMF 2 and two inter-area oscillation modes shown in IMF3 and IMF4. The local oscillation mode in IMF 2 and the inter-area oscillation mode in IMF3 have light damping.

Since these frequency measurements are non-stationary signals, the Prony's method is not capable for oscillation mode analysis. To facilitate comparison, the classical EMD method was applied to the same measurements. Figure A.4 and Figure A.5 show the EMD results based on measurements from Bus 60 and Bus 68. It can be noted that the number of IMFs of the two measurements given by EMD is different: EMD gives five IMFs for the Bus 60 frequency measurement and three IMFs for the Bus 68 frequency measurements. In addition, the phase information of the oscillation is separated in the different EMD results. These shortcomings make EMD inaccurate and even incapable to identify oscillation. On the contrary, in MEMD, the frequency measurements from all buses are decomposed into the same number of IMFs. Moreover, MEMD can detect the common oscillation modes and preserve the phase information. Also, MEMD has higher computational efficiency than EMD due to the simultaneous decomposition of multiple signals.

To test the sensitivity of MEMD to time window sizes, Figure A.6 shows the IMFs given by MEMD on the first half of the original time window. It can be seen that a shorter time window will produce consistent IMFs with those in Figure A.3. This time frequency analysis capability also indicates that MEMD is suitable for online applications.

MEMD was also compared with the Fast Fourier Transform (FFT) using the same measurements. Figure A.7 shows the FFT spectrum of the raw frequency measurements. Figure A.8 shows the joint instantaneous frequency and magnitude of IMF2-5 given by MEMD. It can be seen that the FFT result does not preserve localized frequency, magnitude, and phase angle, as well as damping information. On the contrary, MEMD can easily identify the oscillation and preserve the localized oscillation frequency, amplitude, and phase information for each oscillation mode.

A.4.2. Case 2: European Ambient Frequency Measurements

The first case uses three channels of ambient frequency measurements at three locations in the European power grid as shown in Figure A.9. Applying TEMD to the measurements, Figure A.10 to Figure A.12 show the IMFs in the TEMD results. IMF 1 and IMF 2 show the high frequency components that are caused by measurement errors and noises. IMF 3 represents a 1.0 Hz local oscillation mode in the Turkey power grid. IMF 4 and IMF 7 have small amplitudes and don't show dominant oscillations' information. IMF 8 and IMF 9 contain high magnitudes of variations, reflecting long-term frequency fluctuations resulting from governor responses and automatic generation control. Based on the energy function (6) and IMF amplitudes, IMF 5 and IMF 6 can be as identified dominant inter-area oscillation modes, whose frequencies are 0.30 Hz and 0.15 Hz, respectively. The observed damping ratio of the two oscillation modes vary with time (some even have negative damping) because of constant small disturbances occurred in the ambient environments. Figure A.13 shows the joint instantaneous frequency based on Hilbert spectral analysis.

As a comparison, Figure A.14 shows IMF 4 to IMIF 6 using the classic EMD method. It can be seen that the two inter-area oscillation modes are mixed up with each other in IMF 4, thus unable to be identified using EMD. From this

comparison, it can be noticed that if the measurements in one area has high noises, MEMD could extract possible oscillation information from the noisy signals in this area aided by oscillation information from other areas.

A.4.3. Case 3: EI Ambient and Event Frequency Measurements

The second case analyzes ambient measurements and the measurements of a generation trip event in the U.S. Eastern Interconnection (EI) system. This case aims to verify that the oscillation mode identified using the ambient data can be observed in event transients. Frequency measurements from 12 locations around the event occurrence time are shown in Figure A.15. The studied time window is 5 minutes, during which the generation trip event happened at 125s.

Figure A.16 to Figure A.18 show the MEMD decomposition result using the frequency measurements. Among the obtained IMFs, IMF 1 to IMF 4 shows the high-frequency components caused by local system noises, measurement errors, and local oscillations with high damping ratios. Observed from its frequency and amplitude, IMF 5 might contain useful information of inter-area oscillation. IMF 6 to IMF 9 are the frequency trends that features constant relative phase angles for all measurements. Figure A.19 shows the joint instantaneous frequency based on Hilbert spectral analysis. To identify the dominant oscillation mode, Figure A.20 shows the energy distribution of IMF1 to IMF 5, which have oscillatory phases among all IMFs. It can be seen that IMF 5 has the largest oscillation energy compared with other IMFs, indicating it is the dominant oscillation mode. Figure A.21 shows that MEMD can discover the dominant oscillation mode from both ambient and event measurements.

To further analyze these two oscillation components, Figure A.22 present the frequency and the mode compass graphs of the two oscillations. It shows that

the two oscillations in ambient and event, both of which can be identified by MEMD, actually belong to the same inter-area oscillation mode.

For comparison, three typical methods: the modified Yule Walker method, the Prony's method, and the Fast Fourier Transform (FFT) method are tested using the same measurements. Table A.6 shows their results, as well as a comparison on their advantages and disadvantages. As an example, the single-sided amplitude spectrum of the raw frequency measurement obtained by FFT is presented in Figure A.23, which displays a crest near 0.2 Hz indicating this oscillation mode. However, FFT does not preserve localized frequency, magnitude, as well as phase angle information over the studied time window.

A.5. Conclusions

This chapter introduced BEMD, TEMD, and MEMD as multi-channel data-drive approaches for inter-area oscillation identification based on wide-area synchronous measurements. The proposed method has the capability to identify inter-area oscillation modes using highly noisy ambient measurements. Moreover, it is robust to drifting and non-stationary measurement signals. Test results based on simulation results and real-world frequency measurements, as well as comparison with existing methods show that the proposed methods have good potential for real-time monitoring and identification of inter-area oscillation modes.

When the measurement in one area is totally unavailable, the oscillation mode information of that area, such as the oscillation amplitude and phase angle, could not be re-constructed using MEMD as it is a measurement-based approach. Future work could be model-measurement hybrid oscillation identification method

development and the optimal measurements selection for MEMD analysis in large power systems.

A.6. Tables and figures

Table A.1. Iteration steps of univariate EMD to generate each IMF

Step	Procedure
1)	Find all frequency extrema of $f(t)$, which are denoted by $\bar{f}_i$ (maxima) and $\underline{f_i}$ (minima).
2)	Construct two time-series frequency signals from maxima $\bar{f}_i$ and minima $\underline{f_i}$, respectively, through cubic-spline interpolation. The two constructed frequency signals $\bar{\bar{f}}_{max}$ and $\bar{\bar{f}}_{min}$ form an envelope.
3)	Computing the mean of the envelop: $\bar{\bar{f}}(t) = \left(\bar{\bar{f}}_{max} + \bar{\bar{f}}_{min}\right)/2$.
4)	Subtracting the envelop mean to obtain a fast fluctuation components $\tilde{f}(t) = f(t) - \bar{\bar{f}}(t)$.
5)	Continue to sift $\tilde{f}(t)$ using Step 1) to 4) until it meets the IMF criterion. Afterwards, get the residue $f(t) - \tilde{f}(t)$ and return to Step 1) to decompose the next IMF.

Table A.2. Iterative procedures of BEMD for generating each IMF

Step	Procedure
1)	Use two frequency measurements f_A and f_B in area A and B to construct the complex frequency measurement vector $\boldsymbol{f}_{\mathrm{A-B}} = f_{\mathrm{A}} + i * f_{\mathrm{B}}$.
2)	Construct *N* directions for projection of the frequency vector. These directions are denoted by $\varphi_k = 2k\pi/N$, $1 \le k \le N$.
3)	Project the complex frequency measurement vector $\boldsymbol{f}_{\mathrm{A-B}}$ on direction φ_k: $P_{\varphi_k}(t) = \mathrm{Re}\left(e^{-i\varphi_k} x(t)\right)$.
4)	Extract the time of the maxima in $P_{\varphi_k}(t)$. The time instants at maxima are denoted by $\{t_j^k\}$.
5)	Conduct cubic-spline interpolation based on the point set $\left[t_j^k, \boldsymbol{f}_{\mathrm{A-B}}(t_j^k)\right]$ to get the complex frequency envelope curve in the direction φ_k, which is denoted by $\boldsymbol{e}_{\varphi_k}$. Update the direction index from *k* to *k*+1. If *k*<*K*, return to Step 3). Otherwise, continue the next step.
6)	Calculate the complex frequency envelop mean: $\bar{\bar{\boldsymbol{f}}}(t) = 2/N \cdot \sum_k \boldsymbol{e}_{\varphi_k}(t)$.
7)	Subtract $\bar{\bar{\boldsymbol{f}}}(t)$ from the complex frequency measurement vector $\boldsymbol{f}_{A-B}$, so that $\tilde{\boldsymbol{f}}(t) = \boldsymbol{f}_{\mathrm{A-B}}(t) - \bar{\bar{\boldsymbol{f}}}(t)$.
8)	Continue to sift $\tilde{\boldsymbol{f}}(t)$ using Step 1) to 7) until it meets the IMF criterion. Afterwards, get the residue $\boldsymbol{f}_{\mathrm{A-B}}(t) - \tilde{\boldsymbol{f}}(t)$ and return to step 1 to decompose the next IMF.

Table A.3. Iterative procedures of TEMD for generating each IMF

Step	Procedure
1)	Using three frequency measurements f_{A}, f_{B}, and f_{C} from three areas, construct the trivairate quaternion frequency signal denoted by $\boldsymbol{f}(t)$.
2)	Calculate the projection of $\boldsymbol{f}(t)$, i.e., $p_{\theta_k}^{\varphi_n}$, where $\theta_k = k\pi/K$ and $\varphi_n = n\pi/N$, where $k = 1, \dots, K \; and \; n = 1, \dots, N$.
3)	Extract the locations $\{(t_k^n)_i\}$ of the maxima of $p_{\theta_k}^{\varphi_n}(t)$ for eac1h k and n.
4)	Conduct cubic-spline interpolation on the extrema point set $[(t_k^n)_i, \boldsymbol{f}(t_k^n)_i]$ to get the frequency envelope curve in the direction $\{\theta_k, \varphi_n\}$, which is denoted by $\boldsymbol{e}_{\theta_k}^{\varphi_n}$ for each k and n.
5)	Calculate the complex frequency envelop mean: $\bar{\bar{\boldsymbol{f}}}(t) = \frac{1}{KN} \cdot \sum_k \sum_n \boldsymbol{e}_{\theta_k}^{\varphi_n}$.
6)	Subtract $\bar{\bar{\boldsymbol{f}}}(t)$ so that $\tilde{\boldsymbol{f}}(t) = \boldsymbol{f}(t) - \bar{\bar{\boldsymbol{f}}}(t)$.
7)	Continue to sift $\tilde{\boldsymbol{f}}(t)$ using Step 1) to 6) until it meets the IMF criterion. Afterwards, return to Step 1) to decompose the next IMF.

Table A.4. Iterative procedures of MEMD for generating each IMF

Step	Procedure
1)	Generate a set of angles $\theta^k\}_{k=1}^K$ on a sphere that has (n−1) dimensions to denote K projection directions. Create the direction vectors denoted by $X^{\theta_k}\}_{k=1}^K$ based on these angles.
2)	Project the frequency measurements $\boldsymbol{f}_N(t)$ for all K directions. The projections are denoted by $p^{\theta_k}(t)\}_{k=1}^K$.
3)	Find the maxima of the projections. Give $\left\{t_i^{\theta_k}\right\}$ as the time instants at the maxima of projections $p^{\theta_k}(t)\}_{k=1}^K$.
4)	Use maxima $\left[t_i^{\theta_k}, \boldsymbol{f}\left(t_i^{\theta_k}\right)\right]$ and cubic-spline interpolation to obtain the envelop curve in each direction. The envelop curves for all K directions are denoted by $\boldsymbol{e}^{\theta_k}\}_{k=1}^K$.
5)	Calculate the envelop mean $\bar{\bar{\boldsymbol{f}}}(t) = \frac{1}{K}\sum_{k=1}^K \boldsymbol{e}^{\theta_k}(t)$. Subtract $\bar{\bar{\boldsymbol{f}}}(t)$ so that $\tilde{\boldsymbol{f}}(t) = \boldsymbol{f}(t) - \bar{\bar{\boldsymbol{f}}}(t)$.
6)	Continue to sift $\tilde{\boldsymbol{f}}(t)$ using Step 1) to 5) until it meets the IMF criterion. Afterwards, return to Step 1) to decompose the next IMF.

Table A.5. Information on the study cases

Case #	Model/Measurement information	Test purpose
1	The NPCC model	Test the capability of MEMD in identifying oscillation modes using simulation data
2	FNET/GirdEye ambient frequency measurements in Europe	a) Test the capability of TEMD in identifying oscillation modes based on ambient measurements b) Compare TEMD with classical EMD
3	FNET/GirdEye ambient and event measurements in U.S. Eastern Interconnection	a) Test the capability of MEMD in identifying oscillation modes using high-noisy ambient data b) Test the capability of MEMD in analyzing non-stationary frequency measurements during events c) Verify the consistency of identified oscillation modes using ambient and event measurements d) Compare MEMD with typical methods

Table A.6. Method comparison based on EI frequency measurements

Methods	Oscillation frequency	Advantage(s)	Disadvantage(s)
MEMD	Ambient: 0.20 Hz Event: 0.19 HZ	a) Capable of analyzing non-stationary signals; b) Provide localized frequency and amplitude; c) Multiple signal analysis capability; d) Preserve phase information; etc.	a) As a data-driven method, it needs more theoretical research.[303]
Fast Fourier Transform [307]	Ambient: 0.20 Hz Event: 0.19 HZ	a) Computationally efficient; b) Accurate frequency domain results; c) Capable of analyzing non-stationary signals.	a) Lost information on localized frequency, amplitude, and phase when analyzing non-stationary signals
The modified Yule Walker method [268, 276, 308]	Ambient: 0.21 Hz Event: 0.20 HZ	a) Capable of analyzing non-stationary signals; b) As a parametric method, it has complete theoretical support.	a) Need pre-processing, such as de-trending; b) Lost localized frequency and phase information.
The Prony's method [309]	N/A (due to non-stationary and noisy signals)	a) Computationally efficient; b) As a parametric method, it has complete theoretical support.	a) Require the signal to be stationary.

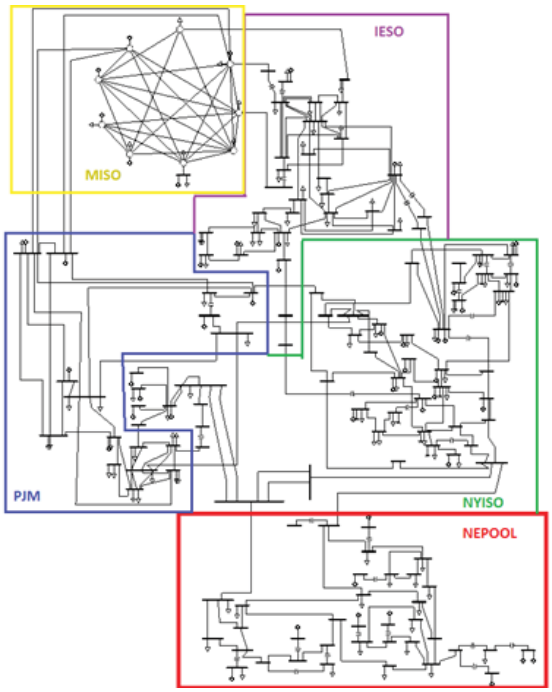

Figure A.1. The reduced NPCC system diagram

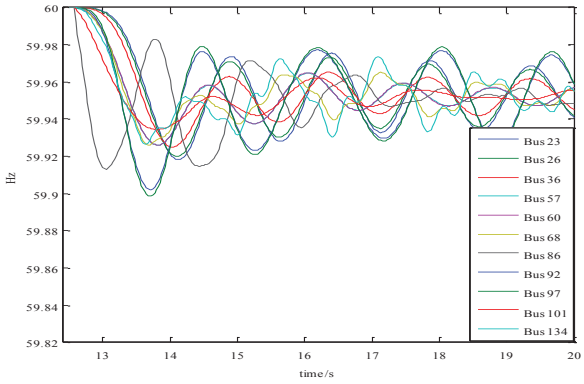

Figure A.2. Bus frequency measurements (the event occurred at 12.58s)

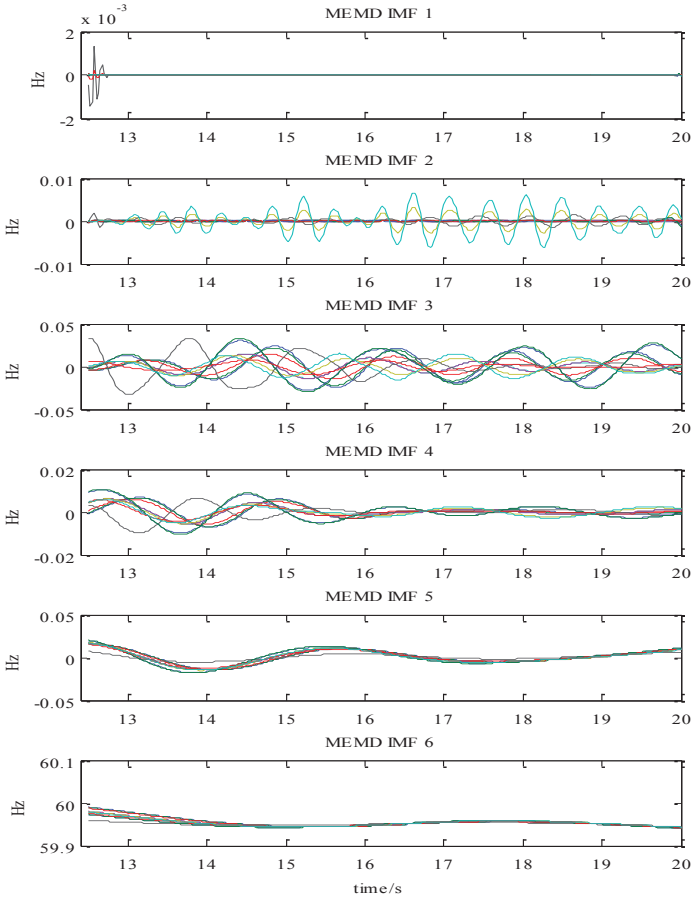

Figure A.3. IMF 1- 6 of the generation trip event in the NPCC system (MEMD)

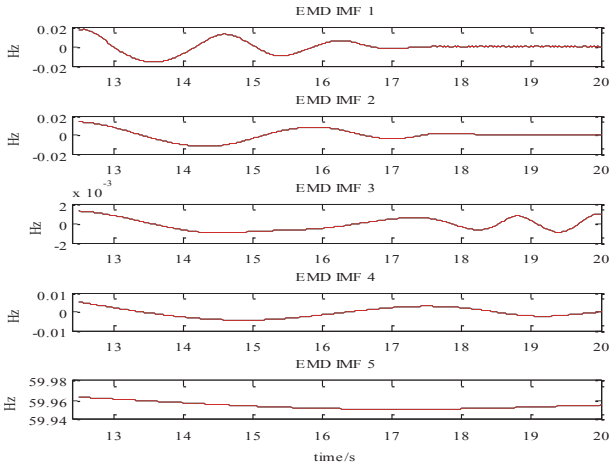

Figure A.4. Bus 60 IMF 1-IMF 3 of the generation trip event in the NPCC system (EMD)

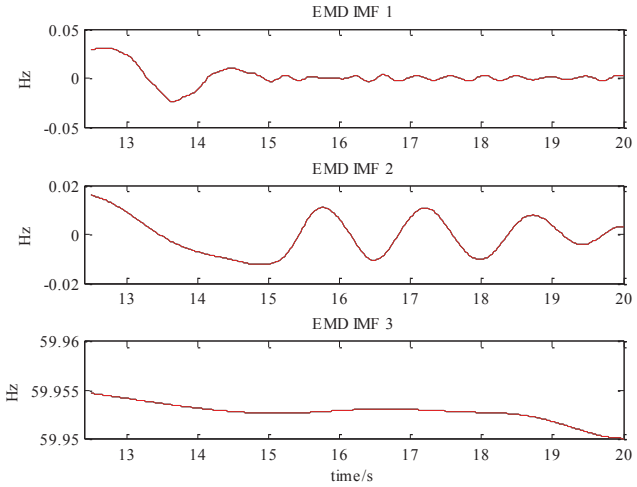

Figure A.5. Bus 68 IMF 1-IMF 3 of the generation trip event in the NPCC system (EMD)

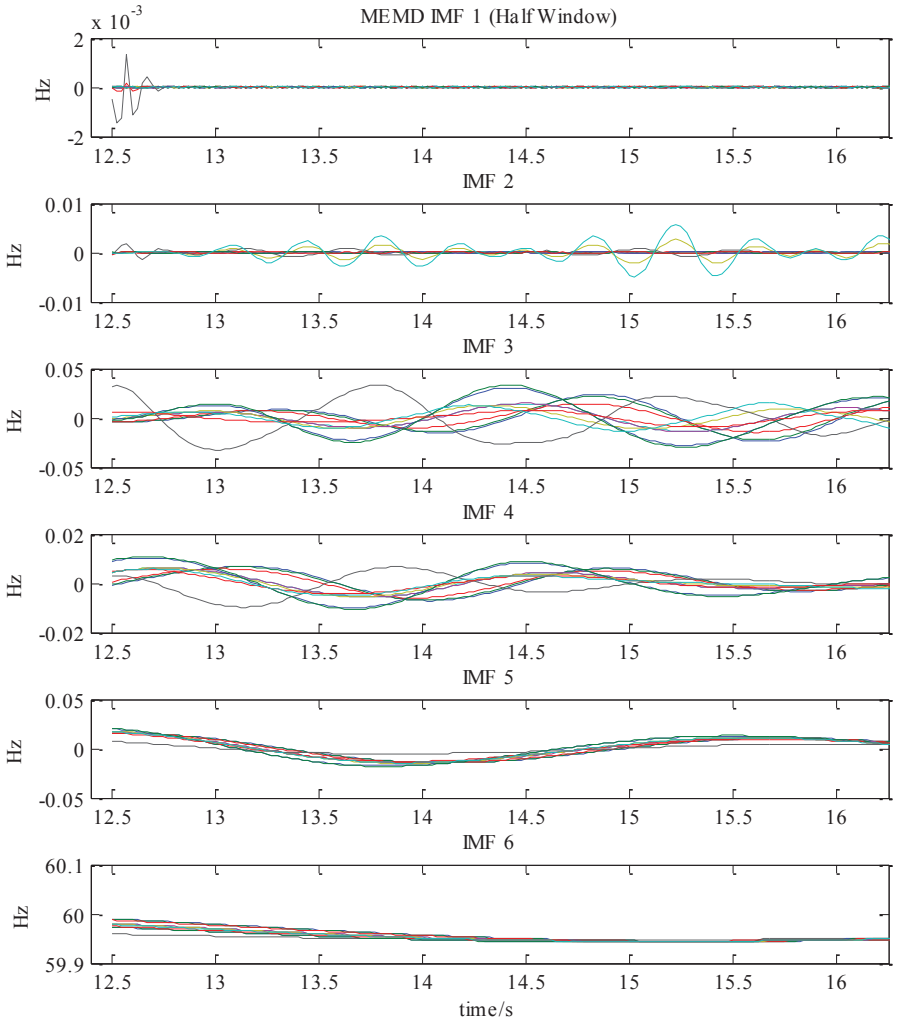

Figure A.6. IMF 1-IMF 6 using the first half time window (MEMD)

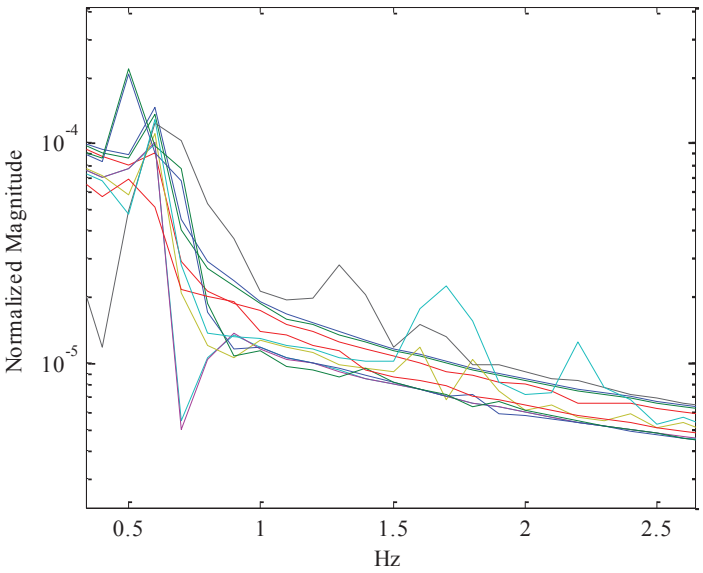

Figure A.7. The FFT spectrum of raw frequency measurements

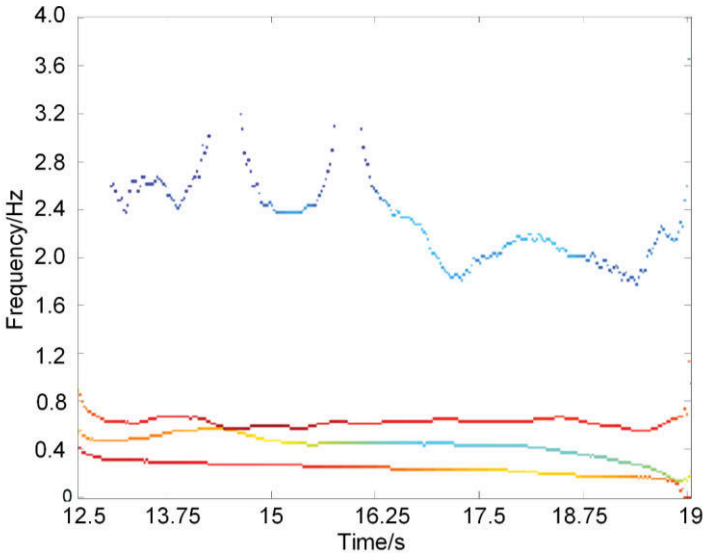

Figure A.8. The Hilbert spectrum of IMF 2-5 (MEMD)

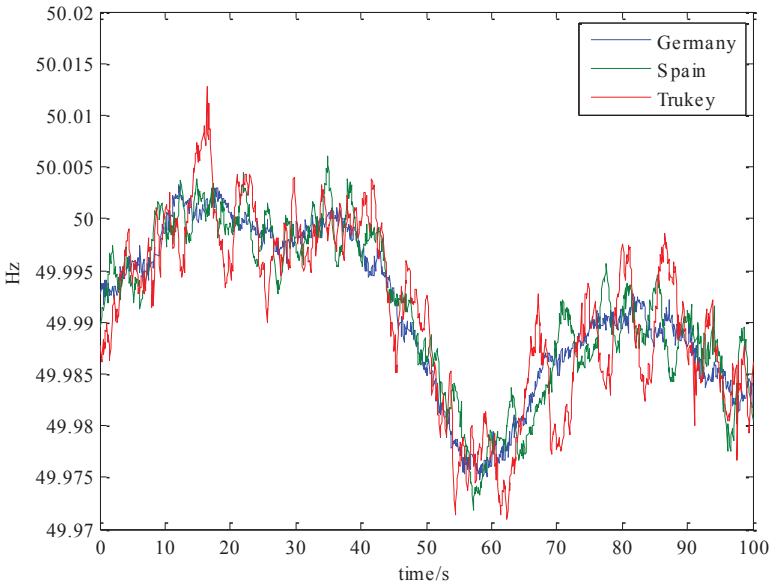

Figure A.9. The European case - ambient frequency measurements with obvious oscillation

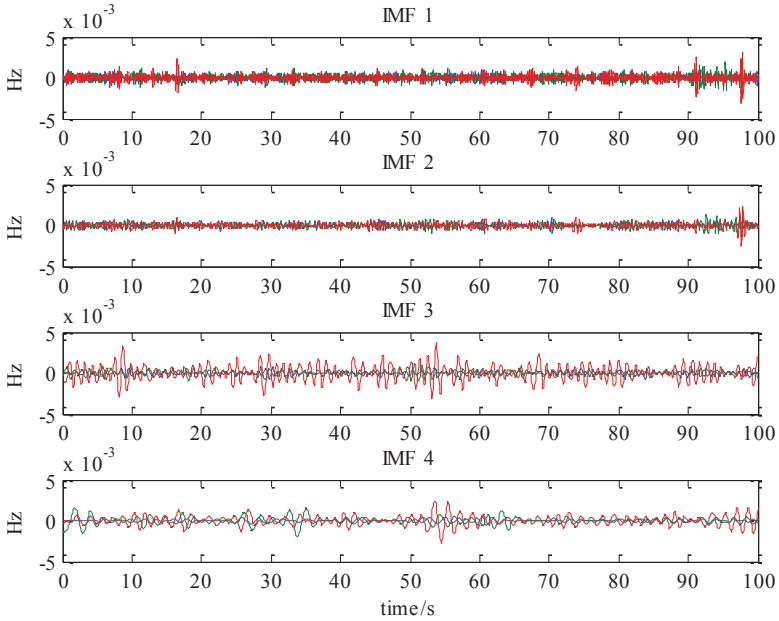

Figure A.10. IMF 1-IMF 3 of the European case

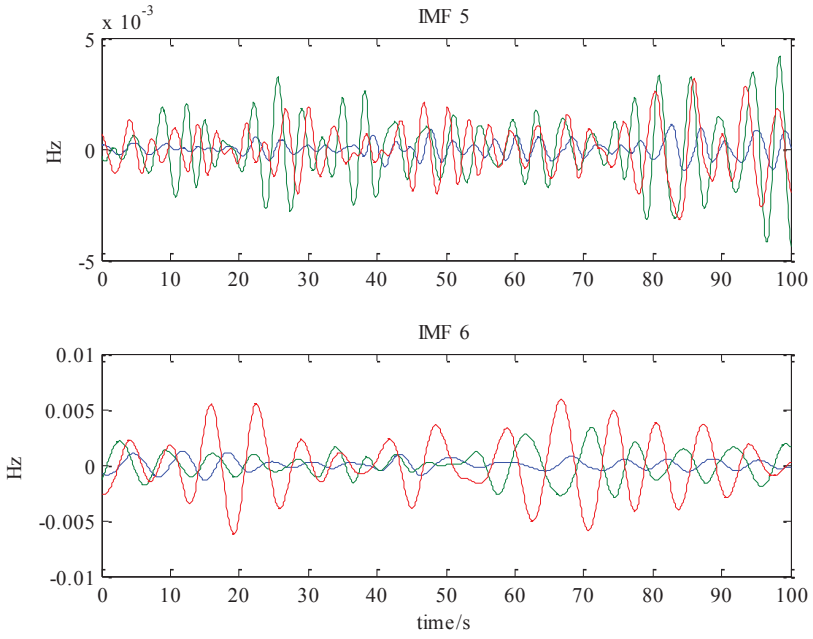

Figure A.11. IMF 4-IMF 6 of the European case

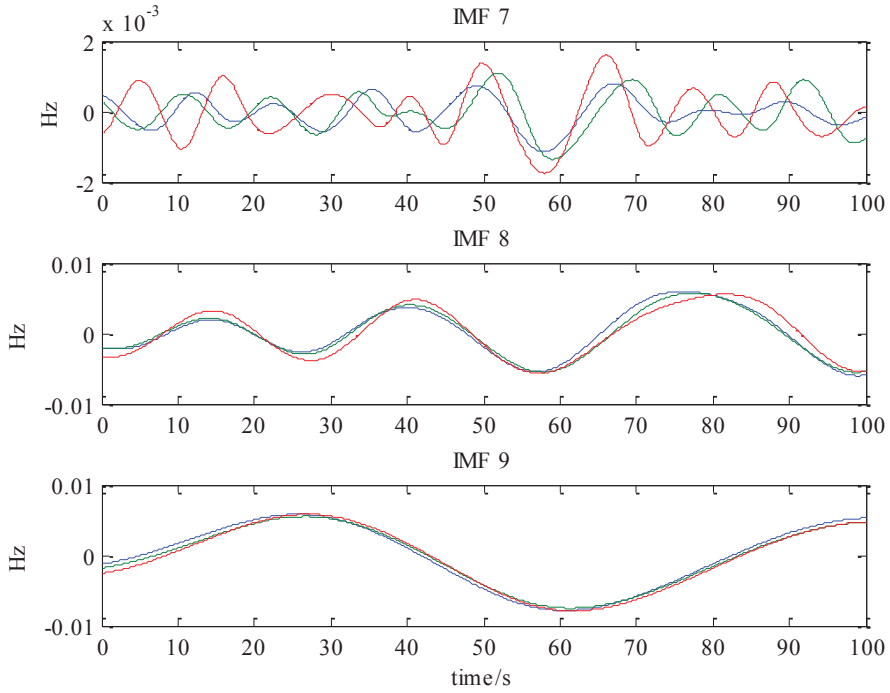

Figure A.12. IMF 7-IMF 9 of the European case

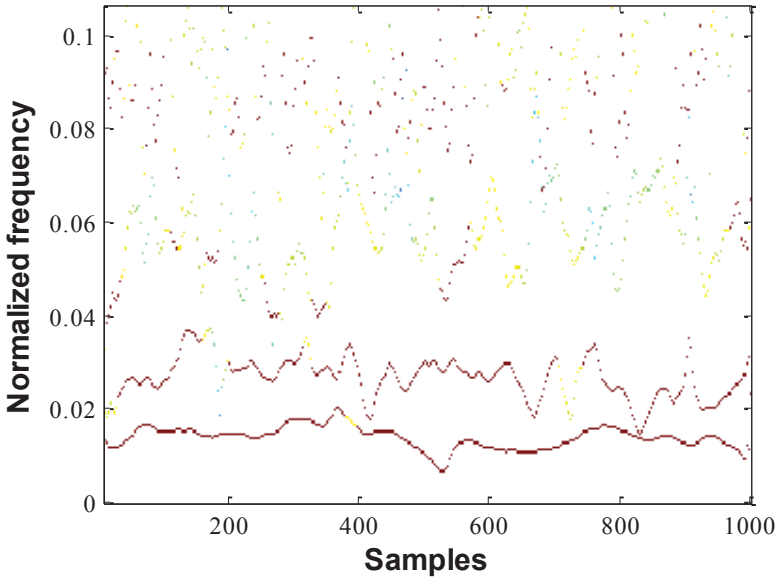

Figure A.13. The Hilbert spectrum (instantons frequency) of IMF 3 to IMF 6 in the European grid ambient measurements

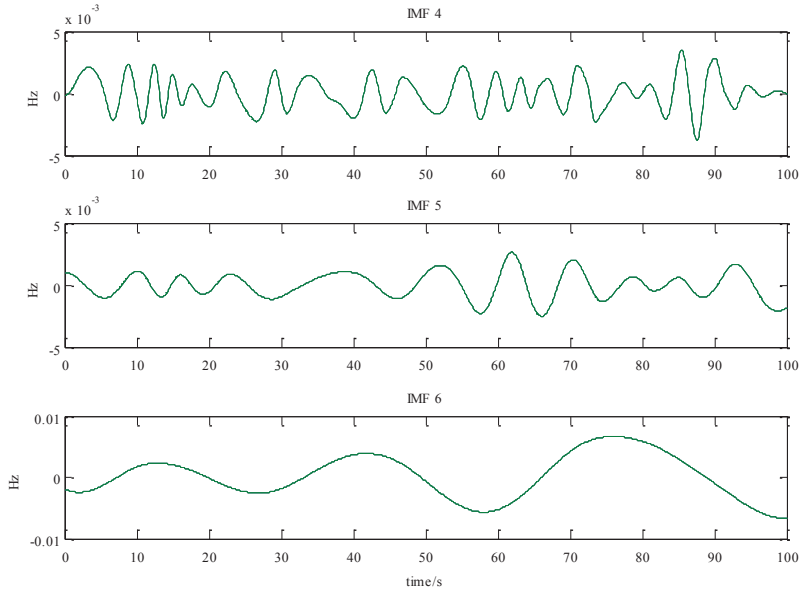

Figure A.14. IMF 4 to IMF 6 obtained by EMD

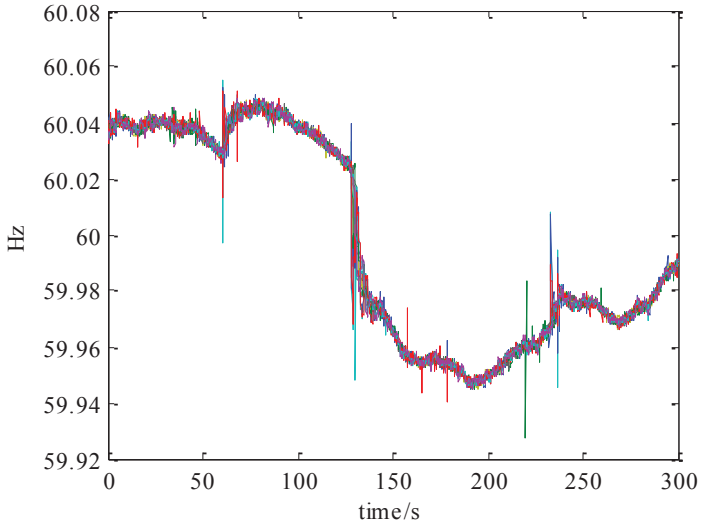

Figure A.15. Frequency measurements of a generation trip event in EI

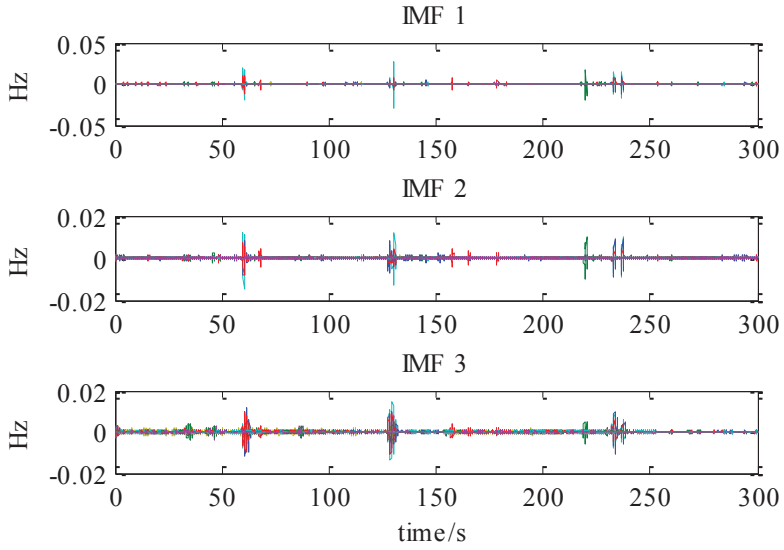

Figure A.16. IMF1-3 of the EI generation trip event

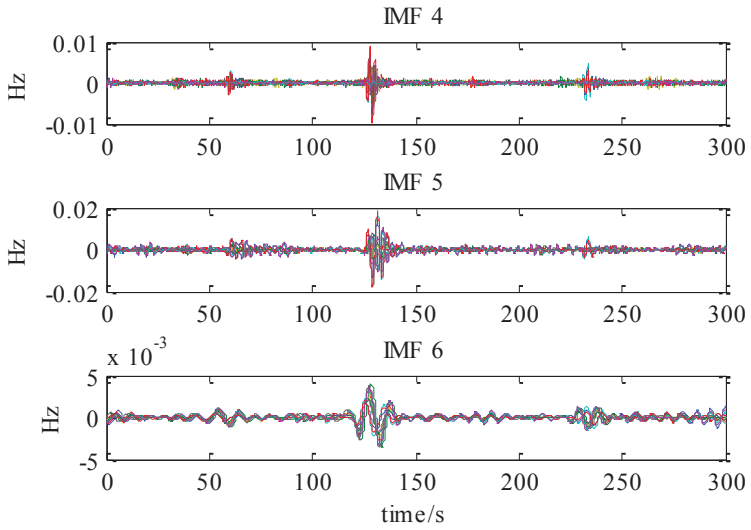

Figure A.17. IMF4-6 of the EI generation trip event

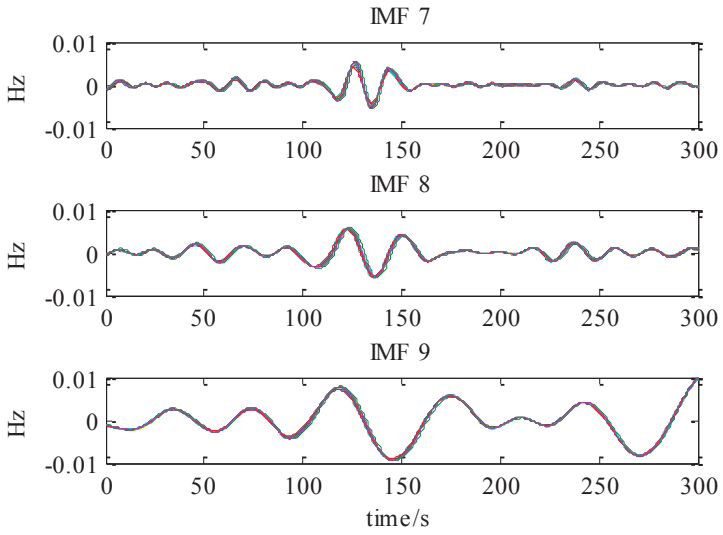

Figure A.18. IMF7-9 of the EI generation trip event

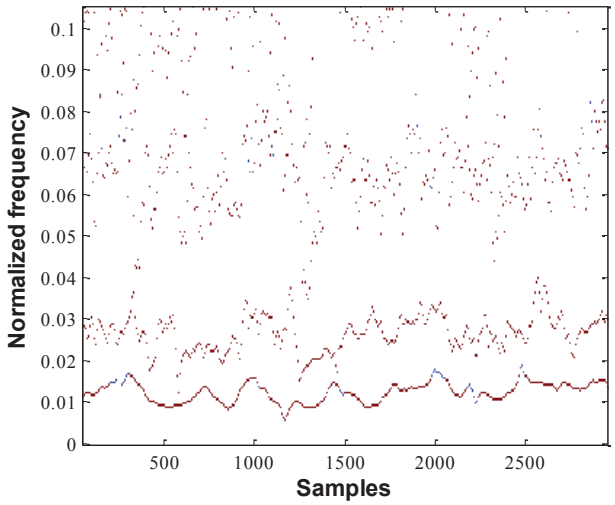

Figure A.19. The Hilbert spectrum (instantons frequency) of IMF 3 to IMF 5 in the EI generation trip event

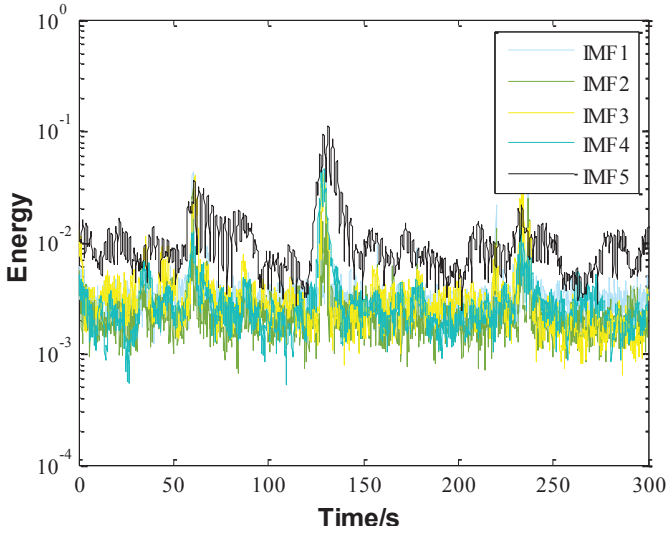

Figure A.20. The energy of IMF1-5 of the EI generation trip event

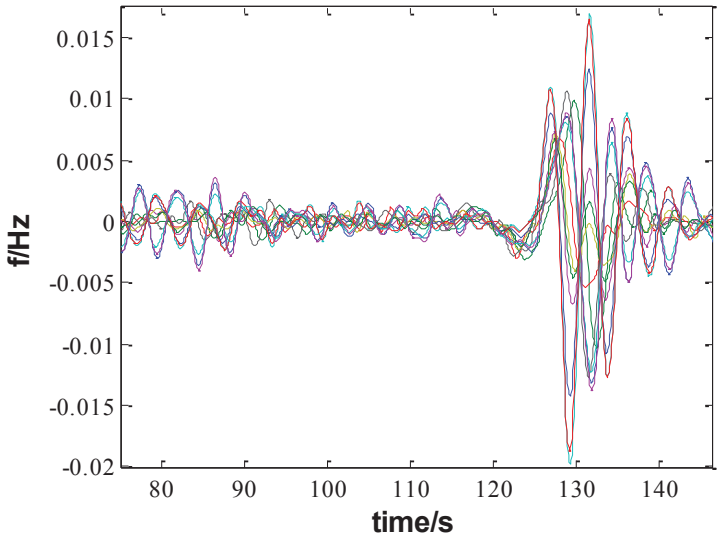

Figure A.21. IMF 5 of the EI generation trip event

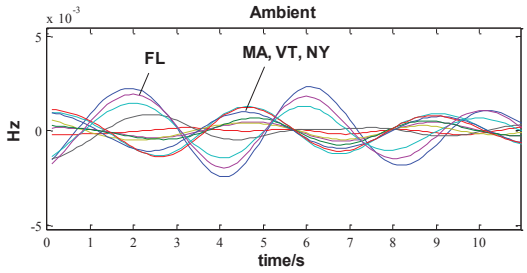

(a) Ambient measurements

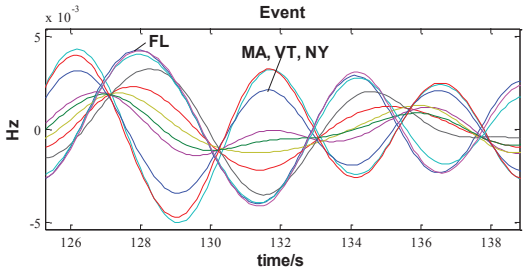

(b) Event measurements

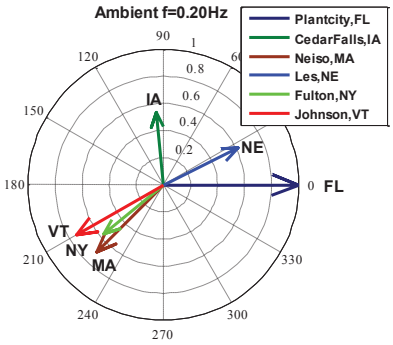

(c) Ambient oscillation mode compass plot

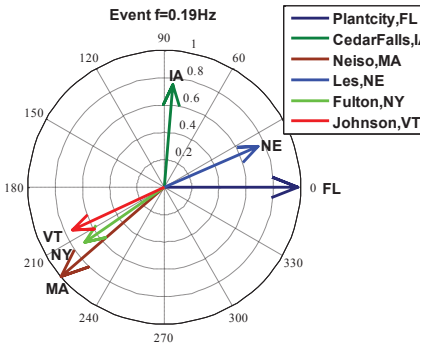

(d) Event oscillation mode compass plot

Figure A.22. Comparison on the identified oscillation mode based on EI ambient and event measurements (IMF 5)

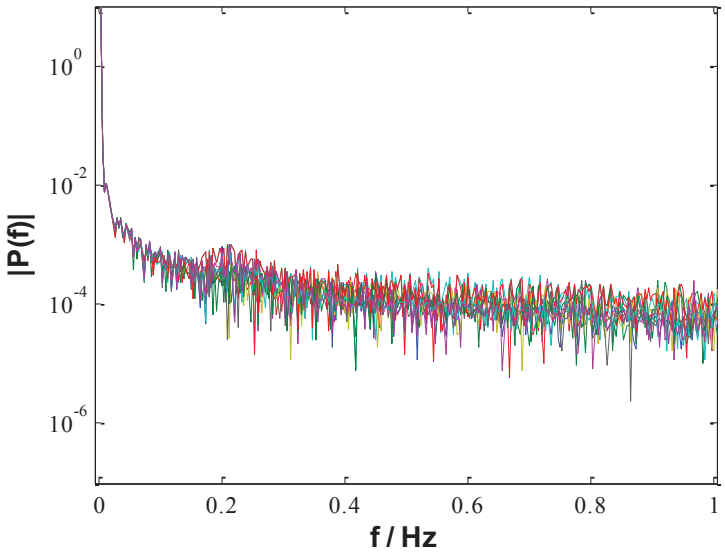

Figure A.23. FFT transform of raw frequency measurements of the EI generation trip event

Appendix B: Chapter One nomenclatures

Nomenclature

$CF_{y,r,s}$	Wind capacity factor of generator g in region *r*, year *y*, scenario *s*
$C_{emm,r,y,g}$	Emission cost for generator g, region *r*, year *y*
$C_{FOM,r,g}$	Fixed operation and maintenance cost of generator g located in region *r*
$C_{fuel,y,r,g}$	Fuel Price for generator g, region *r*, year *y*
$C_{Gbuilt,y,r,g}$	Build cost of generator g located in region *r*, year y
$C_{VOLL,r}$	Value of lost load (energy shortage price) in region *r*
$C_{VOM,r,g}$	Varying operation and maintenance cost of generator g in region *r*
$C_{Wheeling,l}$	The wheeling cost coefficient in interface l
$C_{Xbuilt,y,l}$	Build cost of transmission interface l in year y
DF_y	Discount factor in the year y
$e_{r,g}$	Emission coefficient of generator g located in region *r*
$F_{FOR,r,g}$	Forced outage rate of generator g located in region *r*
L'	Load duration curves of raw chronological load data
$L_{y,r,s}$	Load in region *r*, scenario *s*, year *y*
$L_{y,s}$	System-level load in scenario *s*, year *y*
$MF_{r,s}$	Maintenance factor in region *r* scenario *s*
N_L	Number of transmission interfaces between regions
N_Q	Number of raw chronological curves
N_R	Number of regions

$N_{r,G}$	Number of generators (including both existing and candidates) in region *r*
N_Y	Number of years in the planning horizon
$N_{y,S}$	Number of scenarios in year *y*
$P_{\max,r,g}$	Maximum generation capacity of generator g in region *r*
$\overline{P}_{\max,r,g,s}$	Maximum generation of generator g after considering the forced and maintenance outages discount in scenario *s* in region *r*
$P_{l,\max}$	Maximum transmission capacity of transmission interface l
$pr_{y,s}$	Probability of scenarios *s* in year *y*
pr'_q	Probability of raw load curves *q*
$R_{H,r,g}$	Heat rate of generator *g* in region *r*
$Rs_{y,r}$	Required reserve margin in region *r* year *y*
$RPS_{y,r}$	Renewable portfolio standard percentage in region *r* year *y*
T	Number of hours in each year
$x^0_{r,g}$	Number of existing units of generator g
$\overline{x}_{Gbuilt,y,r,g}$	Max unit number of annual expansion of generator g in region r
$X_{MaxGbuilt,r,g}$	Maximum number of unit expansion of generation g
$X_{MaxXbuilt,l}$	Maximum number of unit expansion of interface l
$\overline{x}_{Xbuilt,y,l}$	Max unit number of annual expansion of interface l
$x^0_{r,l}$	Number of existing lines of interface l
Ω_r	Set of the transmission interfaces of region *r*

Variables

$I_{y,l,s}$	Power flow of transmission interface l in scenario *s*, year *y*
$P_{y,r,g,s}$	Dispatch level of generating unit *g* in scenarios s, region *r*, and year *y*.
$P_{USE,y,r,s}$	Unserved power in region *r*, scenario *s*, year *y*
$x_{Gbuilt,y,r,g}$	Expansion decision variable of generator g
$x_{Xbuilt,y,l}$	Expansion decision variable of transmission interface l in year *y*

Indices

g	Generator index
l	Transmission interface index
q	Raw chronological curve index
r	Region index
s	Scenario index
y	Year index

Appendix C: Active power control diagram of renewable power plants

Many different wind farms controls have been proposed in literature to enable wind generators to have the “virtual”, “artificial” or “synthetic” inertial response to improve power system frequency response. Though it may not be the most effective approach, droop-based inertia control is most likely to be applied in the wind industry because of its simplicity and robustness [310]. In fact, the GE WindINERTIA^{TM} technology, which is a typical droop-based inertia control, has already been implemented in some wind generators. Therefore, to be as practical as possible, this droop-based inertia control approach is applied in this chapter.

Furthermore, if a large percentage of synchronous generators are replaced by renewable generation, the system primary frequency response will also be decreased and the frequency recovery will be slow. As discussed in [161], if working in over-speed zone instead of MPPT point, wind turbines can decrease the rotational speed to release the reserved power in seconds and, as a result, the “governor response” can be provided by wind farms. Furthermore, the wind power reserve can also be achieved through pitch control. Considering the impact of high wind penetration levels on EI and TI frequency response, this type of wind farm governor control is also likely to be procured by the regulation agency to maintain a minimum reserve capacity in the future. Therefore, a droop-based wind farm governor control is also implemented. The diagram of the wind farm active power control is shown in Figure B.1. Deadbands are used to avoid the reaction of the wind farm inertia and governor controls to small random frequency variations during normal operation conditions and filters are used to reject measurement noises or unwanted frequency components.

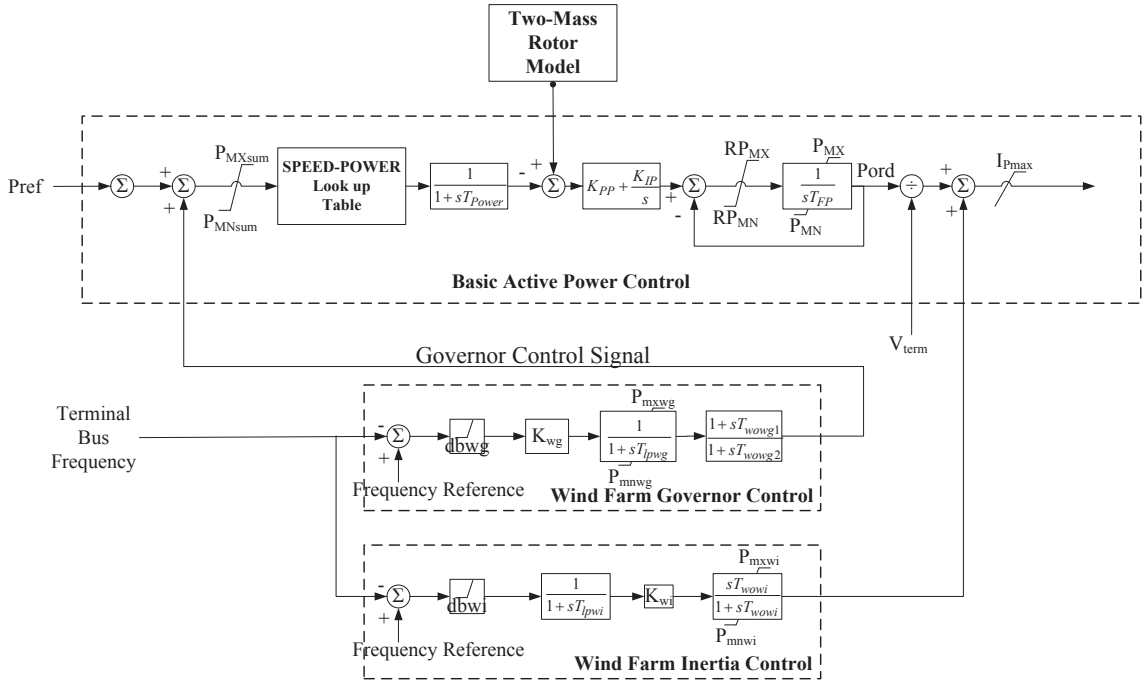

Figure B.1. Diagram of wind farm active power control [173]

Because of the wind farm's capability to control active power, it also has potential to damp electromechanical oscillations [94, 310, 311]. In fact, most of the oscillations in the EI and TI systems are excited by generation failure according to WAMS measurements, so it is beneficial if wind farms can be controlled for frequency control and oscillation damping simultaneously. A wind farm active power control structure similar to conventional power system stabilizer (PSS) is added to the wind farm active power control (as shown in Figure B.2). That link after gain is a high pass filter to eliminate low frequencies that are present in the frequency deviation signal and allows the PSS to respond only to frequency changes. The default value of this wash-out time constant is about 2 second for a generic PSS. Here, 5 seconds is used in the simulation to allow it damp some low frequency inter-area oscillations. Either local or wide-area control signals can be used as the input to this oscillation damping controller.

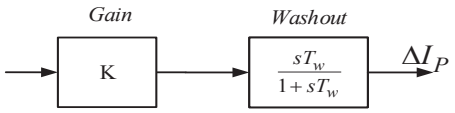

Figure B.2. Wind farm oscillation damping control [173]

Similar to wind power plants, PV power plants can also apply similar active power controls for providing governor response and oscillation damping effects. Different from generic PSS for synchronous generators, Solar PSS doesn't include a phase compensator in because there is no phase lag between the excitation voltage and the electrical torque as in synchronous machine. It includes a high pass filter to eliminate low frequencies that are present in the frequency deviation signal and allows the PSS to respond only to frequency changes. The default value of this wash-out time constant is about 2 seconds for a generic PSS. Here 5 seconds is used in the simulation to allow it damp some low frequency inter-area oscillations. The active power control diagram of PV power plants is shown in Figure B.3. Parameters of the wind farm and PV active power control are listed in Table B.1 and Table B.2.

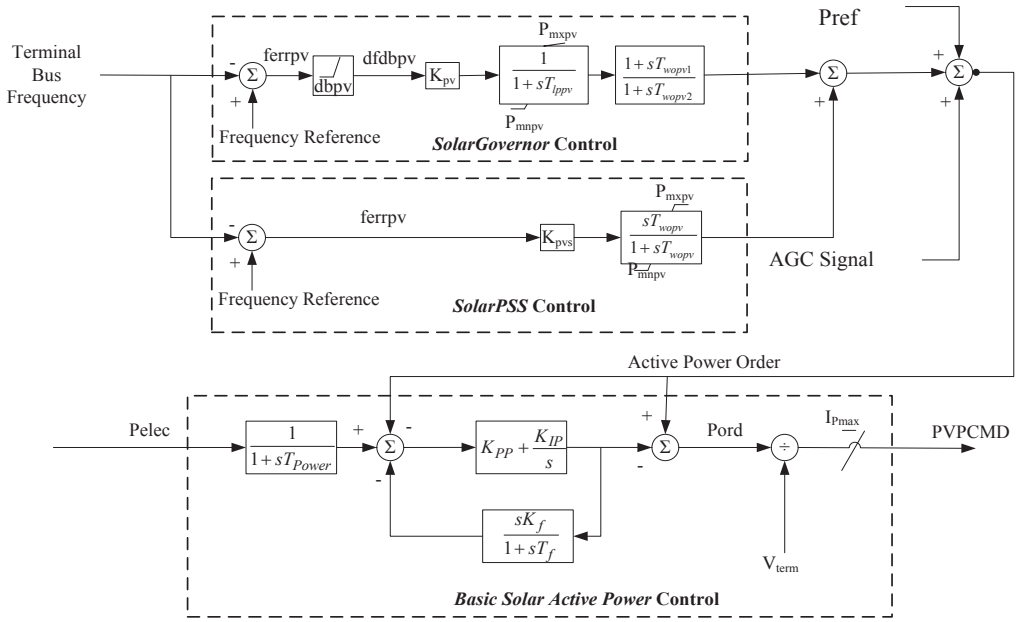

Figure B.3. Diagram of PV power plants active power control [173]

Table B.1. Parameters of the wind farm active power control [173]

Parameter	Value	Parameter	Value
T_{Power}	5.0000	Tlpwi	1.0000
K_{PP}	3.0000	Twowi	5.5000
K_{IP}	0.6000	P_{MXWI}	0.1000
RP_{MX}	0.4500	P_{MNWI}	-0.1000
RP_{MN}	-0.4500	dbwg	0.0001
P_{MX}	1.1200	Tlpwg	0.0500
P_{MN}	0.1000	Twowg1	1.0000
I_{PMAX}	1.1000	Twowg2	1.0000
T_{FP}	0.0500	Pmxwg	0.1000
dbwi	0.0001	K_{wi}	11.7000
K_{wg}	20.0000		

Table B.2. Parameters of the PV active power control [173]

Parameter	Value	Parameter	Value
T_{Power}	0.0500	P_{MNPV}	-0.1000
K_{PP}	0.0500	dbpv	0.0001
K_{IP}	0.1000	Tlppv	0.0500
Kf	0.0100	K_{PV}	20.0000
Tf	0.0800	T_{wopv1}	1.0000
I_{PMAX}	1.1000	T_{wopv2}	1.0000
T_{lppv}	1.0000	P_{mxpv}	0.1000
K_{PVS}	0.0500	P_{mnpv}	-0.1000
Twopv	5.5000	TWOPV	20.00
P_{MXPV}	0.1000		

Appendix D: List of python scripts created in the dissertation study for PSS/e simulation

1. Develop a generic dynamic model based on a power flow model
2. Convert none-deadband governor models into models with headbands
3. Adjust inertia
4. Add wind generation and PV models
5. Statistical analysis on governor response resources
6. Statistical analysis on system inertia
7. Extract specific parameters from a dynamic file
8. Run multiple contingencies in dynamic simulation
9. Convert negative generation to load
10. Add load characteristic models for load modeling
11. Change other dynamic parameters
12. Add/remove/replace dynamic models

VITA

Shutang You was born in China. He obtained his B.S. and M.S. degree in Electrical Engineering from Xi'an Jiaotong University, China, in 2011 and 2014, respectively. He started to work towards his Ph.D. degree at the Power IT Lab, in the EECS department of the University of Tennessee, Knoxville, since August, 2014.